The Role of Adipocytes and Tumour Microenvironment in Ovarian Cancer Progression

Swansea University
Prifysgol Abertawe

Samuel Mark Oliver

Submitted in fulfilment of the requirements
for the Degree of Doctor of Philosophy

Department of Mathematics
Faculty of Science and Engineering
Swansea University

2025

“When I die, I want to die like my grandfather who died peacefully in his sleep. Not screaming like all the passengers in his car.”

Will Rogers

Abstract

As the leading cause of death amongst all gynaecological cancers, ovarian cancer research is an increasingly important area of study. Patients of the disease continue to suffer from significant challenges despite receiving the best treatment currently available. Throughout the past, treatments deemed optimal have been done so based on results from *in vivo* or *in vitro* experiments using physical cells. Advancements in the availability and capability of technology now allows *in silico* experiments to provide alternative methods and insights into tumour growth.

A key aspect of ovarian cancer progression is its tenancy to metastasise. Surrounded by the peritoneal cavity and omentum, the ovaries provide an ideal location for the spread of malignant neoplasms. This, along with the lack of early symptoms exhibited in the majority of cases, causes ovarian cancer to maintain a 5 year survival rate of under 50%. With the help of mathematical models, the scientific community is aiming to increase this statistic by optimising new treatments and preventative approaches.

In this study, we take key aspects of ovarian cancer progression and inhibition and develop multiscale mathematical models to investigate the role of these processes. We begin by exploring the role of adipose tissue found in the omentum. Adipose tissue is home to adipocytes, a cell found to secrete substrates such as leptin and interleukin-6, proven to promote proliferation in cancer tumours. Metastasis occurs as a result of a phenotypic change encouraged by this adipose derived media. The transition between these states, known as epithelial-to-mesenchymal transition is also studied in detail, along with the ability of cisplatin to impede the overall growth of the tumour, with relevant parameters optimised using experimental data.

Acknowledgements

To everyone who has supported and helped me during my PhD, thank you very much as I couldn't have done it without you. Firstly, I would like to thank my supervisor, Professor Gibin Powathil. Beyond just the academic support you have provided me with during my time at Swansea, having you as my mentor for the last four years has helped me in every way imaginable. I'm extremely fortunate to have had you as my supervisor. I would also like to thank Dr Noemi Picco and Professor Deya Gonzalez for their continual willingness to help me throughout the course of my PhD. Thank you also to EPSRC for fully funding the PhD project and making this work possible.

I would like to thank my mum and dad for always being there for me every step of the way. You've both always encouraged whatever is best for me and made me feel incredibly supported. Thank you also to my sisters, Jenny and Katie. The passion you both showed for my masters project studying leafcutter bees in Panama helped inspire my decision to stay in scientific research. Thank you to Chris Vowles, Peter Vowles, and Jayne Pickett for always being so supportive of me. I'm lucky to be a part of such a kind and loving family.

I would also like to thank the friends who helped make my time at Swansea such a pleasure. It's thanks to you that I looked forward to coming into the office each day. In order of my personal preference, thank you to Will Bean, Sadeer Beden, Harry Bryant, Sarah Costa, Xavier Crean, Jonathan Davies, Hassan Eshkiki, Damiano Greco, Indira Jith, Som Kodsueb, Leonardo Lonati, Andrew Pulsipher, Liam Ryall-Friend, Giovanni Solda, Kevin Spinicci (sorry Kevin - I don't know how to do the é symbol on LaTeX), Paul Sutton, Sam Two, Mark White, and the rest of the Computational Foundry. I'd like to give a special thanks to my friend and colleague Dr Kira Pugh for giving me such a kind, optional welcome to Wales, always being happy to take up the slack, and providing so many unforgettable memories from all corners of the world.

Declaration of Authorship

This work has not been previously accepted in substance for any degree and is not being concurrently submitted in candidature for any degree. The work in this thesis has, however, undergone peer review and has been presented at major international venues. The publications noted below were prepared for submission during my candidature. The work in Chapter 2 (P1) has been submitted for publication and is currently in preprint. The work in Chapter 3 (P2) has been published and the work in Chapter 4 is to be submitted in the future for publication.

(P1) **Oliver, S.**, *Williams, M., Howard, D., Gonzalez, D. and Powathil, G., 2025. Investigating the Impact of Omental Adipocytes on Ovarian Cancer: Insights from a 3D in-silico model. bioRxiv, pp.2025-07.,*
DOI: https://doi.org/10.1101/2025.07.03.662794

(P2) **Oliver, S.**, *Williams, M., Jolly, M.K., Gonzalez, D. and Powathil, G., 2025. Exploring the role of EMT in ovarian cancer progression using a multiscale mathematical model. npj Systems Biology and Applications, 11(1), p.36.,*
DOI: https://doi.org/10.1038/s41540-025-00508-y

DECLARATION - This work has not previously been accepted in substance for any degree and is not being concurrently submitted in candidature for any degree.

Signed [redacted](candidate)

Date _________________

Statement 1 - This thesis is the result of my own investigations, except where otherwise stated. Other sources are acknowledged by footnotes giving explicit references. A bibliography is appended.

Signed [redacted] (candidate)

Date _________________

Statement 2 - I hereby give consent for my thesis, if accepted, to be available for photocopying and for inter-library loan, and for the title and summary to be made available to outside organisations.

Signed [redacted] (candidate)

Date _________________

Statement 3 - The University's ethical procedures have been followed and, where appropriate, that ethical approval has been granted.

Signed [redacted] (candidate)

Date 14/10/2025

Contents

List of Figures

List of Tables

List of Abbreviations

2D	**2 D**imensional
3D	**3 D**imensional
ATP	**A**denosine **T**ri**P**hosphate
BAT	**B**rown **A**dipose **T**issue
ECM	**E**xtra**C**ellular **M**atrix
EGF	**E**pidermal **G**rowth **F**actor
EMT	**E**pithelial to **M**esenchymal **T**ransition
G1	**G**ap **1**
G2	**G**ap **2**
IL-6	**I**nter**L**eukin-**6**
IL-8	**I**nter**L**eukin-**8**
LHS	**L**atin **H**ypercube **S**ampling
M	**M**itosis
MET	**M**esenchymal to **E**pithelial **T**ransition
MMP	**M**atrix **M**etallo**P**roteinase
ODE	**O**rdinary **D**ifferential **E**quation
OT-CM	**O**mental **T**issue-**C**onditioned **M**edia
PCC	**P**earsons Product **C**orrelation **C**oefficient
PDE	**P**artial **D**ifferential **E**quation
RMSE	**R**oot **M**ean **S**quared **E**rror
S	**S**ynthesis
SVF	**S**tromal **V**ascular **F**raction
TGF-β	**T**ransforming **G**rowth **F**actor-**B**eta
TNF-α	**T**umour **N**ecrosis **F**actor-**A**lpha
U-ADSC	**U**ndifferetiated-**A**dipose **D**erived **S**tem **C**ell
UCM	**U**n**C**onditioned **M**edia
WAT	**W**hite **A**dipose **T**issue

Chapter 1

Introduction

Ovarian cancer is the largest killer of all gynaecological cancers, with a low ten year survival rate of 30% [101, 241]. The disease is found predominantly in post-menopausal women, with almost half the cases in the UK found in women aged over 65 [218]. This poor prognosis can be justified by a range of various reasons. Early stage ovarian cancer is usually asymptomatic, with symptoms appearing only in the latter, often metastasised stages [134]. The most common of these symptoms include bloating, abdominal pain, lack of energy, and frequent urination. These symptoms are closely associated with less severe conditions such as dehydration, lactose intolerance, and coeliac disease, often preventing early detection of ovarian cancer [141, 8]. The stage of diagnosis has a significant role in the chances of survival for the patient. When diagnosed prior to metastasis, ovarian cancer has a five year survival rate of 93% [223], compared to a five year survival rate of 10-20% for women with widespread metastatic ovarian cancer [116].

With such a significant link between the stage of diagnosis and the prognosis for a patient, along with the low rates of early diagnosis, there is a large room for improvement in the treatment a patient may receive. The current standard treatment for ovarian cancer patients involves a combination of surgery and chemotherapy [119]. Surgery alone is sufficient in rare cases where the tumour is small and yet to spread outside of the ovaries and fallopian tubes [199]. Since this situation is unusual, perioperative chemotherapy (administered at the time of surgery) or adjuvant chemotherapy (administered after the surgery) are more common methods of treatment [211, 157]. Drugs in the taxane family such as paclitaxel and docetaxel or drugs which contain platinum such as cisplatin and carboplatin are the most common drugs used for chemotherapy on ovarian cancer [32]. These drugs use either intraperitoneal or intravenous administration, the frequency of which varies from patient to patient depending on the type or stage of the cancer [152]. Despite these methods being the current gold standard of ovarian cancer treatment, there remains to be high rates of recurrence [64]. Application of these drugs also come with various risks and side effects. Exposure to taxane drugs can lead to haematological toxicity, neurotoxicity, and other complex health conditions [81]. Administration of platinum based drugs such as cisplatin can cause effects including nephrotoxicity, gastrointestinal toxicity, nausea, and vomiting [172, 1]. Despite this, cisplatin remains the preferred choice for around 50% of cancer patients [249].

1.1 Adipose Tissue

Smoking is currently the largest preventable factor of tumourigenesis in humans, however, predictions of population trends suggest this is likely to be overtaken in the near future by obesity [20]. Consumed fats are stored as lipids in adipose tissue, a type of tissue with a primary function of storing energy reserves for future use when food availability is low [86]. Adipose tissue is found in various forms throughout the body around organs, muscles, bones, and under the skin [206]. The omentum is a thin layer of adipose tissue stretching in females from the liver down to the ovaries. Due to its location, cells in the omentum can indirectly interact with cells in the ovaries and help them to obtain various "hallmarks" of cancer required to create a malignant tumour [54]. Cancer will often spread to the omentum soon after its development in the epithelial cells of the ovary [130], making it a harder disease to treat and lowering the prognosis for patients. Studies show that 80% of serous ovarian carcinoma cases have spread to the omentum at the time of diagnosis [242], leading to the poor five year survival rate.

The majority of adipose tissue is composed of cells called adipocytes which store any excess energy in the form of lipids [52]. There are three types of adipose tissue, each consisting of the corresponding adipocyte cells: white adipose tissue (WAT), brown adipose tissue (BAT), and beige adipose tissue [90]. Each type of tissue has a different function, appearance, and location in the body, with the prevalence of each depending on factors such as the individual's diet, age, health, and environment [75].

White adipose tissue stores energy as triglycerides and is the most abundant type of adipose tissue found in adult humans [90]. These white adipocyte cells have one large fat reservoir and very few mitochondria, since their role is primarily storage of energy [212]. The two main types of white adipose tissue are visceral and subcutaneous. Visceral WAT surrounds internal organs such as the epicardial adipose tissue around the heart and the peritoneum around abdominal organs

[189]. It helps to provide extra padding and support for these organs to prevent damage or displacement [238]. Subcutaneous WAT is found underneath the skin and provides additional heat insulation for the body [65]. While white adipose tissue does not actively perform thermogenesis, it plays a key role in thermostasis by retaining and preventing heat from escaping out of the body through the surface of the skin [88].

Brown adipocytes store energy in many small lipid droplets dispersed throughout the cell rather than one large pool [245]. The main function of brown adipose tissue is for the production of heat to help maintain thermostasis [197]. Brown adipocyte cells appear this colour due to the high number of mitochondria present [28]. Using advanced lipolysis and oxidisation of fatty acids, the mitochondria can generate large amounts of heat by acting as a catalyst for exothermic reactions within the cell [155]. BAT is found mostly in fetuses and infants in areas around the neck, back, and abdomen [68]. Naturally, babies and young children would be at higher risk to harm when exposed to extremely low environmental temperatures, hence the additional amount of BAT available in the body [23]. The levels of BAT decrease with age until it has all been lost, usually around the age of 80 [188].

The third type of adipose tissue is beige/brite. Beige adipocytes possess similar properties to those which are brown, with their main function also being thermogenesis [135]. However, beige adipose tissue is derived from WAT and each beige adipocyte is only present temporarily [12]. When an organism becomes cold, white adipocytes that have no role in heat production can differentiate into beige adipocytes through a process called "browning" [136]. This produces large amounts of cells with an increased ability to insulate and produce heat, helping to regulate thermostasis [186]. When this extra heat is no longer required, these beige adipocytes can freely return to white adipocytes by losing the additional mitochondria they temporarily had to produce the excess warmth [5]. Cancer cachexia often induces this browning process, since the lack of insulation can promote the biogenesis of beige adipocytes [95].

Alongside adipocytes, components of the stromal vascular fraction (SVF) are also present in adipose tissue [233]. The SVF is a highly heterogeneous assembly of cells including stem cells, macrophages, and fibroblasts [118, 16]. Adipose derived stem cells have a key role in wound healing due to their ability to self renew and differentiate into various cell types [87]. Macrophages are thought to be a major source of chemical messengers such as tumour necrosis factor alpha (TNF-α), interleukin 6 (IL-6), and interleukin 8 (IL-8) contributing to the phenotypic characteristics of cancer cells in the vicinity [246]. Fibroblasts help to construct the connective tissue found around organs to protect them from external damage, as well as serving as progenitors for adipocytes [173]. Due to the production of these components, adipose tissue as a whole is a highly complex structure with functionality beyond simply the storage of fat, playing a key role in the progression and treatment outcomes of cancer tumours.

1.2 Mathematical Modelling

Mathematical models and simulations are rapidly gaining an increasingly significant role in drug development. Computer simulations can complement the results found *in vitro* and *in vivo*, as well as make predictions to find results outside of the obtained biologically experimental data. Depending on the complexity of the model, *in silico* experiments are generally faster than *in vitro* and *in vivo* experiments, with *in vivo* experiments often requiring rigorous ethical approval and large periods of time for highly qualified experimentalists. Computer simulations require no physical cells or resources to develop and run.

Various approaches can be taken when developing a mathematical model. Ordinary differential equation (ODE) and partial differential equation (PDE) models provide an analytical approach to finding cell populations across time. These models are mostly deterministic, with identical results observed when no parameters or equations have been changed. While theoretically possible, finding analytical solutions such as steady states, bifurcation diagrams, and stable/unstable manifolds are realistically difficult. ODE models can also miss key stochastic events and struggle to capture the spatial aspect of where populations are distributed within a domain, with no information captured on individual cells in an ODE model. This can lead to the omission of key individual dynamics, such as the competition between cells for resources based on their proximity to other cells in the domain. For heterogeneous substrates within a domain, the concentration of oxygen, glucose, and other essential substances for cells can vary depending on the location and proximity to the blood vessels. Since ODE models cannot provide this individualised information, agent-based models are often a popular alternative when spatio-temporal dynamics need to be observed.

The development of agent-based models involve creating rules to which the agents (in this case, cells) abide. The rules can depend on the conditions in the microenvironment in which each cell is placed, inducing phenotypic changes to single cells rather than entire populations. This provides a model with a more heterogeneous layout, which is crucial when dealing with 2 dimensional (2D) or 3 dimensional

(3D) tumours, throughout which resources vary dramatically. Characteristics regarding each individual can then be extracted from the results and a more detailed analysis can be performed, compared to if only the total populations were available to the user. Agent-based modelling treats every agent (for example, in this case a cell) separately and will likely produce slightly different results on each simulation due to the random nature of each component involved. These models are generally more likely to reach extreme scenarios and exact states such as a tumour free equilibrium, since the stochastic nature can allow entire populations to eradicate.

Many different agent-based tumour modelling frameworks are available, each with their own unique approach. The user must therefore decide on what aspects of the model they wish to prioritise based on what results are important to them. Chaste [147] is an open-source simulation package used to model the dynamics of soft tissue. Developed in the University of Oxford, the Chaste package focuses on the modelling of cardiac electrophysiology and the development of cancer. The off lattice simulations incorporate ODE and PDE solvers to help produce spatially heterogeneous domains. Alongside Chaste, Morpheus [209] is an alternative modelling environment used to study multicellular systems. Multiscale simulations can be developed using a graphical user interface in either a 2D or 3D domain, taking a cellular Potts approach. Cellular Potts models are also used in CompuCell3D [214], a simulation framework used for single and multicellular modelling. These simulations produce an on lattice virtual tissue to examine a wide range of biological processes and their dynamics. In collaboration with CompuCell3D, Tissue Forge [194] is a recent alternative modelling framework that allows users to explore models at biologically relevant length scales. Tissue Forge is off lattice with a built in combination of a wide range of modelling methodologies. Here, cell movement is force based, supporting Newtonian and Langevin dynamics.

The models developed in this study will use a PhysiCell version 1.13.1 framework [73, 72]. PhysiCell is a multiscale agent-based modelling framework used for 2D or 3D simulations. Cells move off lattice with physics-based velocities dependent on adhesion and repulsion forces between neighbouring cells. Phenotypic characteristics such as cycling rate, death rate, and substrate secretions can be manually adapted, with substrate concentrations tracked on a separate mesh. Substrate diffusion, decay, and adaptable boundary conditions can be implemented and controlled. Simulations automatically generate tumour cross-sections, individual cell information, and substrate spatial data in the output with low computations cost.

1.2.1 Previous Adipose Tissue and Cancer Models

This section aims to cover examples of previously designed models to compare the different ways that adipose tissue has been considered to quantitatively affect the growth of cancer. These models vary greatly in style and complexity, using many different approaches to represent the dynamics. Continuous, ODE based modelling appears to be the preferred method of choice for mathematical biologists looking into the field of tumour growth and fat tissue. These models generally involve less stochasticity than standard agent-based models since they can be studied analytically using ODE solvers such as MATLAB's ODE45 function [2].

RA Ku-Carrillo et al [26] developed an ODE model which initially included three cell type densities: immune cells, cancer cells, and normal cells, with an adipocyte cell density added following further development of the model. Constant source and death rates of immune cells were assumed due to the body's attempt to combat the disease. Tumour, normal, and fat cells were all assumed to show logistic terms with individual intrinsic growth rates, alongside the impacts of heterogeneity in the microenvironment and interspecific competition and mutualism. An analysis of the model was performed, investigating the impact of fat cells on the equilibrium points and bifurcation diagrams [49]. The analysis found three biologically realistic equilibrium points:

1. **The immune, cancer, and fat cell equilibrium.** This is the point where no normal cells remain, with death occurring in patients before the cancer can realistically get to this stage.
2. **The cancer free equilibrium.** Here, only normal, immune, and fat cells remain and the patient is considered to be cancer free. This point is stable if the parameter values used in the model satisfy a strict inequality.
3. **The coexistence equilibrium.** All four types of cells are present at this steady state. This could be the situation where a tumour is dormant and not changing in size, potentially allowing for future metastasis.

Further analysis concluded that lower values of the fat cell carrying capacity lead to significantly lower levels of fat and cancer cells at the coexistence equilibrium, in turn resulting in higher levels of normal and immune cells. An additional development of the model then focused more heavily on the interactions between fat and cancer cells. An additional term was included to account for processes such as cachexia, where advanced cases of cancer have been found to reduce fat and muscle volume in patients, causing significant weight loss [46]. These findings provide us with an insight into the extent to which the fat cells can contribute to tumour growth using previously developed mathematical models.

RA Ku-Carrillo et al [27] later incorporated the usage and effects of a chemotherapeutic drug into the model, in which it was assumed that the drug caused exponential decay of the population for each cell type. When optimising the treatment, the negative side effects are accounted for by including a cost function to minimise the effect on normal cells and maximise the effect on tumour cells. A set of "kill effectiveness" parameters was introduced to represent the impact the drug has on the population of each respective cell type. In the simulations, the chemotherapeutic treatment was only administered into the model when the number of normal cells was over 75% of the initial population. Further analysis was performed to find the optimal method for drug administration, with the *in silico* results finding that drugs should be administered either at their maximum rate or not at all using a binary "on/off" approach.

A different model was designed by T. A. Yildiz et al [244] using fractional calculus without a singular kernel. The ODEs incorporate logistic growth terms and intercellular relationships using Caputo-Fabrizio fractional derivatives, with a linear expression for the influence of the drug on each cell. The model investigated the optimal control problem (Equation 1.1) and aimed to minimise both the number of tumour cells and the use of chemotherapeutic drugs, while maximising the number of normal cells.

$$\min_{(u_1, u_2 \in U_{ad})} J(u_1, u_2) = \int_0^{t_f} (\omega_1 T - \omega_2 N + \omega_3 u_1^2 + \omega_4 u_2^2)\, dt \tag{1.1}$$

Here, u_1 and u_2 are example treatment plans for drugs 1 and 2 respectively, taken from the set of all possible treatment protocols U_{ad}, t_f is the final time of drug treatment, and T and N are tumour and normal cell populations respectively. The ω_i terms are included to account for the side effects of each drug. The results suggested that the cancer-free equilibrium state can be achieved when the drugs are used at varying rates, rather than the binary on/off approach found previously. These varying rates depended on the parameter values, suggesting the importance of optimisation in mathematical models.

Despite the limited number of previous mathematical models linking cancer tumour growth to adipose tissue, there are significantly more models investigating the role of stromal cells in general on the progression of malignant tumours. The stroma is the connective tissue within organs that provides support and aids effectiveness [216]. While stromal cells often have no direct use in the primary purpose of the organ, they can be crucial in maintaining the overall functionality and structure [170]. Stromal cells play a key role in the development of different components of the blood and the body's immune system. Types of stromal cells include pericytes, fibroblasts, adipocytes, and endothelial cells [22]. Malignant tumours can exploit these cells to help promote tumour progression, such as encouraging angiogenesis and metastasis [181]. The metastatic stage of a tumour is a key factor in determining a patient's prognosis, with metastasis thought to account for 90% of all deaths caused by cancer [30]. Over half of the metastasised cases spread first to the bone [166]. When stromal cells become cancer-associated, they can increase cancer cell proliferation by secreting factors promoting tumour growth and development [22]. For this reason, targeting therapy at the cancer stroma as well as the tumour itself has been considered to be a significantly beneficial area of treatment [47].

In 2010, NK Martin et al [145] designed a model linking the normal cell density, tumour cell density, and H^+ ion concentration. The extracellular matrix (ECM) and active matrix metalloproteinase (MMP) densities were also included. MMP is a protease that can break down the ECM, allowing the cancer cells to spread through the body more easily and metastasise [234]. Unlike many others, this model accounted for the spatial ecology of the components and allowed the tumour cells, H^+ ions, and MMP to diffuse throughout the domain according to the concentration gradients. With these densities having such a large impact on the tumour size over time, adding this spatial dimension to the model gave a further and more realistic insight into how these cells interact with each other over time and their dependence on the parameter values. The H^+ ions produced by the cancer cells lead to an acidic microenvironment, increasing the death rate of normal cells. The death of normal cells allows space to free up for cancer cell proliferation, in turn increasing H^+ production and normal cell death. Numerical analysis of the model produces travelling wave solutions. Tumour cells, H^+ ions, and active MMP take over areas previously occupied by normal cells and the ECM due to the acidic conditions and MMP degradation. This phenomenon would be lost without the spatial aspect of the model, providing a new look at how tumour and normal cells interact with each other and the components of the stroma.

Kim et al [120] developed a model to explore how the density of tumour, fibroblast, and myofibroblast cells, as well as the concentration of epidermal growth factor (EGF) and transforming growth factor beta 1 (TGF-β1) are linked. Substrate concentrations are calculated using (PDEs) to incorporate chemotaxis, leading to a model more complex than those previously investigated. Chemotaxis is when cells migrate in response to chemical gradients in the microenvironment. The inclusion of this process can make mathematical analysis difficult [184] due to the non-linear nature of the system. The sensitivity of certain parameter values on the system, such as chemotactic sensitivities, phenotypic transformation rates, and substrate production rates, was evaluated. The study found that only the production rate of EGF from myofibroblasts and the transformation rate of fibroblasts into myofibroblasts had statistical significance on the number of tumour epithelial cells, both of which showed a strong positive correlation. These results from the model were then compared to the previously collected experimental data, with a close agreement to the *in vitro* results. The experiments concluded that the differentiation of fibroblast types can have a key impact on the growth of cancer tumours. Initialising tumours with an absence of any fibroblasts, normal fibroblasts, or tumourigenic fibroblasts each appeared to have a statistically significant impact on tumour size. Having larger adipose tissue has been found biologically to increase the density of fibroblasts via adipose derived stem cell differentiation, accentuated when the tissue is dysfunctional in some way [19]. This again suggests the significance of including adipose tissue in mathematical models to ensure these impacts can be accounted for.

1.2.2 Conclusions of Models

The models discussed in Section 1.2.1 highlight the importance of adipose tissue and the stroma in the outcome of treatment effectiveness. Despite using contrasting approaches and styles of mathematics in their models, obesity was consistently found to have an important effect on the growth of cancerous tumours. The prognosis of the treatment depends heavily on the amount of adipose tissue present around the neoplasm, as well as the location and stage of the cancer at the time of diagnosis.

Each previous model discounts certain aspects of the tumour heterogeneity. Tumours are made up of a mix of different cancer cell types, such as drug-resistant or susceptible cells. The microenvironment has a key impact on the tumour size, with oxygen and glucose levels contributing to the cycling rate of the cells in a neoplasm. The concentrations of these substrates vary greatly throughout a 3D spheroid, in which interior cells may be starved of nutrients, leading to a necrotic core, for example, often omitted by ODE models. With no built up drug resistance or heterogeneity incorporated, the treatments would remain equally as effective regardless of how many times a drug has previously been administered. Drugs are initially efficient in killing the susceptible cells but the remaining drug-resistant cells will remain and proliferate, passing their resistant nature onto the next generation through clonal replication [13]. After each treatment has been administered and fewer susceptible cells remain, more space will become available for resistant cell division. Therefore, future treatments would be less successful in removing the tumour due to the high composition of resistant cells that take up this new space. Future investigations should therefore aim to include the substrate heterogeneity and the effects these adipose tissue secretions have on the tumour size.

In continuous models such as those mentioned previously, the tumour size can reduce but will generally always remain non-zero, potentially allowing the cancer cell population to recover and redevelop into a tumour. Using discrete, agent-based models would allow for other equilibriums to be reached. Upon eradication of the cancer cells (for example, due to treatment, immune response, or natural cell death), the simulation can reach the cancer free equilibrium, allowing mathematical models to help determine if this state can realistically be achieved in a patient.

Many different aspects need consideration when deciding how future models in the field should be constructed. Previous designs can be built upon to include the latest understandings of biological processes and breakthroughs found in medicine. With the link between adipose tissue and cancerous tumours being so profound, further research and discoveries made in the area can help to reduce ovarian cancer-related deaths and increase recovery rates. This is especially important in the modern day, with unhealthy diets becoming more popular, causing an increase in rates of obesity throughout the Western world.

1.3 Thesis Outline

This study aims to develop a selection of multiscale, agent-based mathematical models to investigate the link between adipose tissue volume and ovarian cancer progression. The study will focus on two of the most common ovarian cancer cell lines observed in patients: OVCAR-3 (a human ovarian epithelial carcinoma) and SKOV-3 (an adenocarcinoma) [176], each exhibiting highly contrasting characteristics. Both cause severe, heterogeneous malignancies and have low treatment success rates [115, 169]. Biological observations are obtained from *in vitro* experiments to determine the role that adipose tissue can have on the two cell lines and the tumour compositions. Epithelial-to-mesenchymal transition (EMT) is incorporated into the model to ensure that the correct tumour heterogeneity can be captured. Cells undergoing EMT alter their phenotype by varying their cycling rate, motility speed, adhesive strength, and shape. The model aims to capture these processes and the variations the two cell lines show in their EMT dynamics. The bystander effect will be incorporated into the model, where cells which have already undergone EMT encourage surrounding cells to follow, inducing pockets of mesenchymal cells within the tumour. The inclusion of this effect will be crucial in capturing the observed appearance of the tumours in the presence of adipose tissue.

Chapter 2 will focus on the impacts that adipose tissue has on the progression of ovarian cancer. Comparisons will be made between simulated tumours, with the expression of N-Cadherin and E-Cadherin tracked in each experiment. The role of initial tumour size, amount of adipose tissue in the microenvironment, and dosage of a drug treatment are spatio-temporally investigated by examining tumour population sizes and cross-sections of the simulated spheroids. The difference in population dynamic trends between tumours in high and low adipose tissue environments will be investigated.

In Chapter 3, we will develop the model further and study in more detail the process of EMT and the main drivers of this transition. At this point, mesenchymal-to-epithelial transition (MET), the reverse process of EMT, will also be included to capture the transition in more detail. We will perform a sensitivity analysis to study the key parameters in the model responsible for the changes in the output variables such as total population or final tumour composition. A third cell type, hybrid cells, will be introduced to help aid the comparisons made with additional *in vitro* data.

Finally in Chapter 4, the drug effects are included in the model with more detail. Data collected on OVCAR-3 and SKOV-3 spheroids for both wild type and cisplatin resistant cell types will be used to optimise the drug-related parameters incorporated into the model. A modification of Latin hypercube analysis will be used to optimise these parameter values by minimising the root mean squared error ($RMSE$) between the simulation output and *in vitro* data. Following this optimisation, the results will be fitted to Emax/linear functions to allow for predictions to be made. These predictions will include *in silico* recreations of *in vivo* settings with varied initial tumour compositions, modelling tumours with surrounding blood vessels to allow a more realistic system of drug administration and predictions to be made beyond the scope of biological experiments.

The overall objective is to provide mathematical models of varying complexity to make predictions regarding patient outcomes. The predictions involve the impact of adipose tissue and cancer cell interactions while incorporating the complex heterogeneity of a malignant tumour. The detailed microenvironment can lead to the investigation of patient specific scenarios, allowing a more personally tailored treatment program to be provided based on an accurate and biologically motivated model.

Chapter 2

An Initial Approach to Adipocyte Driven Tumour Dynamics

2.1 Introduction

As well as acting as a home for secondary ovarian tumour masses, adipose tissue was previously thought to be a relatively passive tissue with a role of simply storing fats and regulating heat production. However, more recently it has been discovered to also act as an endocrine function and plays a key role in hormone regulation [69, 174]. Peptides such as leptin and adiponectin were found to be secreted by adipose tissue, both important cytokines in tumour growth and progression [33]. They play a key role in inflammation, angiogenesis, cell proliferation, and other processes, many of which are unrelated to cancer [55]. Leptin induces IL-6 and IL-8 production, examples of proinflammatory chemokines proven to promote cancer progression and metastasis as well as inducing angiogenesis [198, 137, 229]. Adiponectin has been shown to have opposite effects to leptin, promoting cell cycle arrest and apoptosis [114]. Leptin regulates the energy balance in the body by influencing satiety levels while concurrently encouraging the development and progression of cancer [175]. Simultaneously, the down regulation in the expression of adiponectin observed in obese patients also leads to generally more aggressive and uncontrollable tumours [99]. Patients with lower levels of adiponectin generally have more severe and aggressive cases of cancer and higher rates of malignant cell growth. Obesity can cause an imbalance in these hormones by increasing levels of leptin and decreasing adiponectin [67], leaving the patient at a higher risk of developing severe cancer. Enlarged adipocytes can lead to a lack of oxygen to healthy cells causing necrosis, attracting proinflammatory macrophages to further cause inflammation and progression of cancer [205]. As a result of these interactions between the adipocyte cells in the stroma and the epithelial cells, as well as the rise in obesity levels in the modern world, more attention is being put on this link between fat levels and cancer [6]. In the last decade, it has become increasingly apparent that the development, progression, metastasis, and chemoresistance of a malignant neoplasm depends heavily on the composition of fat in the microenvironment and the adipose derived components available to it.

We aim to use 3D multicellular models to determine the interactions between adipocytes and tumour cells, along with their response to chemotherapies. By incorporating the intra-cellular and inter-cellular interactions within a tissue, our multiscale mathematical models give an insight into the possible expected outcomes of a patient.

2.2 Biological Experiment Outline

in vitro experiments were performed by experimental collaborators over four days using two cell lines [159]: OVCAR-3, a human ovarian epithelial carcinoma cell line [176] and SKOV-3, a human ovarian adenocarcinoma cell line [91]. Differences between profiles of 2D and 3D cultured populations were determined via RT-qPCR, immunoblots, and immunofluorescence. For protein analysis, immunoblotting was performed using primary antibodies against E-cadherin (clone G10, Santa Cruz Biotech) and N-cadherin (clone 13A9, Santa Cruz Biotech), with GAPDH (clone O411, Santa Cruz Biotech) used as a loading control for normalisation. For fluorescence analysis of tumour spheroids, immunostaining was carried out. In brief, an initial number of cells were cultured as spheroids using the hanging drop method and subsequently fixed in 4% PFA with 1% Triton in PBS for 3 hours at 4°C. After washing with PBS, spheroids underwent a dehydration and rehydration process through sequential exposure to increasing methanol concentrations (25%, 50%, 75%, and 95%) for 30 minutes each, followed by 100% methanol for 5 hours. The rehydration was achieved by reversing the methanol gradient back to 0% methanol and 100% PBS. Spheroids were blocked overnight at 4°C in PBST containing 3% BSA, followed by incubation with primary antibodies for E-cadherin (clone: EP700Y, Abcam) and N-cadherin (clone: 13A9, Santa Cruz Biotech) and fluorescent secondary antibodies Alexa Fluor® 555-conjugated polyclonal goat anti-rabbit antibody (ab150086, Abcam) and Alexa Fluor® 488-conjugated polyclonal goat anti-mouse antibody (ab150117, Abcam). Before imaging, spheroids were stained with Hoechst and mounted onto microscope slides for visualisation.

2D monolayers and 3D spheroid tumours were cultured and placed in the presence of either omental tissue-conditioned media (OT-CM), undifferentiated adipose-derived stem cells (U-ADSCs), or an unconditioned media (UCM) control. The presence of OT-CM was found to increase cell proliferation in all scenarios other than in OVCAR-3 spheroids, in which unconditioned media showed the highest cell luminescence after 96 hours, as shown in Figure 2.1.

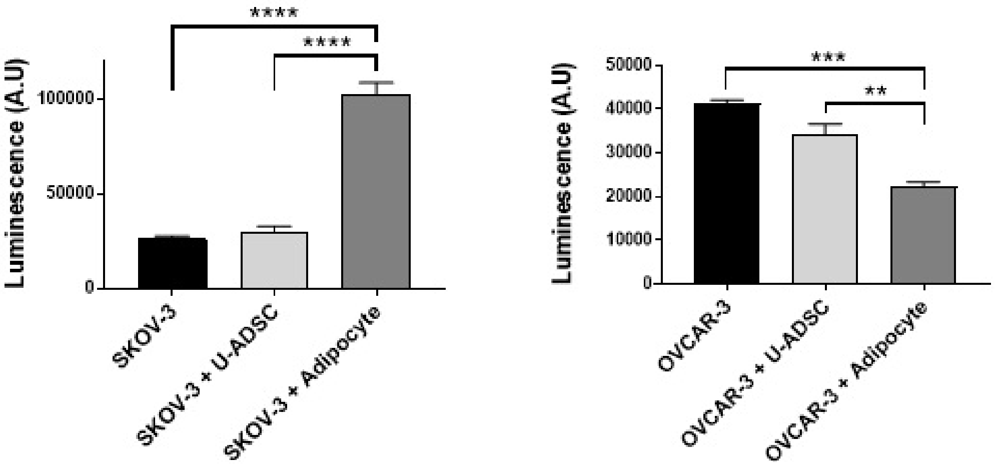

(A) (B)

FIGURE 2.1: **Final cell luminescence from the *in vitro* spheroid experiments** [159]. Cells are plated following co-culture with a control, undifferentiated adipose derived stem cells, and adipocytes. Populations of SKOV-3 (A) and OVCAR-3 (B) spheroids are taken after 96 hours, with the impacts of different types of media compared. SKOV-3 tumours co-cultured with adipocytes show an increased proliferation rate, while OVCAR-tumours co-cultured with adipocytes show a decreased proliferation rate when compared to the control.

Further experiments tracked the expression throughout the tumour of E-cadherin, a surface marker used for the identification of epithelial cells [34], and N-cadherin and vimentin, markers used to locate mesenchymal cells [164]. It was found that the SKOV-3 tumour had a high band intensity of N-cadherin and vimentin, markers associated with a mesenchymal phenotype, suggesting epithelial-to-mesenchymal transition (EMT) had been completed (See Figure 2.2). The OVCAR-3 tumour showed a higher expression of E-cadherin, thus suggesting that larger volumes of the neoplasm was made up of epithelial cells rather than mesenchymal.

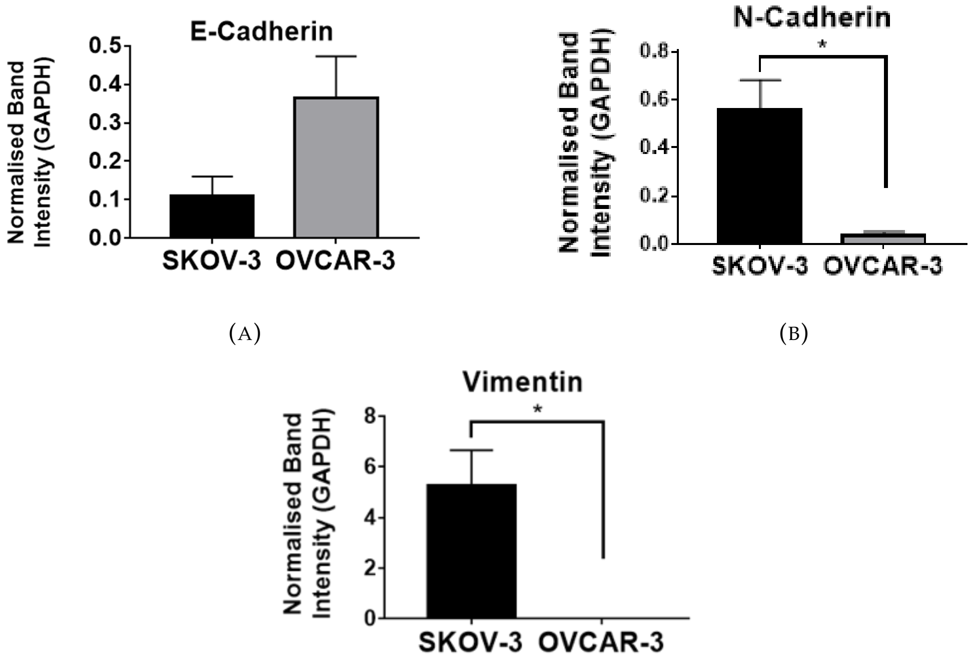

(A)

(B)

(C)

FIGURE 2.2: **Normalised band intensity found *in vitro* between SKOV-3 and OVCAR-3** [159]. Epithelial markers (E-cadherin) and mesenchymal markers (N-cadherin and vimentin) are expressed throughout the tumour after 96 hours. The intensities of these are normalised and compared for the different markers for SKOV-3 (black bars) and OVCAR-3 (grey bars) cell lines.

The cells on the periphery of the SKOV-3 spheroid are shown to express E-cadherin, suggesting an epithelial phenotype, while the interior cells appear to have a uniform, solely mesenchymal distribution. This tumour has a consistent structure, with only mesenchymal cells expressing N-cadherin in the centre and a thin layer of E-cadherin expressed by epithelial cells around the tumour periphery. Mesenchymal OVCAR-3 cells are arranged in small clumps scattered within a surrounding pool of epithelial cells to form the solid tumour (See Figure 2.3). Unlike SKOV-3 tumours, these mesenchymal cells are capable of forming through the tumour, including the periphery. These clumps of mesenchymal cells are thought to play a key role in metastasis, with their collective migration allowing these clumps to leave the primary tumour location and relocate elsewhere. The trends observed in Figure 2.2 support the images shown in Figure 2.3, implying the SKOV-3 spheroid is composed mostly of mesenchymal cells due to the tumour interior, while the OVCAR-3 spheroid is made up of primarily epithelial cells.

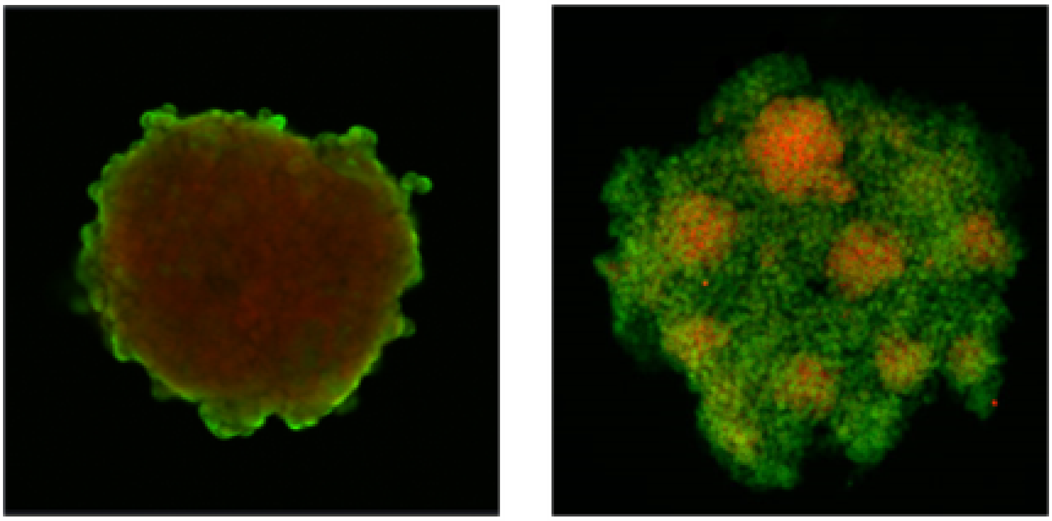

(A) SKOV-3

(B) OVCAR-3

Figure 2.3: **Final cadherin expressions in the cross-section of the tumours found *in vitro*** [159]. The spatial distribution of E-cadherin (green) and N-cadherin (red) is shown for SKOV-3 (A) and OVCAR-3 (B) spheroids after 96 hours.

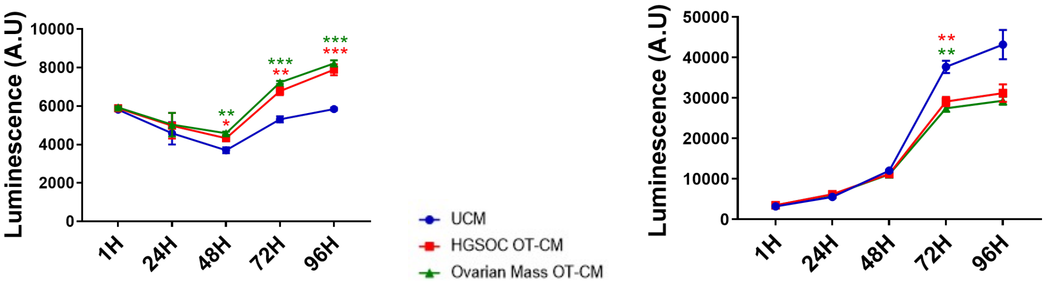

(A) SKOV-3

(B) OVCAR-3

Figure 2.4: **Temporal dynamics of SKOV-3 and OVCAR-3 tumours in various medias** [159]. Live cell populations are measured daily for 96 hours in unconditioned media (blue), high-grade serous ovarian cancer omental tissue conditioned media (red), and ovarian mass omental tissue conditioned media (green). SKOV-3 (A) tumours are initialised with 6000 cells and OVCAR (B) tumours with 3000 cells.

SKOV-3 cells appear to have a low proliferation rate, with an initial decrease in live cell populations and a slow increase during the final 48 hours of the *in vitro* experiments, as shown in Figure 2.4 (A). Omental tissue conditioned media is shown to increase the cycling rate of SKOV-3 cells, with cell populations in unconditioned SKOV-3 tumours consistently lower throughout the experiments. OVCAR-3 cells show opposite trends, with unconditioned media generally leading to the highest proliferation rate in OVCAR-3 cells (See Figure 2.4 (B)). Proliferation rates of OVCAR-3 cells are also considerably higher than those of SKOV-3, with around a tenfold increase in population sizes across four days.

2.3 Model Outline

To perform our *in silico* simulations, various dynamics will be implemented into a PhysiCell modelling framework. PhysiCell is a physics based platform employing two interacting layers to the simulation, one for the substrate concentrations and another for the cells (See Figure 2.5). The simulations will run on a 3D spatial domain that tracks the concentration of each substrate with user created initial and boundary conditions. The concentrations are recorded on a discrete mesh while the cells can move continuously across the domain. Different cell types can be placed and initialised, each secreting and uptaking different levels of substrates. The underlying dynamics of each cell's volume, mechanics, and motility can be defined by the user and adapted to fit the model created. Data collected experimentally will be used to find the previously undocumented values of parameters required for the model. Functional genomics will be incorporated by the properties of each cell being passed onto daughter cells.

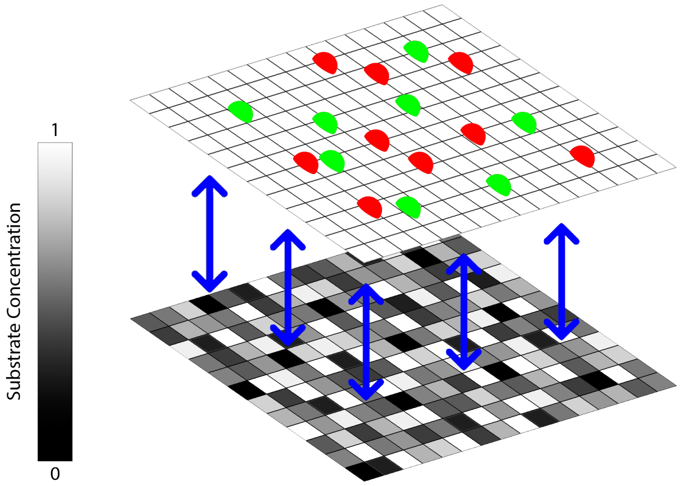

FIGURE 2.5: **Example grid layout for a 2D PhysiCell simulation.** Lighter shades on the bottom level of the visualisation show higher substrate concentrations diffusing according to Equation 2.1. Two different cell types slide along a plane on the top level based on the value of the cell velocity, $\mathbf{v}_i$, given in Equation 2.2.

BioFVM [72] is implemented to recreate the chemical microenvironment, in which multidimensional PDEs are implemented on a Cartesian mesh in Equation 2.1,

$$\frac{\partial \boldsymbol{\rho}}{\partial t} = \mathbf{D}\nabla^2\boldsymbol{\rho} - \boldsymbol{\lambda}\boldsymbol{\rho} + \mathbf{S}(\boldsymbol{\rho}^* - \boldsymbol{\rho}) - \mathbf{U}\boldsymbol{\rho} + \sum_{\text{cells } k} \delta(\mathbf{x} - \mathbf{x}_k) W_k [\mathbf{S}_k(\boldsymbol{\rho}_k^* - \boldsymbol{\rho}) - \mathbf{U}_k\boldsymbol{\rho}] \text{ in } \Omega. \tag{2.1}$$

Here, $\boldsymbol{\rho}$ is the vector of chemical substrates, $\mathbf{D}$ and $\boldsymbol{\lambda}$ are the diffusion coefficients and decay rates respectively. $\mathbf{S}$ and $\mathbf{U}$ are the bulk supply and bulk uptake function respectively, while $\boldsymbol{\rho}^*$ represents the vector of saturation densities for the substrates. The $\delta(\mathbf{x})$ term is the Dirac delta function, incorporated to include the source/sink points in the domain due to cell secretions/uptakes. W_k, $\mathbf{x}_k$, $\mathbf{S}_k$, $\mathbf{U}_k$, and $\boldsymbol{\rho}_k^*$ are the volume, position, source rates, uptake rates, and saturation densities respectively for the k^{th} cell.

The cells move off lattice within the 3D domain, Ω, based on adhesion, repulsion, and various motility rules. The forces acting upon each cell are shown in Equation 2.2, giving the velocity after each time step and updating the position of cell i subsequent to each iteration,

$$\begin{aligned} \mathbf{v}_i = \sum_{j \in \mathcal{N}(i)} \Bigg(& -\sqrt{c^i_{cca} c^j_{cca}} \nabla \phi_{1,R_{i,A}+R_{j,A}}(\mathbf{x}_i - \mathbf{x_j}) - \sqrt{c^i_{ccr} c^j_{ccr}} \nabla \psi_{1,R_{i,A}+R_{j,A}}(\mathbf{x}_i - \mathbf{x_j}) \Bigg) \\ & - c^j_{cba} \nabla \phi_{1,R_{j,A}}(-d(\mathbf{x}_i)\mathbf{n}(\mathbf{x}_j)) - c^i_{cbr} \nabla \psi_{1,R_i}(-d(\mathbf{x}_i)\mathbf{n}(\mathbf{x}_j)) + \mathbf{v}_{i,mot}. \end{aligned} \tag{2.2}$$

Each cell has a repulsion force acting between itself and the surrounding cells to prevent overlapping. The motility speed, $\mathbf{v}_{i,mot}$, is set to be two times higher for mesenchymal cells as it is for epithelial to attempt to qualitatively replicate the more metastatic behaviour of cells that have undergone EMT and is assigned a random direction.

Here, $\mathcal{N}(i)$ is the list of all cells in the domain capable of interacting with cell i. The magnitude of the cell-cell adhesion and repulsion forces are given by c^i_{cca} and c^i_{ccr} respectively, while the cell-basal membrane forces are given by c^i_{cba} and c^i_{cbr}. R_i is the radius of cell i and $R_{i,A}$ its maximum adhesion distance. Functions $\phi_{n,R}(\mathbf{x})$ and $\psi_{n,R}(\mathbf{x})$ are adhesion and repulsion functions, the details of which are defined in PhysiCell [73]. Finally, $\mathbf{n}(\mathbf{x})$ represents the normal vector to the nearest cell basal lamina and $d(\mathbf{x})$ the distance to it.

Several studies have investigated the composition of ovarian cancer spheroids. Capellero et al [25] reported that tumour cells exhibit a hybrid EMT phenotype, co-expressing epithelial and mesenchymal markers [25]. This partial EMT state is thought to improve the viability of spheroids and their adhesion within the peritoneal cavity. To incorporate this hybrid state in the modelling framework, cells are assigned a cadherin rating along a scale of their epithelial to mesenchymal phenotype running from zero (epithelial) to thirteen (mesenchymal), as illustrated in Figure 2.6. The maximum rating is set to thirteen to allow an equally weighted assignment of epithelial cells to ratings of 0-6 and mesenchymal to 7-13. Moreover, an average rating value for epithelial (three) and mesenchymal (ten) cells can be set as the default if required.

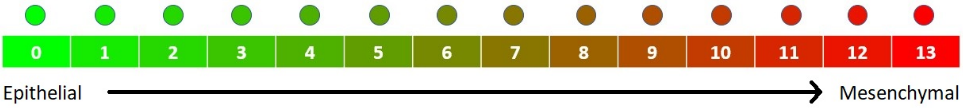

FIGURE 2.6: **Appearance of cells during the simulations based on their current cadherin rating.** Cells can take fourteen different values, with ratings 0-6 classified as epithelial and 7-13 classified as mesenchymal. There is an average rating of three for epithelial cells and ten for mesenchymal cells. The colour of each cell during the simulations represents where along this scale they are placed.

2.3.1 Cell Cycle and Death

The overall size of the tumour over time has a major impact on the likelihood of successful treatment for cancer patients. The rapid growth of cancer tumours is mainly due to the increased rate at which cancer cells can divide and multiply [111]. The cell cycle is split into four stages: gap 1 (G1), synthesis (S), gap 2 (G2), and mitosis (M) [154]. Three main DNA damage checkpoints are present throughout the cycle, located at the end of the phases G1, S, and G2 to ensure damage cannot be passed onto future generations [39]. Alongside these, an antephase checkpoint found between G2 and M ensures that environmental conditions such as oxygen levels and available surrounding space are favourable to support attempting cell division [183]. When arriving at a checkpoint, either the cell passes the checkpoint and continues the journey through the cell cycle, or fails at the checkpoint at which point the cell may initiate programmed cell death or enter quiescence, a state of reversible exit from the cell cycle [11]. The ability of cancer cells to avoid these checkpoints allows the cells to complete steps of the cycle faster and with higher chances of success, causing the tumours to form and progress so rapidly. The probability a cell progresses from stage i to j during an iteration in the model is given approximately by $r_{ij}\Delta t$, where r_{ij} is the transition rate from state i to j and Δt is the change in time. Including the cell cycle as a four stage process rather than using a single proliferation rate allows a more accurate determination of the population dynamics by including realistic influences of the cellular conditions on the cycling rate. Mesenchymal cells are assumed to leave the G1 stage of the cell cycle 50% slower than epithelial cells [167], as shown in Figure 2.7 (A). Based on an inspection of the experimental data shown in Figures 2.1 and 2.4, we assume for simplicity that a lack of media increases the proliferation rate of SKOV-3 cells [40] by 50% and decreases OVCAR-3 cells in spheroids [236] by 50%, shown in Figure 2.7 (B). This difference allows us to capture the phenomenon of adipose derived media increasing the tumour cell population compared to the control in SKOV-3 tumours, while decreasing it in OVCAR-3 tumours.

The increase in mitochondrial consumption of oxygen observed during the G1/S transition [63] suggests a dependence on oxygen in the microenvironment for the rate at which a cell leaves the G1 stage of the cell cycle. Therefore, variations in the cell cycle rate due to inter-cellular and intra-cellular conditions are incorporated into the G1 stage, with fixed rates of exiting stages S, G2, and M, shown in Table 2.1.

Cycle Durations	
Cell Cycle State	**Average Rate of Cycling Stage exit (1/mins)**
G1	Equation 2.3
S	1/480 [42]
G2	1/240 [42]
M	1/60 [42]

TABLE 2.1: **Average cycle durations.** Cells progress through four stages of cell cycle. The probability of cell cycle progression during an iteration can be estimated by multiplying the rate by the time length of the iteration.

As slower cycling cells are assumed to reach cycling checkpoints less frequently than faster cycling cells, the death rate is also assumed to be lower. The lifespan of cells in humans varies greatly from a timescale of days to years [196]. Higher concentrations of the drug paclitaxel in the microenvironment are assumed to lead to higher rates of apoptosis in the cells, as shown in Figure 2.7 (C) [227]. Treatment in the model is assumed to cause up to a 100-fold increase in apoptosis rate. Epithelial cells are more susceptible to treatment due to their faster cycling rate, while the mesenchymal cells are more resistant [21]. In our model, we assume an OVCAR-3 mesenchymal cell will have an average lifespan of around ten weeks, leading to a death rate of around 1×10^{-5} / min. In line with the difference in G1 cycling rate, we assume that SKOV-3 cells die ten times as slowly as OVCAR-3 cells as shown in Figure 2.7 (D). These death rates are explored in more depth during Chapter 4.

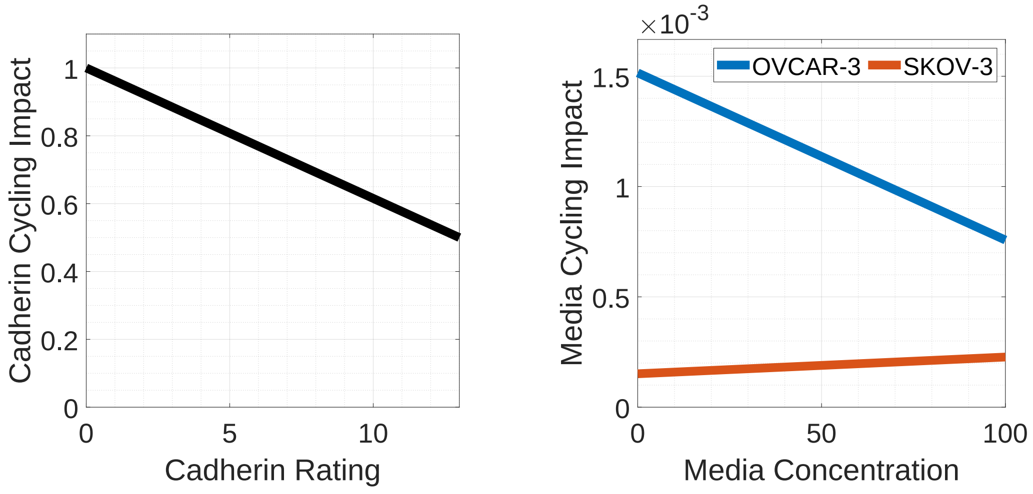

(A) Cadherin cycling impact parameter value, c_c.

(B) Media cycling impact parameter value, m_c.

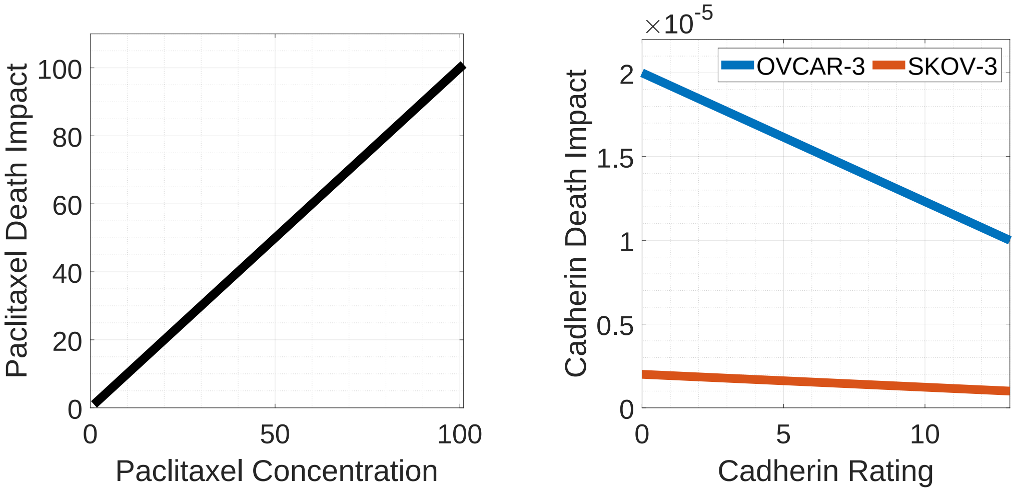

(C) Death rate for cells due to paclitaxel, p_d.

(D) Death rate for cells due to cell line and cadherin rating, c_d.

FIGURE 2.7: **G1 cycling and death rates for OVCAR-3 and SKOV-3 cells.** The relationships between cadherin rating and cycling rate (A), media concentration and cycling rate (B), paclitaxel concentration and apoptosis rate (C), and cadherin rating and apoptosis rate (D) are shown. OVCAR-3 relationships are shown in blue, SKOV-3 relationships in red, and those independent of the cell lines are shown in black.

Figure 2.7 shows the intra-cellular components and conditions in the microenvironment that are incorporated into cell cycling and death rates. The cadherin cycling impact, c_c, and media cycling impact, m_c, parameters are brought into the rate at which a cell leaves the G1 cycling stage using Equation 2.3,

$$r = c_c \cdot m_c. \tag{2.3}$$

Later in the chapter we will briefly compare the tumour growth with and without chemotherapy treatment with a set of basic rules. When treatment is included, paclitaxel is added uniformly throughout the domain after 24 hours, during which all voxels are assigned a paclitaxel concentration of 50mg. Paclitaxel is assumed to remain at a constant concentration throughout the remainder of the experiment. The paclitaxel death impact, p_d, and cadherin death impact, c_d, parameters are incorporated into the rate at which a cell can undergo apoptosis using Equation 2.4, with the probability of death occurring during the interval $[t, t + dt]$ being $d \cdot dt$,

$$d = p_d \cdot c_d. \tag{2.4}$$

2.3.2 Role of the Bystander Effect

Based on the observations in Figure 2.3, here we develop a model that incorporates the emergence of small mesenchymal clusters within a predominantly epithelial population of OVCAR-3 cells, as these clusters are crucial for correctly replicating the spheroid behaviour. In our model, we simulate a bystander effect, where epithelial cells near mesenchymal cells upregulate cadherin expression in response to local signalling cues, reflecting the influence of mesenchymal cells on surrounding epithelial populations [133, 103].

In this context, bystander effects are the cumulative effects of various factors such as cytokines, growth factors, and exosomes secreted by cancer cells [140]. In the model, the bystander effect is responsible for the formation of the disjoint mesenchymal clumps observed in the OVCAR-3 hybrid tumour population, co-expressing epithelial and mesenchymal markers [217]. We assume that these bystander effects encourage epithelial cells in their proximity to undergo EMT. To achieve this phenomenon, we include another substrate into the model. Mesenchymal cells which have undergone EMT are set to secrete a bystander signal [140] up to a rate of 100 units per minute, representing the percentage of the maximum secretion possible by cells, as shown in Figure 2.8. We assume that the signal secretion rate is increased with cadherin rating, meaning epithelial cells in the presence of mesenchymal cells are exposed to a higher concentration of signal and are more likely to increase in cadherin rating themselves, inducing the bystander effect. These factors secreted by mesenchymal cells help encourage changes in the cell phenotype and increases the rate at which cells undergo EMT [133, 103]. This creates localised pockets of mesenchymal clusters in which high amounts of these secreted factors are present, further encouraging EMT in the surrounding cells. Such tumour heterogeneity is apparent in solid tumours where spatially organised expressions of cadherins have been described in both primary and secondary epithelial ovarian cancer tumours [4, 122].

The voxel in which a mesenchymal cell is located fills with this signal due to the high secretion rate, remaining with a high concentration as long as the mesenchymal cell resides within it. A very low substrate diffusion coefficient (1 micron^2/min) is included for the signal to keep the range of influence low, along with a signal decay rate of 1 unit per minute to avoid a build up of signal in voxels which no longer host mesenchymal cells. A Hill function is used to ensure there is a small secretion rate for cells of a low cadherin rating while still allowing a high secretion rate for mesenchymal cells. This Hill function has a half max set at 6.5, since this is half the value of the maximum cadherin rating (13) that cells can reach during the simulation. The saturation value is set to 100 units, at which point signal saturation is assumed to be reached. The Hill power is set to four, optimised across simulations using observations from the experimental images shown in Figure 2.3.

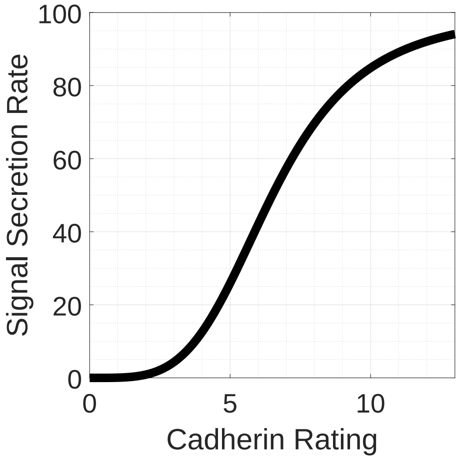

FIGURE 2.8: **Signal secretion rate for cells dependent on their current cadherin rating.** Cells at a higher cadherin rating with a more mesenchymal-like phenotype encourage epithelial cells in their proximity to undergo EMT. This is done by secreting a signal with low diffusion into the microenvironment to increase the rate of EMT.

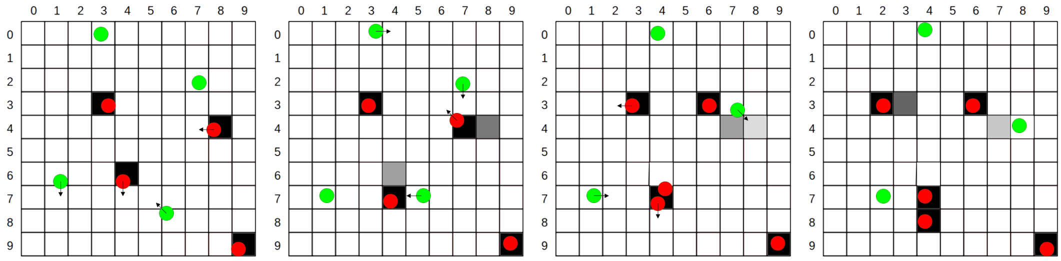

(A) Time Step 0 (B) Time Step 1 (C) Time Step 2 (D) Time Step 3

FIGURE 2.9: **Example of the signal concentration during a simulation.** Red mesenchymal cells secrete a chemical signal, shown by darker shades in the voxel. This signal encourages EMT in epithelial cells according to Equation 2.5. The signal slowly decays over time following the departure of the mesenchymal cell from the voxel.

Figure 2.9 shows an example of four time steps taken from a minimalistic simulation. Mesenchymal (red) and epithelial (green) cells are initialised in a 2D domain made up of 100 voxels, with cells moving continuously off lattice. The arrows from the cell in the diagram show where the cell is moving and the compartment of the grid that the cell will be in at the next time step. The shade of a voxel shows the concentration of the signal at the time point (black indicates maximum signal and white indicates no signal). When the grid square is vacant of mesenchymal cells the signal immediately begins to decay from that compartment and the concentration decreases.

2.3.3 Intra-Cellular and Inter-Cellular Impacts on EMT

Cells have been observed to show the highest phenotypic plasticity when only partial EMT has been completed, with the most stable cells found to be either purely epithelial or purely mesenchymal [215]. To include this, a cadherin EMT impact parameter, c_e, is introduced, shown in Figure 2.10 (A). Alongside this, cells in low levels of oxygen are more likely to jump up a cadherin rating and perform EMT than those which are not [36, 110]. We introduce an oxygen EMT impact parameter, o_e, in Figure 2.10 (B). The oxygen EMT impact parameter decreases as oxygen levels increase, saturating at zero when oxygen concentration increases above 1 unit. Adipose derived media and signal secreted by mesenchymal cells are both assumed to encourage EMT in epithelial cells [129]. This phenomenon is incorporated into the model using a media EMT impact parameter, m_e, and a signal EMT impact parameter, s_e in Figures 2.10 (C) and (D) respectively. These parameters are positively correlated to the concentration of their respective substrate, with saturation being reached at concentrations of 100 units of media and 20 units of signal.

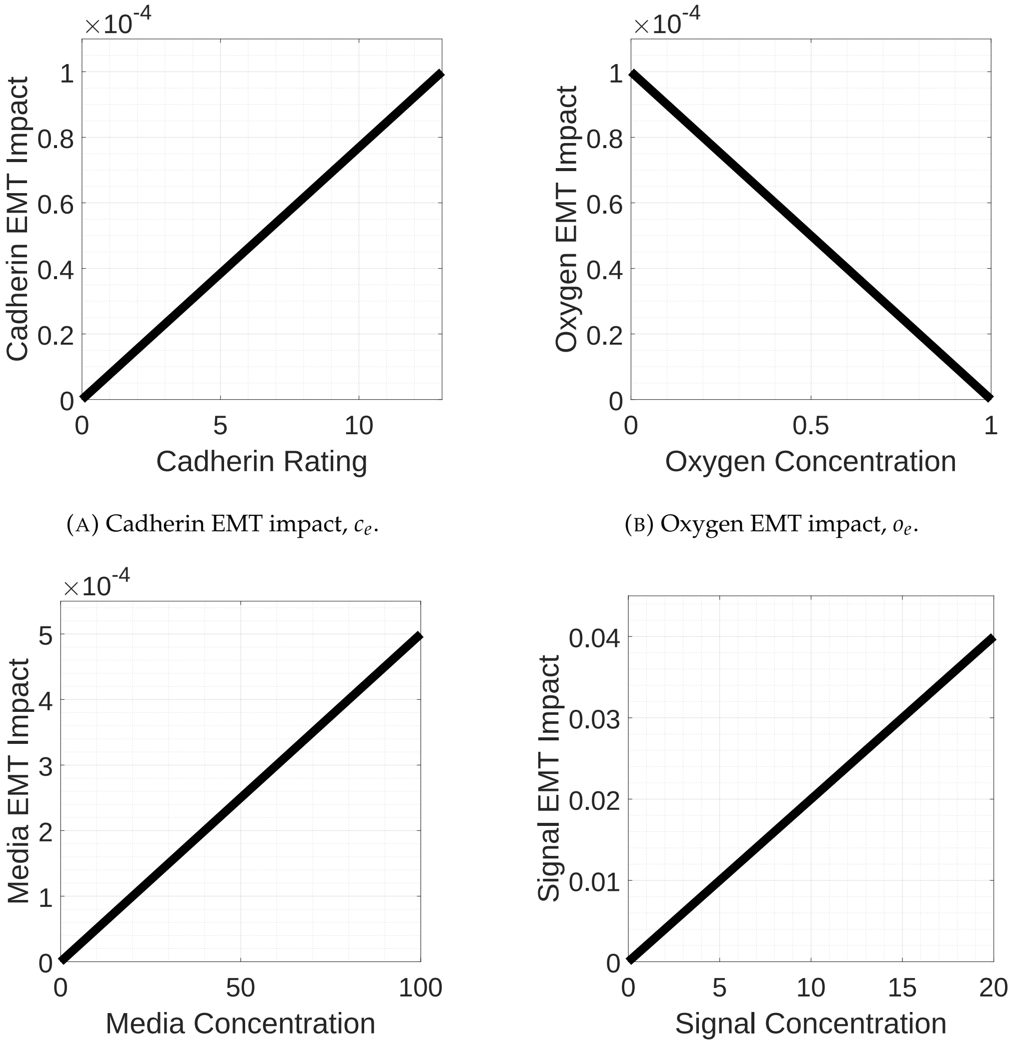

(A) Cadherin EMT impact, c_e.

(B) Oxygen EMT impact, o_e.

(C) Media Rate parameter value, m_e.

(D) Signal Rate parameter value, s_e.

FIGURE 2.10: **EMT rate variables with respect to the intra and inter-cellular conditions.** The impact of the cadherin rating (A), oxygen concentration (B), media concentration (C), and signal concentration (D) on the rates of EMT in cells. These variables are included in calculating the probability of EMT on each iteration using Equation 2.5.

All impact parameters are incorporated into calculating the probability for a cell to jump up a cadherin rating, thus ensuring the conditions lead to an impact on the rates of EMT. The parameter values are incorporated for each cell using a probabilistic approach, viewing them as a set of independent variables and calculating the probability of their union as shown in Equation 2.5. Here, p is the probability that a cell will jump up a cadherin rating on each six minute iteration,

$$p = 1 - (1 - c_e) \cdot (1 - o_e) \cdot (1 - m_e) \cdot (1 - s_e). \tag{2.5}$$

We ensure the cells on the periphery of the SKOV-3 3D spheroids remain epithelial, as observed in the biological observations, by incorporating a "transformation threshold" parameter, set in the model to be 0.1 units of oxygen. Any SKOV-3 cells in oxygen levels greater than this value are automatically reassigned a cadherin rating of 0. This prohibits the cells on the exterior of the tumour from undergoing EMT and ensures they remain epithelial to replicate the biological experiments in which a shell of epithelial cells is wrapped around an interior mass of mesenchymal cells. A summary of the key differences between the cell lines are shown in Table 2.2.

OVCAR-3	**SKOV-3**
Lower Probability of EMT	Higher Probability of EMT
All cells can perform EMT	Only Interior cells can perform EMT
Faster cell cycling rates	Lower cell cycling rates

TABLE 2.2: **Key cell type differences.** Comparisons between the two cell lines of interest are shown, inferred from the biological experiments shown in Section 2.2. SKOV-3 cells have higher rates of EMT, slower proliferation rates, and retain a shell of epithelial cells along the tumour exterior.

2.3.4 Parameter Values

The key parameters for our model, such as cell-cell adhesion strengths and substrate secretion/uptakes are stated in Tables 2.3 and 2.4. For simplicity, we currently keep cell volumes, repulsion and adhesion strengths, and substrate uptake rates equal between epithelial and mesenchymal cells. Cell adhesion ($0.4\mu m/\text{min}$) and repulsion ($10.0\mu m/\text{min}$) strength parameter values are kept consistent with those used in the PhysiCell template project [73]. These values help ensure there is no overlapping of the cell membranes whilst also keeping the tumour as one collective mass.

In simulations with adipocyte derived media, we initialise the domain with 50 dimensionless units of media distributed uniformly. Oxygen enters the system immediately using Dirichlet boundary conditions set to 38 units from each boundary edge. Epithelial and mesenchymal cells in both cell lines are each set to uptake oxygen at a rate of 0.6 units per minute and media at a rate of 0.001 units per minute in the model [79], removing the respective amount of substrate from the cells voxel as a sink. Oxygen and media have diffusion coefficients of 1e5 micron^2 and 200 micron^2 per minute respectively, assigned after observations of simulation results. Due to the short time frame of the experiments, we set the decay rate of oxygen and media to be zero, anticipating that minimal decay would occur in biological experiments.

Parameter	**Units**	**Value**
Cell Volume	microns^3	3000 [43]
Cell Adhesion Strength	micron/min	0.4
Cell Repulsion Strength	micron/min	10
Motility Speed	micron/min	0.1 [151]
Oxygen Uptake rate	1/min	0.6 [79]
Media Uptake rate	1/min	0.01

TABLE 2.3: **Cell parameter values.** Values are estimated using data provided in literature or inferred from comparing simulation results to biological observations.

Despite the constant influx of oxygen incorporated from the boundary edges through Dirichlet boundary conditions, the oxygen intake from the cells can create simulated hypoxic conditions in the tumour core, resulting in a higher probability of EMT occuring. Adipose derived media has less direct involvement than oxygen for cellular respiration and so the cell uptake rate is set to be considerably lower. We see in the biological experiments that the impact of media on the proliferation rate remains relatively high throughout the 96 hour *in vitro* experiment, also suggesting a low uptake rate of media in the cells. Setting an uptake value of 0.001 units per minute ensures that central areas of the tumour can become media deficient and cells on the periphery proliferate the fastest as a result. Parameter values can found in Table 2.3.

Oxygen and adipose derived media are assumed to each have no decay rate due to the short time frame of the simulation. The only reduction in the levels of these substrates is due to the uptake rate of the cells shown in Table 2.3 for processes such as glycolysis in respiration. The media is placed in the domain uniformly at the beginning of the simulation to immediately encourage cell proliferation. No further media is added during the simulation, resulting in a gradual decrease in overall media levels. There is an input of oxygen from the boundary edges to recreate the environment found in the *in vitro* experiment. This is implemented using Dirichlet boundary conditions along all faces of the 3D cube shaped domain. Media and signal substrates are assigned Neumann boundary conditions with a flux of zero along the boundary edges. Values for these parameters can be found in Table 2.4. Parameters not stated in this section were kept as the default PhysiCell parameter values from the template project provided [73].

Parameter	Units	Oxygen	Media	Signal
Diffusion coefficient	micron^2/min	1e5 [127]	200	0
Decay rate	1/min	0	0	1
Dirichlet/Neumann Boundary Conditions	dimensionless	38	0	0

TABLE 2.4: **Substrate parameter values.** Boundary conditions which are non zero use Dirichlet boundary conditions and those which are zero use Neumann boundary conditions with zero flux. Bystander signal related parameters are determined based purely on simulations observations due to the lack of physical substrate found experimentally.

2.4 Model Calibration

To ensure our model gave similar qualitative results to the biological experiments, we ran computer simulations to compare the tumour growth in unconditioned media and omental tissue conditioned media. Tumours are initialised as closely to the *in vitro* experiments as possible. The simulated tumours were placed in 3D spheroids in a cube-shaped domain with edges of length 410μm. OVCAR-3 cells were initialised with 3000 cells in a sphere of radius 120μm, while SKOV-3 cells were initialised with 6000 cells in a sphere of radius 150μm. We ran the simulations for 96 hours of simulated time, storing cellular and microenvironment data every 60 minutes.

The *in vitro* SKOV-3 tumour shown in Figure 2.3 (A) and repeated in Figure 2.11 (A) shows a large central mass of mesenchymal cells in which there is a high expression of N-cadherin, with an exterior shell of green epithelial cells formed around the periphery. *in vitro* OVCAR-3 tumours shown in Figure 2.3 (B) and repeated in Figure 2.11 (D) are shown to have small clumps of mesenchymal cells in the mass of otherwise epithelial cells. Both these trends are generally recreated in the results from the model simulations for SKOV-3 and OVCAR-3 spheroids shown in Figures 2.11 (B) and (E) respectively. To investigate the importance of the bystander effect, the simulations are repeated with no bystander signal secretion enabled from mesenchymal cells, with results shown for SKOV-3 tumours in Figure

2.11 (C) and OVCAR-3 tumours in Figure 2.11 (F). The lack of EMT in these results highlights the need for the bystander effect to be present in the model dynamics.

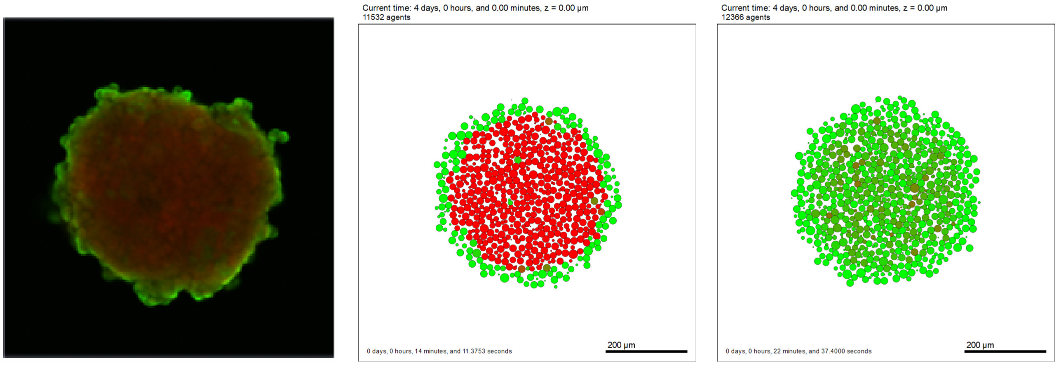

(A) Experimental SKOV-3 tumour after 96 hours.

(B) Simulated SKOV-3 tumour after 96 hours with the bystander effect.

(C) Simulated SKOV-3 tumour after 96 hours with no bystander effect.

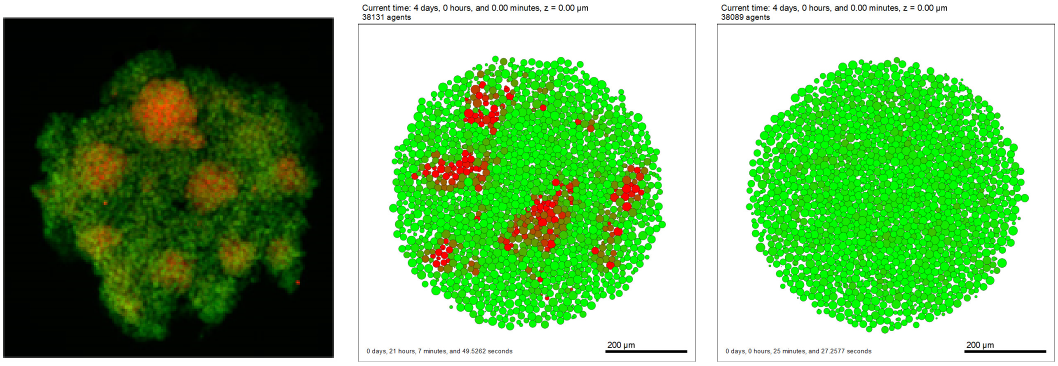

(D) Experimental OVCAR-3 tumour after 96 hours.

(E) Simulated OVCAR-3 tumour after 96 hours with the bystander effect.

(F) Simulated OVCAR-3 tumour after 96 hours with no bystander effect.

FIGURE 2.11: **Comparisons of the final cadherin expressions in the cross-section of the tumours found *in vitro* and *in silico*.** The spatial distribution of E-cadherin (green) and N-cadherin (red) is shown *in vitro* for SKOV-3 (A) and OVCAR-3 (D) spheroids after 96 hours, and compared with those found *in silico* for SKOV-3 (B) and OVCAR-3 (E). Simulations are also tested without the presence of the bystander effect in EMT, shown for SKOV-3 (C) and OVCAR-3 (F) tumours.

Figure 2.12 shows the live cell populations over time for the *in silico* and *in vitro* experiments in different types of media. The red lines represent tumours grown in omental tissue-conditioned media, with the blue lines showing tumour growth in unconditioned media. The green lines shows tumour population grown in ovarian mass omental tissue-conditioned media, not used in the *in silico* model for simplicity. Figure 2.12 (A) shows that omental tissue conditioned media helps to increase cell proliferation when compared with unconditioned media in SKOV-3 spheroids, with similar dynamics captured in the results of the *in silico* experiments shown in Figure 2.12 (C).

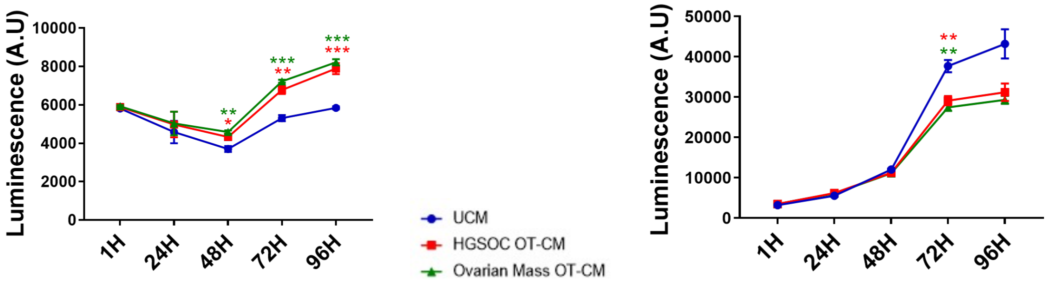

(A) Experimental Luminescence of a SKOV-3 tumour over 96 hours.

(B) Experimental Luminescence of a OVCAR-3 tumour over 96 hours.

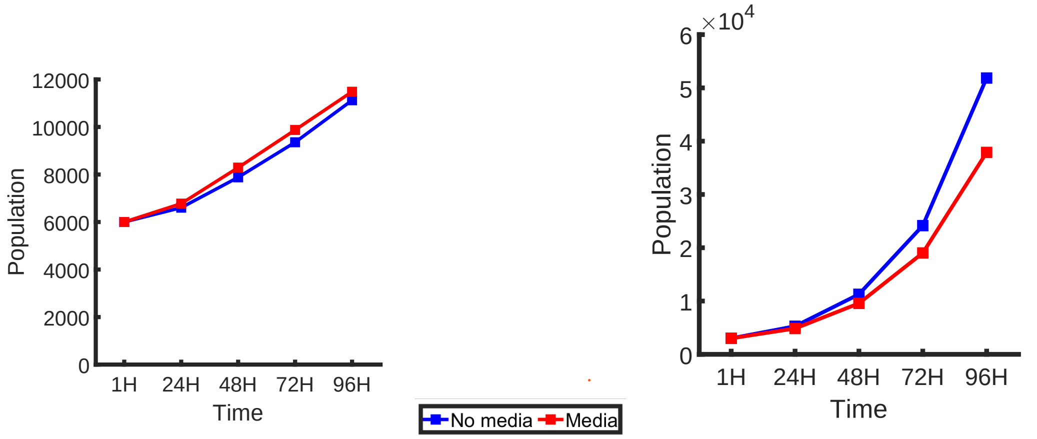

(C) Simulated Luminescence of a SKOV-3 tumour over 96 hours.

(D) Simulated Luminescence of a OVCAR-3 tumour over 96 hours.

FIGURE 2.12: **Comparison of temporal dynamics of tumours in various medias found *in vitro* and *in silico*.** Results found from in vitro experiments are shown for SKOV-3 tumours (A) and OVCAR-3 tumours (B). Simulations are run for 96 hours in with no initial media concentration (blue) and with an initial media concentration of 50 units (red). These tumours are simulated for SKOV-3 cells (C) and OVCAR-3 cells (D), and compared with the results found *in vitro* for the two cell lines.

The opposite effect is observed in OVCAR-3 spheroids, in which proliferation decreased as a result of omentum derived media being present in the *in vitro* experiments, as shown in Figure 2.12 (B), with simulation results shown in panel (D). While the exact shapes of the population curves during the simulation differ, the general trends are similar between the biological experiments and model simulations. Developing a model with a higher quantitative agreement rather than qualitative by including certain aspects such as a carrying capacity and further parameter optimisation is explored in more detail later in the study.

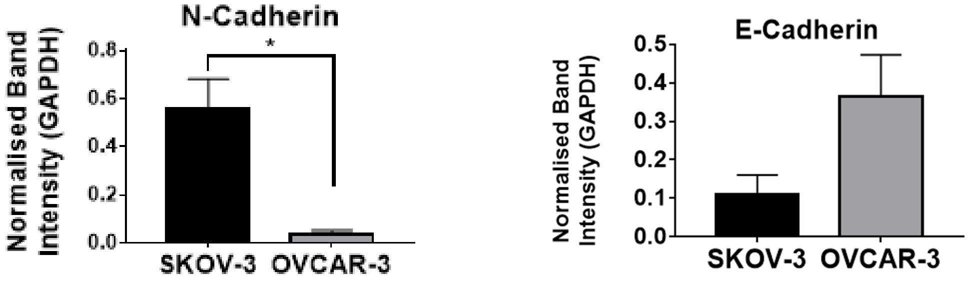

(A) Experimental N-cadherin band intensity after 96 hours.

(B) Experimental E-cadherin band intensity after 96 hours.

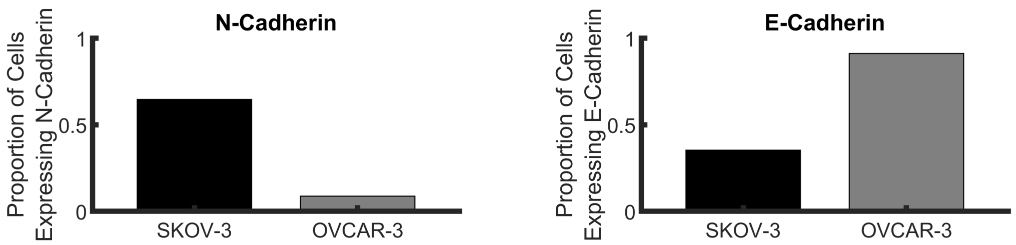

(C) Simulated number of cells expressing N-cadherin after 96 hours as a proportion of the total tumour.

(D) Simulated number of cells expressing E-cadherin after 96 hours as a proportion of the total tumour.

FIGURE 2.13: **Comparison of the N-cadherin and E-cadherin expression found *in vitro* and *in silico*.** Results found from *in vitro* experiments show the expression of N-cadherin (A) and E-cadherin (B) after 96 hours. These are compared with the *in silico* results in panels (C) and (D) for the two cell lines in which cells with a cadherin rating of seven or higher are assumed to express N-cadherin, and cells with a cadherin rating lower than seven are assumed to express E-cadherin.

We also compare the number of cells expressing mesenchymal and epithelial markers in the spheroids. After 96 hours of simulated time, the proportion of mesenchymal cells and epithelial cells in OVCAR-3 and SKOV-3 tumours were calculated, as shown in Figure 2.13. The high expression of N-cadherin and low expression of E-cadherin in SKOV-3 tumours found experimentally (top row), shown using black bars, is generally captured very well by the model results (bottom row). OVCAR-3 tumours show very low N-cadherin expression and high E-cadherin expression following biological experiments, shown using grey bars. These results are also found in the computer simulations we perform, with similar proportions of tumour expressions observed across the *in vitro* and *in silico* results.

This section helps to test the validity of the hypotheses we used to construct the model, with Figures 2.11, 2.12, and 2.13 showing strong similarities between the *in silico* and *in vitro* experiments. General trends in simulation results are consistently captured when compared to the data provided from the *in vitro* experiments. Ensuring our model has this calibration with the biological experiments provides the foundation to build from this model with the assumption that the results are accurate and realistic to what could be expected *in vitro*.

2.5 Results and Discussions

To explore the capabilities of the model, we begin to test the impact that three parameters can have on tumour growth and the final size of the neoplasm. Firstly we vary the media in the initial conditions. This aims to show what may be expected of a tumour in patients varying from lean to obese, with the previous sections highlighting the importance of incorporating the volume of adipose tissue into the model. Investigating this impact in more detail could lead to a better understanding of the exact tumour attributes expected for different patients. We next introduce the drug treatment described in Section 2.3.1 to test the effectiveness of different drug dosages on a tumour. These results can be incorporated to study the dosage a patient should be administered with, given their obesity level or tumour composition. Finally, we compare the tumour growth for different initial sizes. This may lead to interesting dynamics when incorporating media, since larger tumours will restrict the adipose derived media available to the central cells, changing the growth over time and potentially playing a role in determining the optimal treatment strategy.

2.5.1 Effect of Media Concentration on Tumour Growth

To explore the impacts of adipose tissue and the omentum, we vary the levels of adipose derived media in the initial conditions of the microenvironment between different values. All parameters remain the same as stated previously other than the initial media concentration, assigned the default value of 50 units distributed uniformly throughout the domain. We vary this parameter value between 0% and 200% of the default value shown in Figures 2.14 for OVCAR tumours and 2.15 for SKOV-3 tumours, with the cross-sections at the final time displayed alongside the temporal dynamics of the populations for each setting.

OVCAR-3

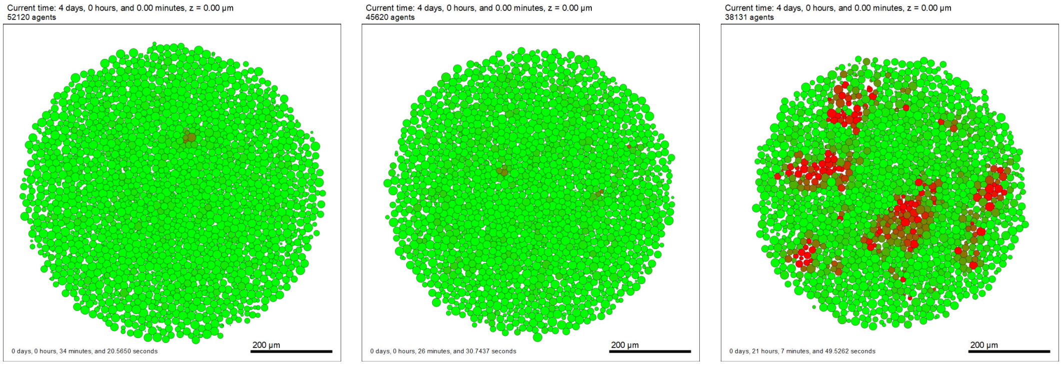

(A) 0% of the default initial media concentration value.

(B) 50% of the default initial media concentration value.

(C) 100% of the default initial media concentration value.

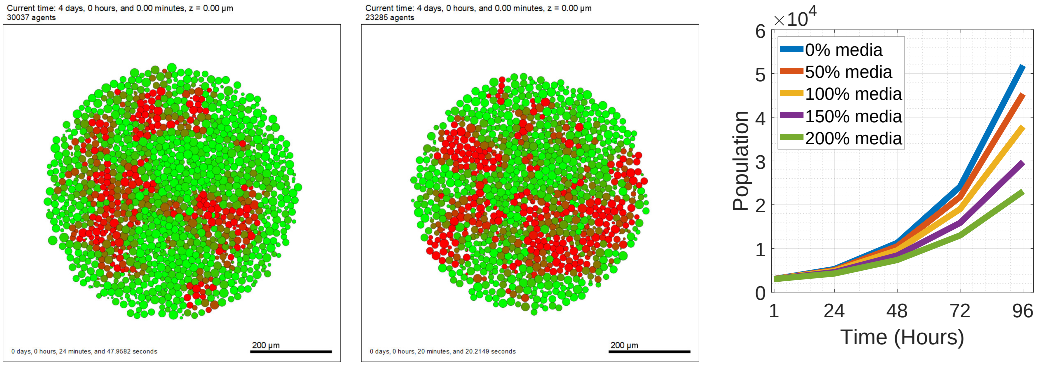

(D) 150% of the default initial media concentration value.

(E) 200% of the default initial media concentration value.

(F) Population of cells for different levels of media over time.

FIGURE 2.14: **OVCAR-3 spheroids after 96 hours of simulated time for different levels of media concentration.** Cross-sections of the OVCAR-3 tumours after 96 hours are shown for spheroids initialised with no media (A), 50% of the default media concentration (B), 100% of the default media concentration (C), 150% of the default media concentration (D), and 200% of the default media concentration (E). The temporal dynamics of these simulations show the live cell populations over time (F).

Figure 2.14 shows the tumour layout for OVCAR-3 spheroids after 96 hours in different media levels. For adipose derived media levels at 0% and 50% of the default value (panels (A) and (B) respectively), there are insufficient media to allow EMT to occur and the tumour ends with almost only epithelial cells present. The population of mesenchymal cells increases with levels of media, leading to the eventual merging of separate clumps as seen in Figures 2.14 (D) and 2.14 (E). We see that the total population of cells at the final time of the simulation decreases monotonically as initial media conditions increase (F). While these results may suggest that increased fat levels may be beneficial due to less overall tumour growth over time, mesenchymal cells have a higher tendency to metastasise and are considered to be harder to control and treat than epithelial cells. Therefore, it is likely that tumours in lower adipose derived media are easier to treat despite their larger size.

SKOV-3

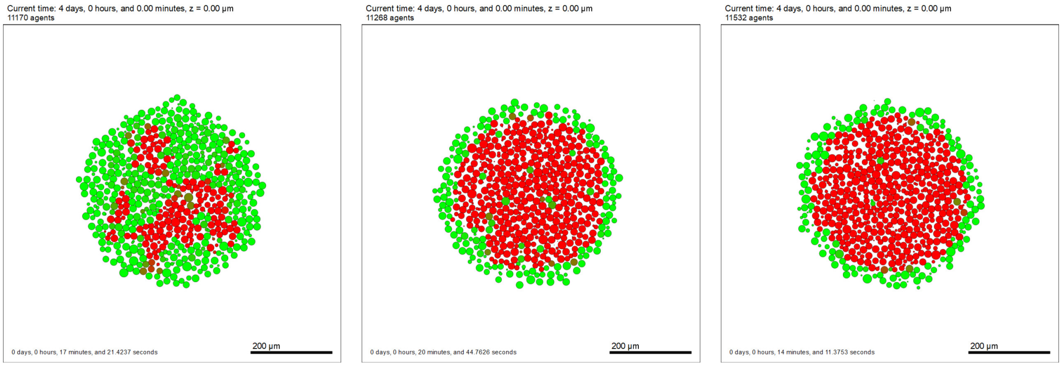

(A) 0% of the default initial media concentration value.

(B) 50% of the default initial media concentration value.

(C) 100% of the default initial media concentration value.

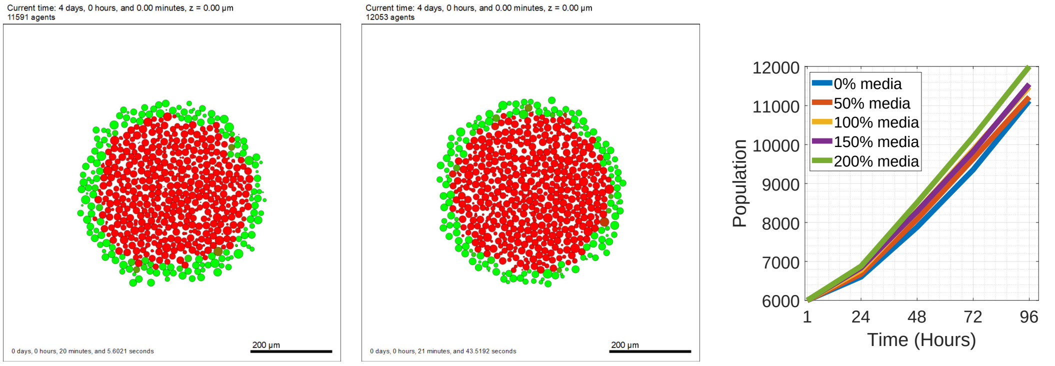

(D) 150% of the default initial media concentration value.

(E) 200% of the default initial media concentration value.

(F) Population of cells for different levels of media over time.

FIGURE 2.15: **SKOV-3 spheroids after 96 hours of simulated time for different levels of media concentration.** Cross-sections of the SKOV-3 tumours after 96 hours are shown for spheroids initialised with no media (A), 50% of the default media concentration (B), 100% of the default media concentration (C), 150% of the default media concentration (D), and 200% of the default media concentration (E). The temporal dynamics of these simulations show the live cell populations over time (F).

Figure 2.15 shows that only when no adipose derived media is present do simulations of SKOV-3 tumours remain fairly epithelial after 96 hours. All other initial conditions in the microenvironment lead to outcomes in which the interior of the tumour is almost entirely mesenchymal with an epithelial exterior. Other than occasional individual cells, visually there are few major differences from (B) to (E) in Figure 2.15. Panel (F) shows there is a small change in the total population of cells over time for different media conditions. Higher media consistently leads to a slightly larger tumour size at the end of the simulation. This is as a result of the increased proliferation rate that adipose derived media has on SKOV-3 cells.

2.5.2 Effect of Treatment Dosage on Tumour Growth

We next look for any potential impacts of administering treatment to a patient, with results shown in Figure 2.16 for OVCAR-3 and Figure 2.17 for SKOV-3 spheroids. The default drug amount is set to be 50 units delivered after 24 hours, with the dosage again varying between 0% and 200% of the default value and cell populations tracked over time for the different levels of treatment.

OVCAR-3

Figure 2.16 shows the final OVCAR-3 spheroids after being exposed to different concentrations of drug during the simulations. No level of drug we tested was sufficient in eradicating the tumour entirely, despite leading to a significant decrease in size overall. Alongside this, the drug has a higher capability of killing the epithelial cells over the mesenchymal cells, allowing the mesenchymal cells to remain and in general make up more of the final tumour. Tumours made up of mesenchymal cells are generally more resistant to treatment than those made up of epithelial cells. This leads to the question of whether higher drug dosages are always preferential, as the tumour can recover when the treatment is no longer active regardless of the dosage. Any negative side effects are often dosage dependent, meaning extra care is required when deciding on a treatment plan for cancer patients. Despite only a single administration of the drug, concentrations appear to remain sufficiently substantial at high dosages to continue reducing the populations in the OVCAR-3 tumour until the simulation is complete. Dosages at 100% or more of the default value show a monotonic decrease in cell populations following drug administration, suggesting that with enough time there may be potential to eradicate the tumour completely.

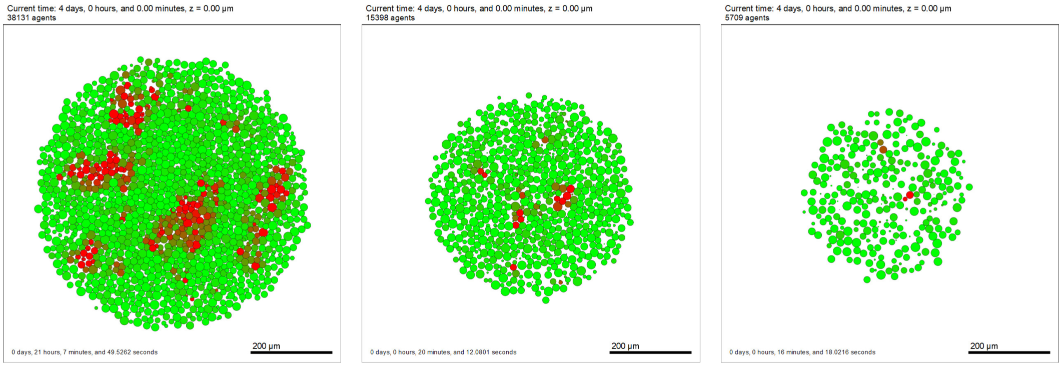

(A) 0% of the default drug treatment dosage.

(B) 50% of the default drug treatment dosage.

(C) 100% of the default drug treatment dosage.

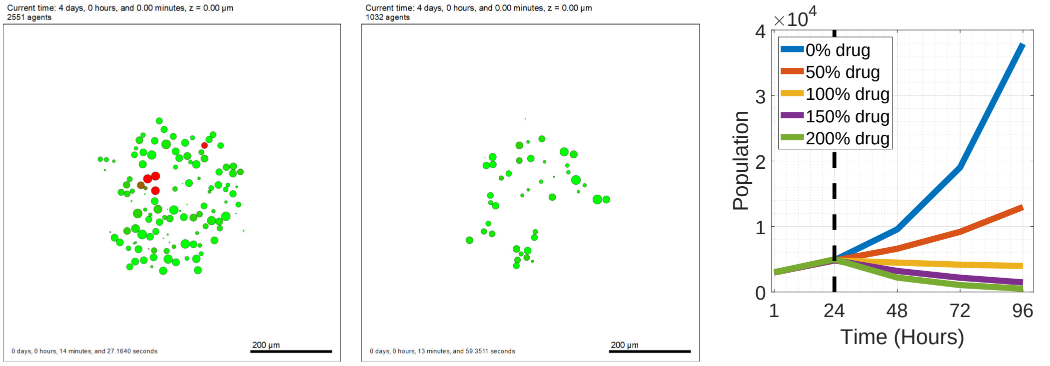

(D) 150% of the default drug treatment dosage.

(E) 200% of the default drug treatment dosage.

(F) Population of cells for different levels of drug dosage over time.

FIGURE 2.16: **OVCAR-3 spheroids after 96 hours of simulated time for different levels of treatment.** Cross-sections of the OVCAR-3 tumours after 96 hours are shown for spheroids with no treatment (A), 50% of the default treatment dosage (B), 100% of the default treatment dosage (C), 150% of the default treatment dosage (D), and 200% of the default treatment dosage (E). The temporal dynamics of these simulations show the live cell populations over time (F), with the dashed vertical line at 24 hours showing the introduction of treatment.

SKOV-3

We next investigate the impact of the drug on SKOV-3 cells. Figure 2.17 shows the tumour appearance after 96 hours of the simulation. Again, no treatment level tested in the simulations led to the complete removal of the tumour, with even any reduction over time in the population size found to be unachievable. The drug targets the epithelial cells on the periphery, stripping the tumour of its outside layer, thus increasing the oxygen levels to the previously interior cells. This converts the outside mesenchymal cells into epithelial cells due to the increased oxygen levels available to these cells and the oxygen threshold rules imposed on SKOV-3 cells in the model. As a result, the tumour shrinks over time while simultaneously keeping the lining of green epithelial cells on the tumour periphery.

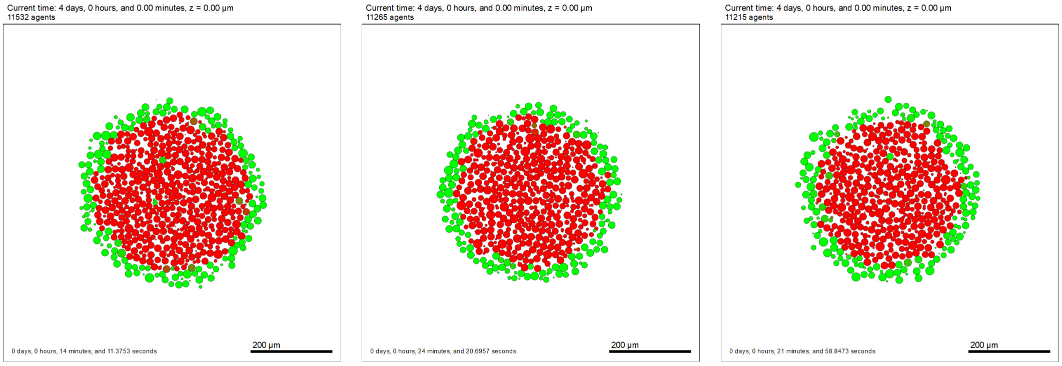

(A) 0% of the default drug treatment dosage.

(B) 50% of the default drug treatment dosage.

(C) 100% of the default drug treatment dosage.

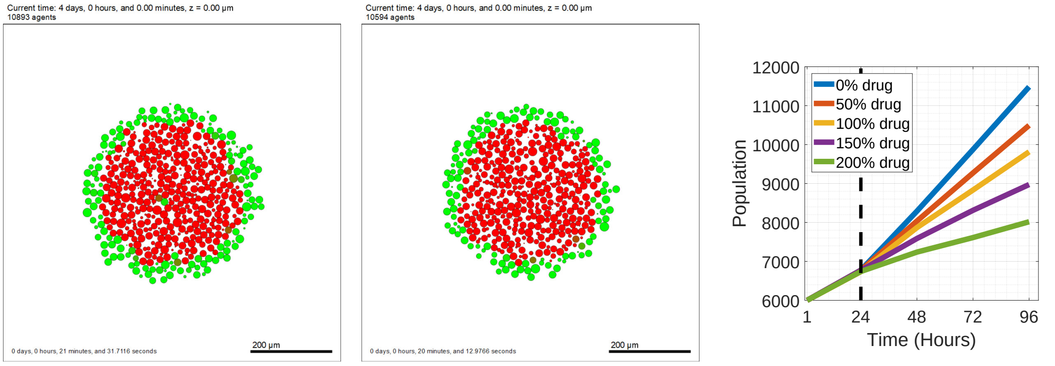

(D) 150% of the default drug treatment dosage.

(E) 200% of the default drug treatment dosage.

(F) Population of cells for different levels of drug dosage over time.

FIGURE 2.17: **SKOV-3 spheroids after 96 hours of simulated time for different levels of treatment.** Cross-sections of the SKOV-3 tumours after 96 hours are shown for spheroids with no treatment (A), 50% of the default treatment dosage (B), 100% of the default treatment dosage (C), 150% of the default treatment dosage (D), and 200% of the default treatment dosage (E). The temporal dynamics of these simulations show the live cell populations over time (F), with the dashed vertical line at 24 hours showing the time of treatment introduction.

No drug concentration tested for either cell line is sufficient to completely eradicate the tumour over time. While simulated tumour populations decrease with higher drug administration, certain drawbacks should be considered when treatment protocol is decided such as drug resistance, side effects of chemotherapy, and magnitude of the treatment effectiveness. In Chapter 4, we look into the effect that a drug has on tumours in significantly more detail.

2.5.3 Effect of Initial Tumour Size on Tumour Growth

The next result we use our model for is to find is the importance of the initial tumour size on the cell population. We have a default tumour size of 3000 cells for OVCAR-3 spheroids and 6000 cells for SKOV-3 spheroids, consistent with those used in the *in vitro* experiments in Section 2.4. Comparisons are made between the dynamics observed in tumours initialised with 50%, 100%, and 150% of these default tumour sizes, with the temporal dynamics of the populations tracked. The difference in initial tumour size can provide an option for the model to account for the stage in which the tumour is diagnosed and how advanced the tumour is in the area of interest.

OVCAR-3

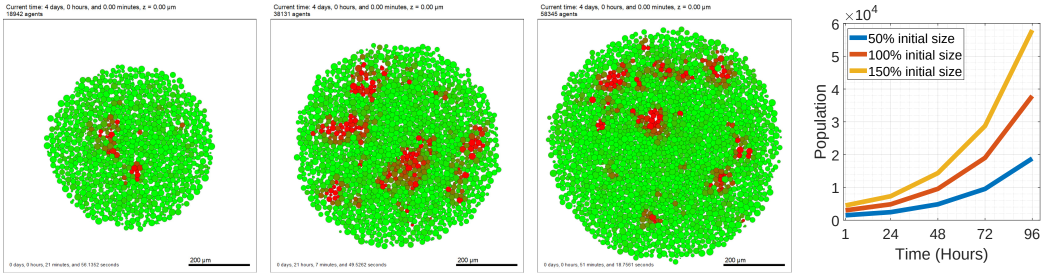

(A) 50% of the default initial tumour size.

(B) 100% of the default initial tumour size.

(C) 150% of the default initial tumour size.

(D) Population of cells for different initial tumour sizes over time.

FIGURE 2.18: **OVCAR-3 spheroids after 96 hours of simulated time for different initial tumour sizes.** Cross-sections of the OVCAR-3 tumours after 96 hours are shown for spheroids with 50% of the default initial population size (A), 100% of the default initial population size (B), and 150% of the default initial population size (C). The temporal dynamics of these simulations show the live cell populations over time (D).

Figure 2.18 shows the tumour growth for a small, medium, and large initial tumour size. Other than their size, the overall appearance of the tumours and the presence of the small mesenchymal clumps in the sphere of green epithelial cells remains similar. The larger tumours lead to a slightly more restricted availability of media to each cell, reducing the rate of EMT. Simultaneously, the larger OVCAR-3 spheroids have lower oxygen levels towards the centre of the tumour, in turn increasing the rate of EMT. These two effects somewhat cancel out, keeping the proportions of mesenchymal and epithelial cells roughly constant across tumour sizes. The rate of growth is similar between the three simulations, with proportions between the sizes of tumours across the three simulations remaining similar over time.

SKOV-3

Similar to OVCAR-3 spheroids, SKOV-3 spheroids shown in Figure 2.19 appear comparable across the different initial tumour sizes other than overall cell populations. For all different values of initial cell population, a thin layer of green epithelial cells consistently forms on the tumour periphery alongside a red pool of mesenchymal cells in the interior after 96 hours of simulated time. The growth rates between the simulations are again similar, as seen in Figure 2.19 (D).

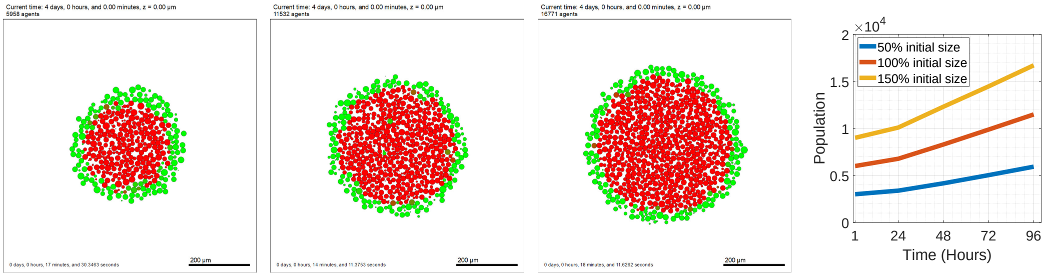

(A) 50% of the default initial tumour size.

(B) 100% of the default initial tumour size.

(C) 150% of the default initial tumour size.

(D) Population of cells for different initial tumour sizes over time.

FIGURE 2.19: **SKOV-3 spheroids after 96 hours of simulated time for different initial tumour sizes.** Cross-sections of the SKOV-3 tumours after 96 hours are shown for spheroids with 50% of the default initial population size (A), 100% of the default initial population size (B), and 150% of the default initial population size (C). The temporal dynamics of these simulations show the live cell populations over time (D).

2.6 Conclusions

The impact that adipose tissue has on cancer patients and their treatment is clearly shown to be crucial, with fat tissue encouraging EMT and cell proliferation in both epithelial and mesenchymal cells. The mechanisms responsible for this are still largely unknown but can be represented in mathematical equations used for the simulations to ensure the model is as representative of a natural cancer tumour as possible. We have shown previously that the model can recreate trends found in biological experiments with accurate results. This helps justify our ability to make predictions and gain answers to questions not yet found through *in vivo* or *in vitro* experiments. Unlike ODE models, the fact the model is agent-based with a set of rules for each cell phenotype makes the model extremely adaptable and replicable.

The capacity for this change allows relatively minor adaptations to be made to convert into models used for many other biological systems.

The key aim of the model in this chapter is to create an accurate and true model to represent the biological dynamics. A model which incorrectly quantifies associations between the cells will lead to results that over time become an unrealistic representation of the system and would give incorrect optimisation strategies. By performing relevant experiments, these interactions can be inferred from the results at different time steps and levels of adipose tissue. Analysing these experiments allows us to find the unknown parameters and create a model that fits as closely as possible to the data found. Ideally we would also obtain data on the various stromal cells such as fibroblasts and macrophages, as well as the concentrations of important substrates including oxygen, adiponectin, and leptin. A further key question is finding the key parameters involved in chemoresistance. Since these will be heavily time dependent it's crucial that their values over time are correct given the level of different stromal cells in the microenvironment, in particular adipocytes.

Areas of further interest include looking into the importance of the initialisation for the set up. Angiogenesis and metastasis are two of the areas in which cancer can transform into a more serious threat to human life. The ability of a tumour to provide itself with the necessary nutrients is a requirement for it to become a significant size. How this occurs and how adipose tissue can affect the angiogenesis of a tumour could be found and quantified in future variations of the model. Since few mathematical models have been created linking adipocytes with cancer, many of the interactions require new experimental data rather than by using past studies that could quantify the relationships. These interactions are likely to have a significant bearing on the outcomes of the models and simulations, hence it is important they are accurate to ensure the results are meaningful and useful for future research and treatment protocols.

The flexibility of the model and capacity to generate custom tumours and microenvironments helps us take further steps towards achieving patient specific treatment plans and digital twins. In doing so, a main objective would be to find the optimal treatment protocol for each patient, thus hopefully increasing the 5 year survival rate for ovarian cancer. In the future, the model could include additional agents such as fibroblasts and macrophages to ensure it is as close to any *in vivo* experiments as possible. Currently the adipose derived media is considered to be one single collective substrate. We know this is not the case as it includes various types of peptides and exosomes [93]. While a more complex model may lead to more representative results of tumours in patients, it is important to keep the model simple to avoid over complication and over fitting. For this reason, we create this model as a basis for future work and aim to explore increasing the complexity later in the study.

Chapter 3

Modelling the Epithelial to Mesenchymal Plasticity in Cancer

3.1 Introduction

EMT is a key process in which epithelial cells undergo phenotypic changes, enabling a reduction in cell-cell adhesion and enhancing the migratory abilities essential for normal tissue functionality within the body [222, 61, 125]. It allows the closure of developmental neural tubes [117], plays a key involvement in embryogenesis [151], and enables wound healing to occur [144]. Despite the reliance of the human body on this process, the role of EMT can occasionally become detrimental and further complicate treatment for diseases. EMT is heavily linked to cystic fibrosis by causing goblet cell and pneumocyte hyperplasia in the lungs [185]. Rheumatic diseases have also been linked to EMT, with rheumatoid joints expressing an abundance of TGF-β in the synovial fluid [250, 35].

Since EMT plays a large role in many different processes, it was recently suggested to separate EMT into three main types [113, 121]. EMT occurring during a self-contained process requiring multiple cell types to be generated such as organ development and embryo formation is classified as type 1. EMT associated with repair such as wound healing, organ fibrosis, and tissue regeneration is classified as type 2. This repair discontinues upon completion and when inflammation is reduced. The third type of EMT includes instances where there is a genetic and epigenetic difference between the epithelial and mesenchymal cell types. Type 3 is the key type of EMT associated with cancer progression and metastasis.

As mentioned in Chapter 2, EMT is no longer viewed as a binary switch and is now considered to be a more continuous procedure [83]. Cells can fluctuate through a multi-step process during which they may show partial epithelial and mesenchymal characteristics [165, 161]. This leads to a more complex differentiation process between classifications of cells. The ratio of the biological markers used in Chapter 2 (E-cadherin, N-cadherin, and vimentin) conclude the placement of these cells along the EMT scale [37].

EMT is a crucial step in cancer progression [190], allowing mesenchymal cells within a tumour to have lower cell-cell adhesion forces due to a reduced E-cadherin expression on the cell surface [201]. This allows the cells to break away from the main tumour location and escape from the brick-like structure they were previously a part of [31]. This relocation of cells can cause metastasis away from the primary tumour site, with metastatic cases responsible for over 90% of all cancer-related deaths [80]. One justification for this statistic is the improved drug resistance possessed by the slower cycling metastatic cells [56, 149]. These metastatic cells can obtain resistance to anoikis, a type of programmed cell death caused by a detachment from the surrounding extracellular matrix [163]. Cells can also switch from a phenotype tailored for proliferation to a phenotype which targets invasion around the body [48]. This lack of proliferation hinders the effectiveness of the drug, as targeting the rapidly dividing cells is no longer efficacious [148, 168]. This effect is responsible for lower long-term treatment dosages occasionally being beneficial. Higher dosages can eradicate the susceptible, less concerning epithelial cells, therefore making space and freeing up resources for the mesenchymal cells to exploit [226, 128, 77].

It has been shown that cells are also capable of undergoing mesenchymal-to-epithelial transition (MET) [106, 231]. This is the reverse process of EMT, where mesenchymal cells transition back to epithelial cells and regain the epithelial phenotype and behaviours previously exhibited [9, 221, 112]. The phenomenon of MET is primarily seen in mesenchymal cells which return to focusing on proliferation following their relocation elsewhere in the body [156]. While completing EMT allows a cell to travel with more ease throughout the body, MET enables transformation back to the faster proliferating, more stable epithelial phenotype [126, 182]. This allows the tumour to grow faster and spread throughout the body more rapidly [29, 247].

EMT has become an increasingly popular area for mathematical modelling, with many various approaches taken in the last decade. MacLean et al [139] uses an ODE model to measure the population sizes of two cell types: epithelial and mesenchymal. A reversible binary switch is assumed to occur between the cell types, with switch rates dependent on the total population sizes of each. Franssen et al [66] later models the metastatic spread of cancer using a non-binary classification of the EMT process. Partial EMT states are introduced and use an agent-based model with a system of ODEs within a 2D domain. The model allows cell detachment in partial EMT cells, with cells primarily around the tumour periphery undergoing transition to break away from the primary tumour. Other models such as those produced by He et al [89] and Mooney et al [150] include feedback loops of various transcription factors. Both the EMT and MET processes are modelled using systems of ODEs, with the correlations between the model output and various input parameters such as gene expressions studied. Murphy et al [153] develops both discrete and continuum mathematical models, inducing EMT and cell detachment through chemical signal concentrations. These concentrations also affect the proliferation rate and size of cells in the models. An extensive review performed by Jolly et al [107] has shown how past mathematical models have helped improve the understanding of EMT in cancer cells. The reverse process, MET, is included in the review to explore how the plasticity of the cells along this scale can impact the models and their findings.

Here, we investigate the role of EMT in the progression of ovarian cancer by developing a multiscale mathematical and computational model to investigate the role of EMT in OVCAR-3 and SKOV-3 cell lines. This model allows cells to migrate through the domain, proliferate at microenvironment-dependent rates, and progress through EMT in a biologically realistic manner. The model is based on experimental data and processes found in past literature with a focus on EMT rather than the adipose derived media.

The model will also be used to study the importance of including MET in tumour dynamics, a key process when modelling metastatic cancers. Direct comparisons will be made between simulations both including and excluding the presence of MET. Sensitivity analysis on the key parameters is performed to help quantify the role of EMT and its association with tumour size and composition over time. Following model validation using experimental data, future predictions are made on different initial states of the tumour. Temporal dynamics of tumours initialised with epithelial and mesenchymal cells across different cell lines are compared, with the importance of accurately distinguishing the cell lines of interest. By investigating the progression of cancer tumours in various scenarios, we aim to make predictions for how cell populations and tumour compositions are likely to change with time. Given these results, future adaptations of this model may be used to incorporate various treatment plans, potentially providing insights into the optimal treatment protocols. Ideally, patients diagnosed at a certain stage could have their tumour recreated as a digital twin and simulated using this model, incorporating this treatment method to provide the best prognosis possible.

3.2 Methods

Here, we study temporal tumour evolution over 96 hours using an adapted mathematical model. As done previously, OVCAR-3 and SKOV-3 epithelial cells are placed in the domain, with the cross-sections of the tumour shown each day until the completion of day four. The simulation results are then compared to the biological observations and data obtained from the *in vitro* experiments discussed in Section 2.2.

This chapter focuses on the role of the EMT process in general, rather than adipocyte driven EMT. This includes investigating the impacts of initial tumour compositions, or the inclusion of the reverse process, MET. Therefore, we remove media from the substrates and simply assume the effects are present in the background. In addition, we now assume there is an oxygen decay rate of 10 units per minute in the domain, causing low oxygen levels which could potentially lead to hypoxia induced EMT. The updated substrate related parameters can be found in Table 3.1.

Parameter	**Units**	**Oxygen**	**Signal**
Diffusion Coefficient	micron^2/min	1e5	0
Decay Rate	1/min	10	1
Dirichlet Boundary Conditions	dimensionless	38	0

TABLE 3.1: **Substrate parameter values with hypoxia.** Parameter values are carried across from those used in Chapter 2, other than a decay rate for oxygen. Hypoxia induced EMT plays a significant role in the dynamics, hence the inclusion of this decay.

3.2.1 Cell Cycle

Cells in the model progress through the cell cycle at varying rates depending on the conditions within both the cell and the microenvironment [70]. In Chapter 2, correlations between intra and intercellular conditions were assumed to have a linear relation to the cell cycling rate. In this section, Hill functions are used for these correlations to create saturation effects as shown in Figure 3.1 using Equation 3.1,

$$y = \frac{(sat - base) \cdot x^p}{K_{50}^p + x^p} + base. \tag{3.1}$$

A Hill power of four is used throughout, allowing minor behavioural changes during perturbations of small dependent variable values, while still creating non-linear correlations overall. Here, y denotes the response to a variable x, *base* and *sat* are the values that the Hill function can take for $x = 0$ and as x tends to infinity respectively, p is the Hill power used to assign the steepness of the curve, and K_{50} is the half max, the value of x for which y is half way between the *base* and *sat* values. These Hill functions asymptotically approach their saturation value, meaning their exact saturation value is never reached.

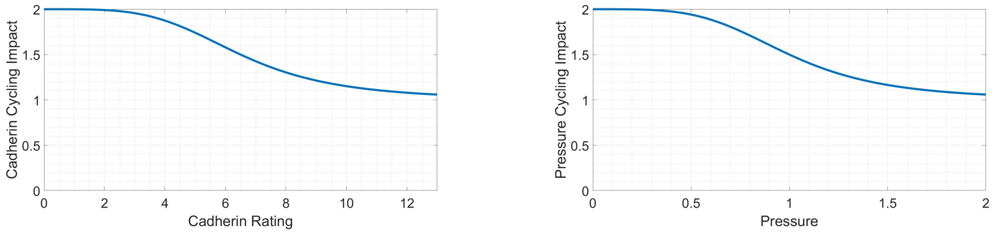

(A) Cadherin cycling impact parameter, c_c, vs cadherin rating. This shows the impact of the current cadherin rating on the rate at which a cell leaves G1. The more stable epithelial cells will cycle at a faster rate than the mesenchymal cells in the model.

(B) Pressure cycling impact parameter, p_c, vs pressure a cell is under. This shows the impact of contact inhibition in the model. Cells under higher pressure from their neighbours will leave G1 at a slower rate.

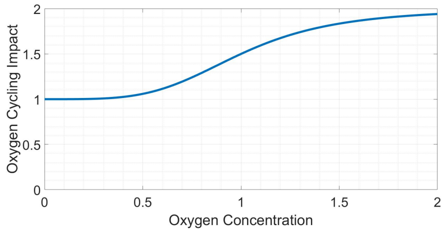

(C) Oxygen cycling impact parameter, o_c, vs oxygen concentration in the microenvironment. This shows the impact of hypoxia on the cell, with cells in higher oxygen levels leaving G1 at a faster rate through increased ATP production [15].

FIGURE 3.1: **Dependence of cell cycling parameter values on cell conditions.** Increased cadherin rating (A) and pressure a cell is under from neighbouring cells (B) decrease the cell cycling rate, while increased oxygen concentration (C) increases the cell cycling rate. Hill functions range between a maximum of two to a minimum of one.

Similar to oxygen concentrations, contact inhibition has been found to lead to arrest in the G1 phase of the cell cycle [235]. Therefore, similar to in Chapter 2, dependence of the conditions on the cell cycling rate is incorporated into the G1 cycling phase.

Cells with a higher cadherin rating are assumed to have more mesenchymal phenotypic behaviours and so cycle slower than those possessing more epithelial characteristics [78], implemented into the model as shown in Figure 3.1 (A). This parameter is two for entirely epithelial cells, asymptotically approaching one for entirely mesenchymal cells. Cells under higher pressure due to combined repulsion forces from neighbouring cells also reduce the cell cycling rate, as shown in Figure 3.1 (B) [71, 146]. This encapsulates the effect of cells requiring empty space in the surrounding area to divide into [177]. We generate this pressure cycling impact parameter value using a similar Hill function to that seen in Figure 3.1 (A), where the parameter value is two where no pressure is applied to the cell and tends to one where the pressure is two units. The unit of pressure is defined using a dimensionless analog described in the documentation of PhysiCell [73]. With a greater concentration of oxygen available in the microenvironment, cells are able to increase adenosine triphosphate (ATP) production and therefore cycle faster [59, 248, 191, 202]. This is incorporated into the model in Figure 3.1 (C) by introducing an oxygen cycling impact parameter ranging from one in hypoxic conditions to two in oxygen-rich conditions.

Due to the difficulty in quantifying the exact minimum and maximum parameter values in these functions, we assume that each cycling impact parameter fluctuates between one and two, meaning each variable has the capability of doubling the rate to exit G1. This assumption allows us to make qualitative conclusions regarding how the tumour size may depend on the intra-cellular and inter-cellular conditions. The exact parameters used in the generation of these Hill functions are shown in Table 3.2.

Cycling Rate Related Parameters					
y	x	$base$	sat	K_{50}	p
Cadherin Cycling Impact (c_c)	Cadherin Rating	2	1	6.5	4
Oxygen Cycling Impact (o_c)	Oxygen Concentration	1	2	1	4
Pressure Cycling Impact (p_c)	Pressure	2	1	1	4

TABLE 3.2: **Hill function parameters used for the variables in the cycling rate equation.** The table shows how the cadherin rating, oxygen concentration, and pressure that a cell is under can influence the cycling rate of a cell. Hill functions are used to quantify the impact of these conditions on the cell cycling rate according to the parameters shown in the table.

These impact parameters are used to calculate the rate at which a cell leaves the G1 stage of the cell cycle using Equation 3.2, where r is the cycling rate, b_c is a base cycling rate parameter, n is the current population, and K is the carrying capacity,

$$r = b_c \cdot c_c \cdot p_c \cdot o_c \cdot \left(1 - \frac{n}{K}\right). \tag{3.2}$$

The carrying capacity is included, estimated to be 6500, to allow a maximum population similar to that observed in the experimental data where the growth rate of large tumours are reduced. Due to the cycling rate variability being enforced in the G1 stage of the cycle, there is a time delay in the effect of this rate and the tumour can reach populations higher than that specified in the carrying capacity of the logistic growth term. Assuming on average that cells have a base cycling rate parameter (b_c) of 1/11 hours^{-1} [158], these values allow a maximum cycling rate of 8/11 hours^{-1} to leave G1. Due to the other stages of the cell cycle unaffected by the conditions, the total length of the cell cycle would therefore vary between around 14 hours in the optimal conditions for cell proliferation and 24 hours in the poorest.

3.2.2 Cadherin Rating

The cadherin rating of a cell has a key influence on its phenotypic characteristics [105]. We use a number of Hill functions to build correlations between the current cadherin rating and the behaviour of a cell. Figure 3.2 shows the assumed quantitative trends between cadherin rating and different cell behaviours such as migration speed (A), signal secretion rate (B), and cell-cell adhesion strength (C). Hill functions are used to generate these correlations, with relevant values shown in Table 3.3. Mesenchymal cells have been found to possess enhanced migratory tendencies [192, 123] and lower adhesion strength than seen in epithelial cells [208, 124]. Here, the increased migration speed which is permitted for mesenchymal cells allows the cells to move with greater freedom through the domain and increase the probability of the cell leaving the tumour itself to reach the domain boundary. The decrease in adhesion strength allows the mesenchymal cells to break away from neighbouring cells and escape the tumour with greater ease.

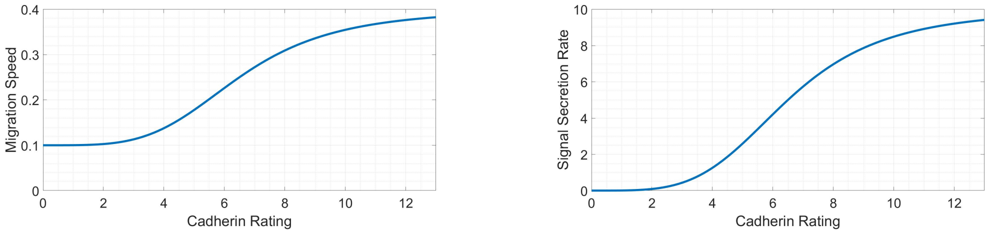

(A) Migration speed vs cadherin rating. This shows the speed at which cells can move throughout the domain as a result of random motion and any migration bias such as chemotaxis.

(B) Signal secretion vs cadherin rating. This shows the rate at which the chemical signal responsible for the bystander effect is secreted by the cells into their microenvironment.

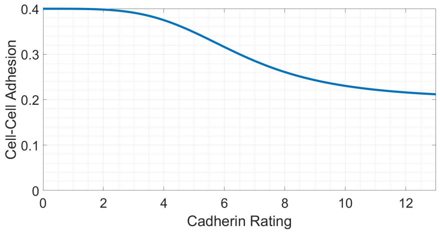

(C) Adhesion strength vs cadherin rating. This shows the magnitude of attraction between neighbouring cells, according to various adhesion interaction potential functions [138].

FIGURE 3.2: **Dependence of different cell variables on the current cadherin rating of the cell.** Increased cadherin ratings increase cell migration (A) and bystander signal secretion rate (B), while decreasing cell-cell adhesion strength (C).

Cell Behaviour Related Parameters					
y	x	*base*	*sat*	K_{50}	p
Migration Speed	Cadherin Rating	0.1	0.4	6.5	4
Signal Secretion Rate	Cadherin Rating	0	10	6.5	4
Cell-Cell Adhesion	Cadherin Rating	0.4	0.2	6.5	4

TABLE 3.3: **Hill function parameters used for the phenotypic behaviours.** The table shows how the cadherin rating can influence the behaviours of a cell in the model. Hill functions are used to correlate the rating to the migration speed, signal secretion rate, and cell-cell adhesion strengths.

Impact of Inter-Cellular Conditions

Following experimental observations, we hypothesise in our model that two main factors in the microenvironment contribute to EMT within epithelial cells. Hypoxic conditions have been found to encourage EMT in cancer cells by generating various signalling pathways and activating transforming growth factor TGF-β [102, 110].

This is achieved in the model using a Hill function to produce an oxygen EMT impact parameter decreasing from one in hypoxic conditions to approximately zero in oxygen-rich microenvironments, as shown in Figure 3.3 (A). It has also been observed experimentally that mesenchymal cells appear to promote EMT [44]. Here, we incorporate this using bystander signals, where cells higher on the cadherin rating scale secrete the chemical signal responsible for the bystander effect at increased rates. This leads to higher signal concentrations around the mesenchymal cells and a chain reaction of EMT to occur. Figure 3.3 (B) shows the quantitative impact that the signal concentration in the microenvironment has on the signal EMT impact parameter ranging between zero and one with a half max reached when the signal concentration is three units.

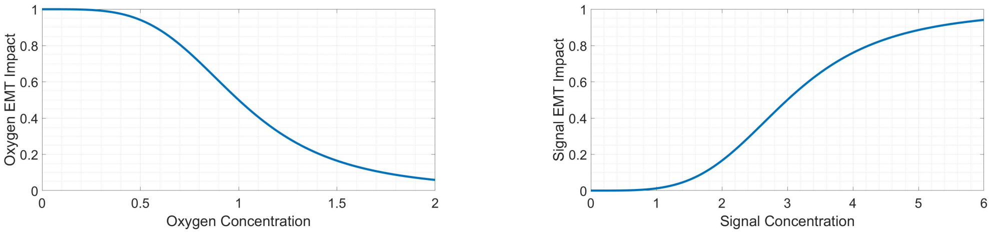

(A) Oxygen EMT impact parameter, o_e^*, vs oxygen concentration. This shows how hypoxic conditions affect the probability of a cell undergoing a step of EMT during an iteration of the simulation. Hypoxia encourages instability in epithelial cells and increases the probability of transition.

(B) Signal EMT impact parameter, s_e^*, vs signal concentration. This parameter accounts for the impact of the bystander effect on the EMT probability. Higher concentrations of signal in the microenvironment encourage epithelial cells to undergo EMT at a higher probability.

FIGURE 3.3: **Dependence of the EMT rate parameters on the microenvironment.** Increased oxygen concentration reduces the probability of EMT occurring in a cell (A) due to the lack of hypoxic conditions that encourage EMT. To create the bystander effect, an increased concentration of signal around a cell increases the rate of EMT (B). This ensures epithelial cells in the presence of signal secreting mesenchymal cells are more likely to undergo EMT and form mesenchymal clumps within the tumour.

These oxygen and signal EMT impact parameters are viewed as the unweighted probability that an EMT jump will occur as a result of oxygen and signal concentrations respectively. Therefore, the values range between zero (highly unlikely) to one (highly likely). A cell line dependent weighting for these terms is added later in this section.

Impact of Intra-Cellular Conditions

Cells are also given a cadherin EMT impact parameter, c_e^*, causing cells with a higher cadherin rating to progress faster through the EMT scale. Biologically, epithelial and mesenchymal cells are considered metastable, unlike hybrid cells which possess the highest plasticity, retaining proliferative potential while also being migratory and invasive [215, 108]. We introduce this phenomenon into the model using a Hill function based on the current rating of a cell, as illustrated in Figure 3.4. The parameter ranges from zero for purely epithelial cells to near one for purely mesenchymal. We combine this variable with the oxygen EMT impact, o_e^*, and signal EMT impact, s_e^*. Equation 3.3 shown later describes how these variables are combined to generate an overall jump probability depending on the cell line. This ensures that each relevant inter-cellular and intra-cellular condition contributes to this probability in a synergistic way.

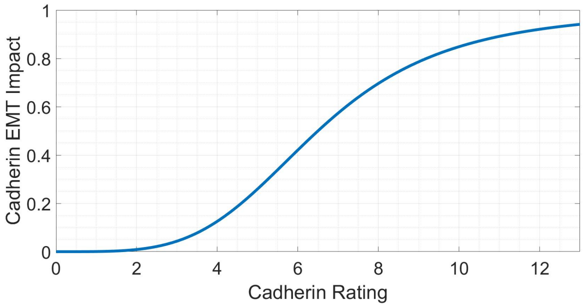

FIGURE 3.4: **Cadherin EMT impact parameter, c_e^*, vs current cadherin rating.** This shows how the current cadherin rating of a cell affects the likelihood of further steps up the cadherin rating. The positive correlation leads to increased stability in cadherin rating at either end of the EMT scale, as epithelial cells are less likely to undergo EMT on each iteration of the simulation than mesenchymal cells that are in otherwise identical conditions.

Similar to the inter-cellular variables in Figure 3.3, the cadherin EMT impact parameter is seen as the unweighted probability that an EMT jump will occur as a result of the current cadherin rating of the cell. The value is set to range between zero and one prior to the cell dependent weighting. Values used in the Hill functions are shown in Table 3.4.

EMT Probability Related Parameters					
y	x	*base*	*sat*	K_{50}	p
Cadherin EMT Impact (c_e^*)	Cadherin Rating	0	1	6.5	4
Oxygen EMT Impact (o_e^*)	Oxygen Concentration	1	0	1	4
Signal EMT Impact (s_e^*)	Signal Concentration	0	1	3	4

TABLE 3.4: **Hill function parameters used for the variables in the EMT probability equation.** The table shows how the cadherin rating, oxygen concentration, and signal concentration that a cell is in can influence the EMT probability of a cell. Hill functions are used to quantify the impact of these conditions on the cell EMT probability according to the parameters shown in the table.

Jump Probability

While EMT does appear more likely to occur in the G1 phase, cells are not limited to transitioning only during this stage of the cell cycle. EMT induced by TGF-β1 was found in cells synchronised at the G1/S phase but not in those synchronised at the G2/M phase [239]. However, despite increased blebbing during the M phase of cell division leading to a reduction of EMT-like phenotype, the transition can still be completed during mitosis [195]. We therefore, for simplicity, assume that the probability a cell undergoes EMT is independent of the stage of the cycle the cell is in.

We denote c_e^* as the cadherin EMT impact, o_e^* the oxygen EMT impact, and s_e^* the signal EMT impact on rates of EMT in cancer cells shown in Figures 3.3 and 3.4. A cell line specific weighting term is incorporated into these impact parameters, for which we assign an EMT impact factor parameter, α, to both cell lines. This parameter quantifies the tendency for the cells to undergo EMT on each iteration of the simulation, depending on the cell line. These inter-cellular and intra-cellular conditions give rise to a stochastic process by which the cadherin rating of the cell is determined.

OVCAR-3

Since EMT does not occur in the majority of OVCAR-3 cells during the previous experimental observations, OVCAR-3 is given a low EMT impact factor of one ($\alpha = 1$), as shown in Table 3.5. Larger values of α, such as that used in Table 3.6 for SKOV-3 cells, lead to larger weightings of the parameters when generating the jump probability term, p, in Equation 3.3. The influence of this α parameter is analysed later in the chapter. The cadherin EMT impact parameter has a low weighting for OVCAR-3 cells to ensure the number of clumps arising in the tumour throughout the 4-day simulation is not unrealistically high compared to biological observations (Figure 2.3). This low weighting is set to be 0.001, based on trial simulations. The impact of oxygen is set to be medium, as hypoxia is not seen as a requirement for EMT but does act as a key catalyst for the process [178, 58]. For simplicity, the weighting of the oxygen EMT impact is set to be 0.002, double that used for the cadherin EMT impact. The chemical signal impact responsible for the bystander effect has a large weighting to ensure disjoint clumps can be formed quickly despite the low diffusion of the signal. By observing simulations with different values of this weighting parameter, 0.01 is sufficiently high to allow clumps to appear within the time frame, while avoiding a chain reaction of EMT and mesenchymal cells taking over the tumour.

Parameter Name	**Unweighted Parameter Symbol**	**Parameter Weight** ($\alpha = 1$)	**Weighted Parameter Symbol**
Cadherin EMT Impact	c_e^*	0.001	$c_e = 0.001 \cdot c_e^*$
Oxygen EMT Impact	o_e^*	0.002	$o_e = 0.002 \cdot o_e^*$
Signal EMT Impact	s_e^*	0.01	$s_e = 0.01 \cdot s_e^*$

TABLE 3.5: **Values of the different variables used for the EMT probability in OVCAR-3 cells.** The signal EMT impact parameter has a large weighting to ensure sufficient levels of signal concentration can induce mesenchymal clump formation. The cadherin EMT impact parameter has a small weighting to ensure EMT does not occur too frequently within the tumour leading to a scenario in which the mesenchymal clumps begin to connect. OVCAR-3 has a low EMT impact factor to prevent excessive EMT from occurring throughout the simulation.

SKOV-3

Unlike OVCAR-3 tumours, in SKOV-3 spheroids the red mesenchymal clumps are no longer distinguishable and instead a large pool covering the entire center of the SKOV-3 tumour is formed, as shown in Figure 2.3 (B). To ensure sufficient amounts of EMT occur to encapsulate this effect, the jump probability weightings are increased by a factor of five to that implemented for OVCAR-3 cells, as shown in Table 3.6. The shell of epithelial cells around the exterior of the tumour, as seen in experiments, is implemented by including an oxygen-dependent condition on the SKOV-3 cells. Hypoxic conditions in SKOV-3 tumours have been shown to upregulate the chemokine receptor CCR7, in turn inducing EMT development [38]. When oxygen concentration increases above a threshold value (set to 2.8 units), it is assumed mesenchymal cells undergo instant MET and are assigned the cadherin rating value of zero. This occurs only around the exterior of the tumour where oxygen is sufficient enough to cross this threshold. Table 3.6 shows the weightings of each parameter involved in generating the EMT probability for SKOV-3 cells. These increased weightings compared to those used in Table 3.5 for OVCAR-3 cells lead to vastly increased amounts of EMT. The EMT impact factor parameter is given a value of five for SKOV-3 cells ($\alpha = 5$), meaning the parameter weights are five times larger in Table 3.6 than in Table 3.5. This value ensures sufficient EMT occurs throughout the SKOV-3 tumour to allow the pool of interior mesenchymal cells to develop inside the tumour. Figure 3.14 following sensitivity analysis performed later in the chapter will show how the final appearance of SKOV-3 tumours change according to the value of the α term. From testing simulations with different values of this term, we find that setting α equal to five completely removes epithelial cells from the tumour interior after four simulated days.

Parameter Name	**Unweighted Parameter Symbol**	**Parameter Weight** ($\alpha = 5$)	**Weighted Parameter Symbol**
Cadherin EMT Impact	c_e^*	0.005	$c_e = 0.005 \cdot c_e^*$
Oxygen EMT Impact	o_e^*	0.01	$o_e = 0.01 \cdot o_e^*$
Signal EMT Impact	s_e^*	0.05	$s_e = 0.05 \cdot s_e^*$

TABLE 3.6: **Values of the different variables used for the EMT probability in SKOV-3 cells.** All parameters have an increased weighting to those used for OVCAR-3 cells to ensure sufficient EMT can occur to generate the pool of mesenchymal cells within the tumour interior. The EMT factor is increased from one in OVCAR-3 cells to five in SKOV-3 cells, as shown in the table.

The newly weighted EMT impact parameters discussed above are incorporated into Equation 3.3 for OVCAR-3 and SKOV-3 cells, showing their cumulative effect,

$$p = 1 - (1 - c_e) \cdot (1 - o_e) \cdot (1 - s_e). \tag{3.3}$$

This jump probability, p, determines if a cell will increase its cadherin rating during each six-minute iteration of the computer simulation, leading to a slight increase in mesenchymal-like behaviours highlighted previously. Six minutes is chosen as the iteration length to ensure simulations remain relatively fast while keeping the timesteps as minimal as possible to increase simulation precision.

In Equation 3.3, c_e, o_e, s_e, denote the cell line specific, weighted cadherin EMT impact, oxygen EMT impact, and signal EMT impact parameters respectively. Since

EMT is a stochastic process, we take a probabilistic approach to determine how likely a cell is to jump up the cadherin rating on each iteration of the simulation. Each weighted parameter value in Tables 3.5 and 3.6 is viewed as the probability that an event occurs, the event in this case being the cell moving up the cadherin rating on an iteration as a result of the respective intra-cellular or inter-cellular condition. We assume for simplicity that each of these three variables assigned to each cell are independent of each other. The total probability that a cell jumps up the cadherin rating on an iteration is therefore the probability that any of these events occur, i.e., the probability of their union. This probability is given in Equation 3.3. When a parent cell divides, the cadherin rating in the model is conserved to the daughter cells.

3.3 Results and Discussions

To investigate EMT, cells are initiated with a cadherin rating of zero. It is assumed that only EMT can occur since we take the tumour to be in its primary location [178]. MET, the reverse process, primarily only occurs when the mesenchymal cells have relocated and stabilised in a new environment [94, 82]. This MET process will be discussed in more detail in Section 3.4.

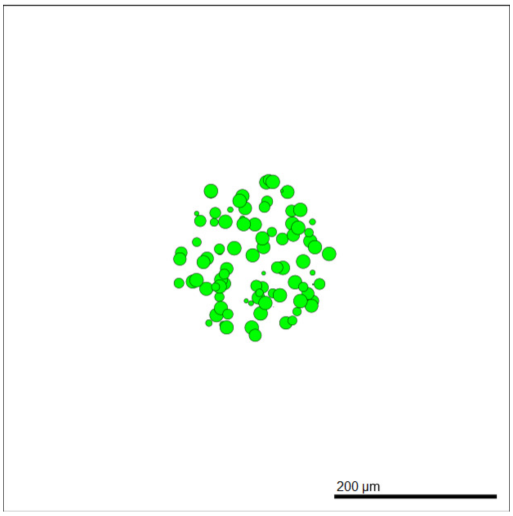

FIGURE 3.5: **Cross-section of an example tumour at time $t = 0$.** 1027 cells are randomly placed within a sphere of radius 120 microns around the center of the domain. Snapshots such as this show a $z = 0$ cross-section plane of the spheroid at the respective time of the simulation, with the colour of the cells showing the current cadherin rating ranging between green (epithelial) to red (mesenchymal).

An example of the initialisation is given in Figure 3.5. This depicts a cross-section of an OVCAR-3 tumour through the $z = 0$ plane at time $t = 0$ in which all cells are epithelial with a cadherin rating of zero. Here, we initialise the simulations with 1027 cells in a 3D spheroid scattered randomly within a sphere of radius 120 microns. This is to recreate the initial conditions as closely as possible to those used experimentally, in which repeats using spheroids with a mean of 1027 cells were placed. Both oxygen and bystander signal substrates are absent at initialisation. Oxygen has a constant influx into the system through Dirichlet boundary conditions applied on all boundaries of the domain set to 38 units, with *in vitro* tumours only capable of accessing oxygen through the tumour edges rather than any internal supplies such as vessels. The signal substrate is given Neumann boundary conditions with no constant influx. The model is simulated for 96 hours in which all cells are initialised with an equal cadherin rating, specified for each simulation.

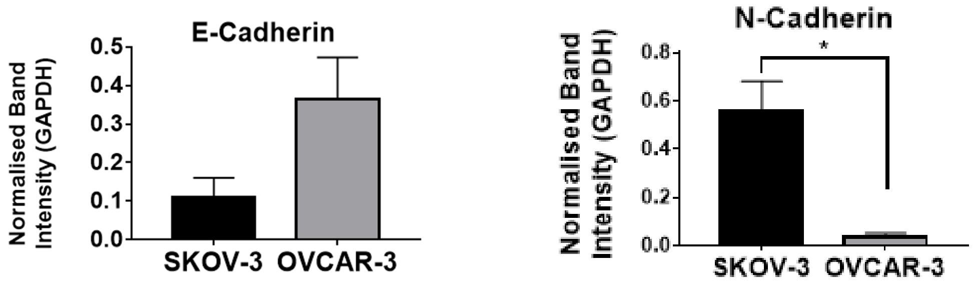

(A) Experimental E-cadherin band intensity.

(B) Experimental N-cadherin band intensity.

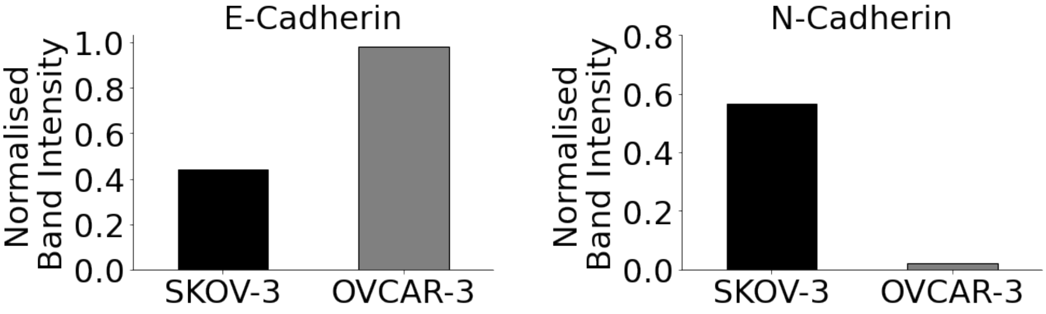

(C) Simulated E-cadherin band intensity.

(D) Simulated E-cadherin band intensity.

FIGURE 3.6: **Band intensity of E-cadherin and N-cadherin for the *in vitro* and *in silico* experiments**. Results after 96 hours from the *in vitro* biological experiments shows the normalised band intensities of E-cadherin (A), a marker for epithelial cells, and N-cadherin (B), a marker for mesenchymal cells. These are compared with *in silico* results taken after 96 hours of simulated time. Proportions of cells classified as epithelial (E-cadherin) and mesenchymal (N-cadherin) for both cell lines are recorded, shown in panels (C) and (D) respectively.

3.3.1 OVCAR-3

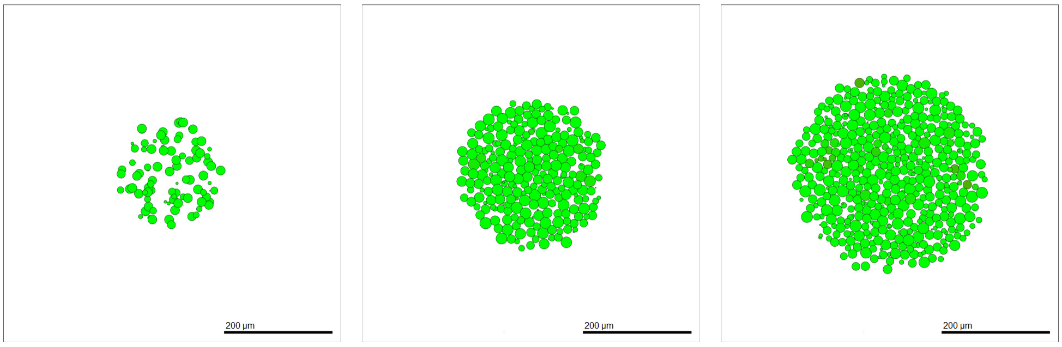

(A) 0 hours (B) 24 hours (C) 48 hours

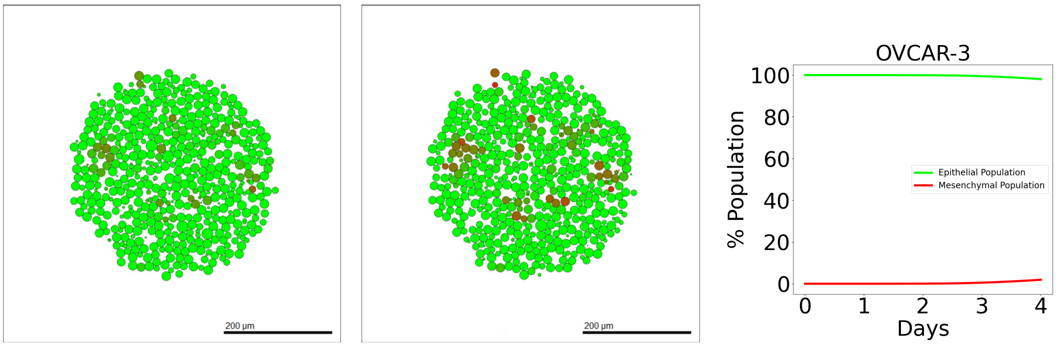

(D) 72 hours (E) 96 hours (F) Population types of OVCAR-3 cells over time.

FIGURE 3.7: **Simulated OVCAR-3 tumour at different time points using default parameter values.** The initial distribution of OVCAR-3 cells for the simulation is shown in panel (A). Cells after one day (B) and two days (C) show that initially very small amounts of EMT occur in the first 48 hours. Due to the bystander effect, clumps appear rapidly towards the latter simulation times, as shown after three days (D) and four days (E), in which small red mesenchymal clumps begin to form. Population types are shown in (F), with epithelial (green) and mesenchymal (red) tumour proportions over time with 95% confidence intervals.

Similar to the calibration performed in Chapter 2, Figure 3.6 shows the proportion of epithelial (E-cadherin) and mesenchymal (N-cadherin) cells in the final population of the tumour. Figures 3.6 (A) and (B) show the *in vitro* results while (C) and (D) show the results found *in silico* using the mathematical model. 95% Confidence interval bars are present in Figures 3.6 (C) and (D). However, due to the consistency across results from ten simulation repetitions, the intervals are too small to be visible in the bar charts. OVCAR-3 cells finish with a vast majority of epithelial cells in both the experimental and computer simulation results. SKOV-3 cells have a majority of mesenchymal cells, however, due to the outer shell being solely epithelial, SKOV-3 tumours have much higher proportions of epithelial cells than OVCAR-3 has mesenchymal. The simulation outputs are in qualitative agreement with the experimental results, with E-cadherin expression around three times higher in OVCAR-3 tumours than in SKOV-3 tumours. N-cadherin expression is negligible in OVCAR-3 tumours when compared to expressions in SKOV-3 tumours.

We now investigate how the simulated tumours change in both composition and size over time. Figure 3.7 shows simulated cross-sections of an OVCAR-3 tumour after 0 hours (A), 24 hours (B), 48 hours (C), 72 hours (D), and 96 hours (E). After one day (B) there is very little change in the tumour composition as cells remain almost purely green, suggesting no change in their cadherin ratings from zero. After two days (C) small, faintly mesenchymal clumps form on the left and right of the tumour. Upon completing day three (D), early stages of clump formation begin to appear and multiple patches of red mesenchymal cells show scattering throughout the tumour. After the final day (E), multiple clumps of mesenchymal cells have advanced throughout the cadherin rating and progressed rapidly through the stages of EMT, showing close agreement to the observation seen in Figure 2.3 (A).

We observe that despite the small red clumps, the majority of cells remain epithelial with a low cadherin rating. While the volume of these clumps appear negligible in comparison to the volume of the tumour, these clusters of mesenchymal cells cannot be overlooked. Upon breaking away, these cells can relocate and have a key responsibility in the metastasis of the tumour [204]. These clusters can perform collective migration throughout the body despite the lack of individual cell adhesion [220, 219]. The exact procedure by which this is carried out and made viable is relatively undocumented.

Moreover, each cell in the model has a pressure exerted on it by neighbouring cells, changing the cell cycling rate. We can compare the pressure each cell is under to its proximity to the centre of the tumour taken as the origin of the domain, shown in Figure 3.8 (A). Qualitatively speaking, there is a general negative correlation between the distance a cell is from the centre of the tumour and the pressure acting upon it. This is in agreement with the results found in the literature [207], allowing us to implement pressure-dependent behaviours to the cells in future model adaptations with confidence. Figure 3.8 (B) shows the oxygen levels throughout the tumour for each cell. Hypoxia is shown to be achieved in central areas of the tumour in which oxygen levels are lower than observed around the tumour exterior.

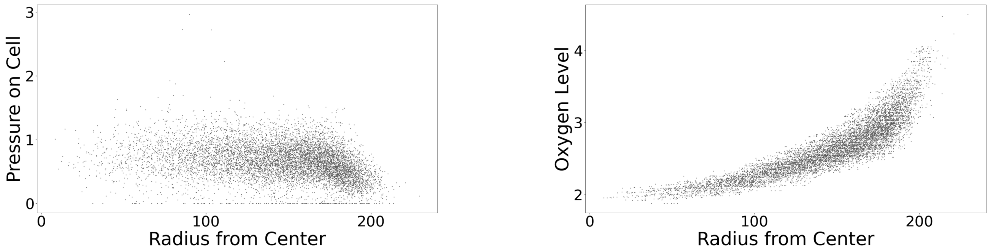

(A) Cell pressure compared to the distance from the centre of the tumour.

(B) Oxygen level compared to the distance from the centre of the tumour.

FIGURE 3.8: **Conditions of cells with respect to the position in the tumour.** Each black dot in the subfigures represent a cell at the final simulation time point. Panel (A) shows how the trends in the dimensionless pressure on the cells are affected by the distance of the cell from the center of the tumour. Using a trial simulation initialised with a tumour of OVCAR-3 cells, results show a general negative trend between the radius from the center of the tumour and the pressure on a cell. Pressure is generally lowest for cells at high radii, suggesting those on the tumour surface are under lower pressure from the neighbouring cells. Panel (B) shows a clear positive trend between surrounding oxygen levels for a cell and the radius of the cell from the center of the tumour, confirming those cells on the surface of the tumour have access to more oxygen than those in the interior.

3.3.2 SKOV-3

SKOV-3 tumour simulations give drastically contrasting results to that seen in OVCAR-3 spheroids, with cells progressing up the cadherin ratings at a much faster due to the increased jump probability. Figure 3.9 shows simulated cross-sections of a SKOV-3 tumour after 0 hours (A), 24 hours (B), 48 hours (C), 72 hours (D), and 96 hours (E). Large areas of the cross-section of the tumour begin to rapidly undergo EMT, creating a blend of epithelial and mesenchymal cells in the neoplasm as seen after one day (B). After 48 hours of simulated time (C), a clear majority of interior cells have fully undergone EMT and have a cadherin rating of around thirteen. Occasional green epithelial cells arise around the tumour periphery where oxygen has increased above the threshold value. After 72 and 96 hours in (D) and (E) respectively, the epithelial shell begins to form and creates a solid coating around the primarily mesenchymal tumour. The SKOV-3 tumours show a close agreement to experimental observations shown in Figure 2.3 (B). The outer shell of epithelial cells remains thin, with only mesenchymal cells making up the interior of the tumour.

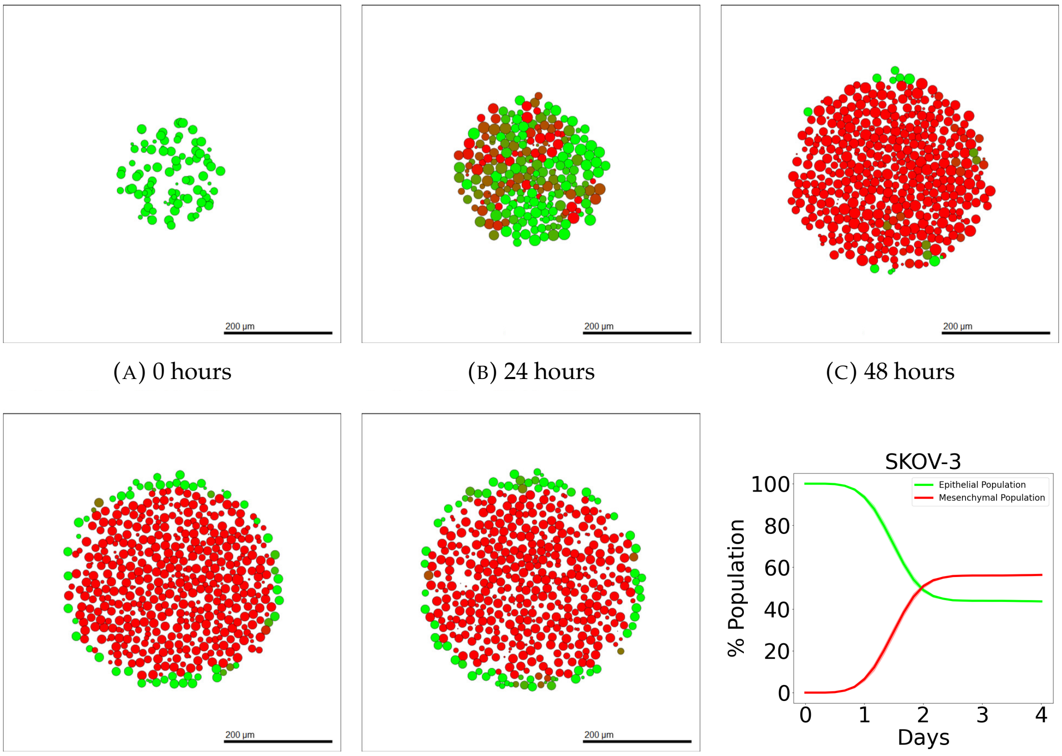

(A) 0 hours (B) 24 hours (C) 48 hours

(D) 72 hours (E) 96 hours (F) Population types of SKOV-3 cells over time.

FIGURE 3.9: **Simulated SKOV-3 tumour at different time points using default parameter values.** The initial placement of SKOV-3 cells for the simulation is shown in panel (A). After only one day (B), high levels of EMT has already occurred throughout the tumour, with completed EMT observed in almost all interior cells after two days (C). A red mesenchymal pool forms inside the tumour after three days (D) and four days (E) with a green epithelial layer created around the periphery. Population types are shown in (F), with epithelial (green) and mesenchymal (red) tumour proportions over time with 95% confidence intervals.

3.3.3 Sensitivity Analysis

Sensitivity analysis is a crucial part of any mathematical model, quantifying the sensitivity of each parameter on the output of a simulation. By changing the values of these input parameters, we can calculate the associated variation in the output. Multiple aspects of the output can be investigated, including information on the cell populations or the substrate concentrations. We use a form of Latin hypercube sampling (LHS) to perform global sensitivity analysis, along the Pearson Product Correlation Coefficient (PCC) value for different parameters to tell us which have the highest impact on the model output. We compare both how the size of the tumour and the composition of the tumour changes with fluctuations in the parameters used in Equations 3.2 and 3.3 for the two cell lines investigated. Generally, most parameters incorporated into these equations have a notable impact on at least one form of output. Parameters used in Equation 3.2 unsurprisingly tend to have more impact on the final simulated tumour size than the mesenchymal fraction for both OVCAR-3 and SKOV-3 tumours. This is due to changes in the cycling rate having a direct link to the proliferation observed during the simulation. Parameters used in Equation 3.3 have less impact on the final OVCAR-3 tumour populations but a much larger impact on the tumour composition. Increasing the parameters in Equation 3.3 increases the probability of cells undergoing EMT. This impact is more observable in OVCAR-3 tumours where the mesenchymal clumps can be formed throughout the tumour rather than only in the interior. SKOV-3 spheroids generally reach complete EMT in the tumour regardless of small changes in the parameter values used in Equation 3.3, as shown later in Figure 3.14. As a result, minor perturbations in the EMT impact weightings used for SKOV-3 have little impact on whether complete interior EMT is achieved.

By utilising an adaptation of LHS, global sensitivity analysis can be performed on the model [84]. Analysis is performed on six parameters: c_c (cadherin cycling impact), o_c (oxygen cycling impact), and p_c (pressure cycling impact) used to calculate the cell cycling rate in Equation 3.2, as well as c_e (cadherin EMT impact), o_e (oxygen EMT impact), and s_e (signal EMT impact) used to calculate the EMT jump probability in Equation 3.3. The values of each parameter is ranged by $\pm 20\%$ using 51 equally spaced values for each parameter. Each of these 51 values for each parameter is then assigned to one of the 51 simulations we run, resulting in a unique value for each parameter across the simulations. Two output variables from each simulation following 96 hours of simulated time are investigated:

- The total live cell population in the tumour.
- The fraction of the tumour considered to be mesenchymal.

Here, the classification of epithelial and mesenchymal cells is made according to if the cadherin rating is 0-6 (epithelial) or 7-13 (mesenchymal). This selection is due to the importance of these results in cancer diagnosis. The stage a patient is deemed to be at depends largely upon the size and metastatic ability of the tumour. These outputs are then compared with the input parameter values for each of the six parameters of interest, with the PCC value calculated to find the nature and magnitude of the correlation between the i^{th} input x_i and output y_i shown in Equation 3.4 [179]. The value of this PCC variable shows if the correlation between the input parameter and the simulation output is weak, moderate, or strong (See Table 3.7),

$$PCC = \frac{\sum_{i=1}^{51}\left((x_i - \bar{x})(y_i - \bar{y})\right)}{\sqrt{\sum_{i=1}^{51}(x_i - \bar{x})^2(y_i - \bar{y})^2}}. \tag{3.4}$$

Coefficient Magnitude	Strength of Correlation
0	No Correlation
Up to 0.4	Weak Correlation
0.4 up to 0.7	Moderate Correlation
Over 0.7	Strong Correlation
1	Perfect Correlation

TABLE 3.7: **Evaluations of different values for the *PCC*.** Positive/negative values suggest a likely positive/negative correlation [45]. Stronger correlations between the input and output result in higher magnitudes of the coefficient.

Total OVCAR-3 Population

Figure 3.10 shows the relationship between the key model parameters highlighted previously and the total population of OVCAR-3 cells after 96 hours of simulated time. The maximum cadherin cycling impact (A) has a strong influence and the maximum oxygen cycling impact (B) has a moderate influence on the final population size respectively. The maximum pressure cycling impact (C) is found to have a statistically weak influence on the final cell population, suggesting small variations in this value do not have a major impact on the population size in the tumour. The three parameters used in calculating the jump probability (Equation 3.3) all have a weak correlation to the total population of OVCAR-3 cells. This is to be expected since these parameters have no direct link to the cycling rate of the cell, instead only affecting the cadherin rating in the tumour.

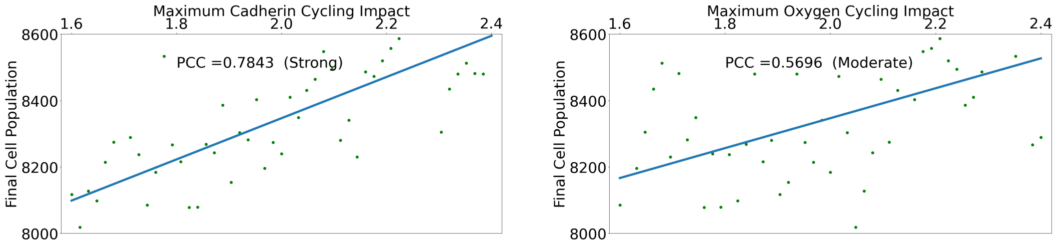

(A) Cadherin cycling impact parameter.

(B) Oxygen cycling impact parameter.

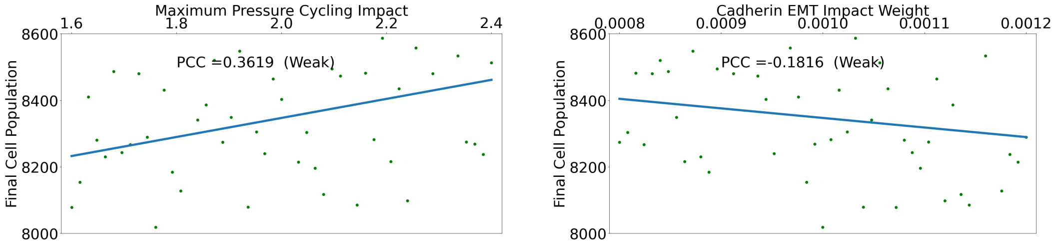

(C) Pressure cycling impact parameter.

(D) Cadherin EMT impact parameter.

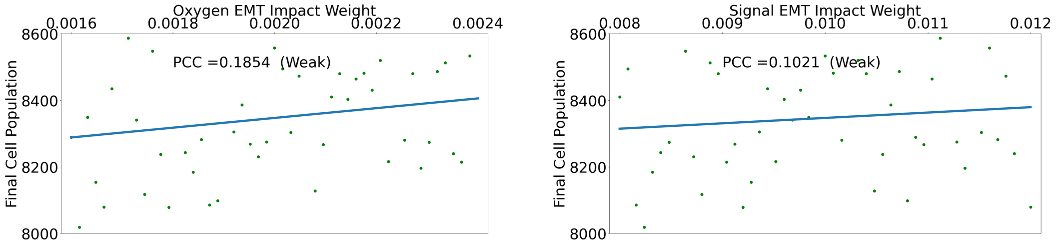

(E) Oxygen EMT impact parameter.

(F) Signal EMT impact parameter.

FIGURE 3.10: **The impact of parameter values on the total cell population in OVCAR-3 tumours.** The total tumour cell population after four days is found and compared for various parameter values. The *PCC* is given for each parameter across 51 simulations. Figures (A), (B), and (C) concern the cycling rate used in Equation 3.2, while Figures (D), (E), and (F) concern rates at which EMT can occur within the cells used in the jump probability in Equation 3.3.

Mesenchymal Fraction of OVCAR-3 Tumours

Figure 3.11 shows the relationship between the six parameters and the fraction of the total tumour population considered mesenchymal after 96 hours of simulated time. The oxygen EMT impact (E) and signal EMT impact (F) weights have a strong and moderate influence on the final composition of the OVCAR-3 tumours respectively. The cadherin EMT impact weight is the only weighting in Table 3.5 with a weak correlation to the final tumour composition. This is likely due to the small weighting that was assigned to the cadherin EMT impact used in Equation

3.3. All input parameters in Equation 3.2 have a negligible impact on tumour composition, suggesting there is a reasonable level of stability with respect to the user parameters involved in the cell cycling rate.

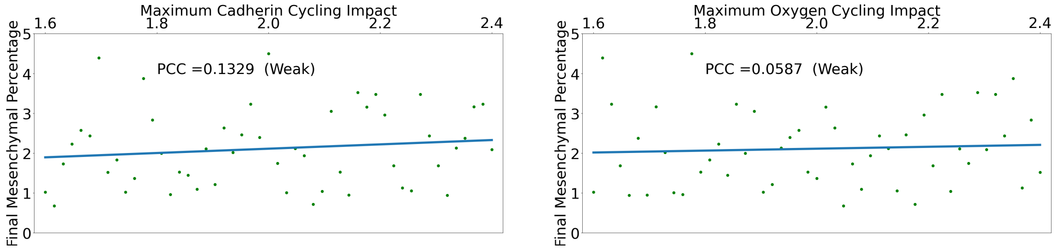

(A) Cadherin cycling impact parameter.

(B) Oxygen cycling impact parameter.

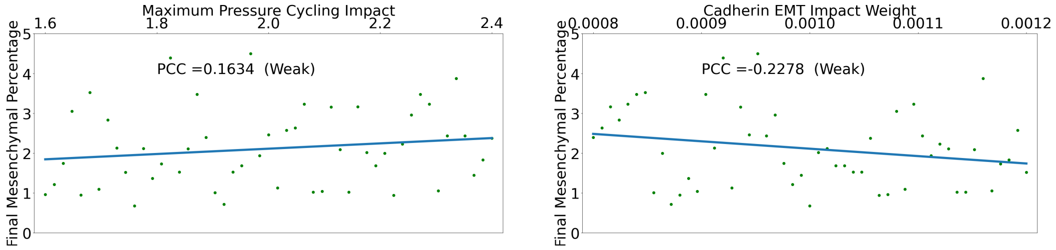

(C) Pressure cycling impact parameter.

(D) Cadherin EMT impact parameter.

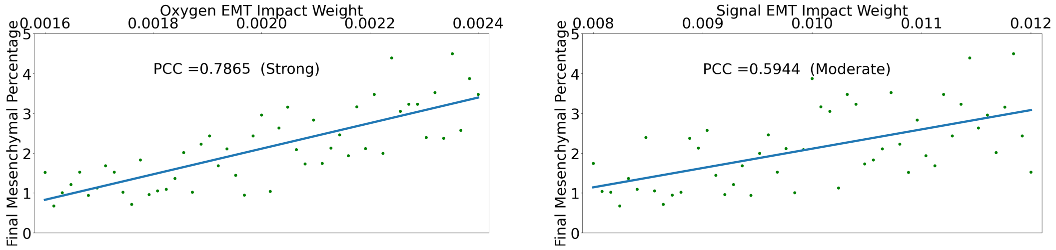

(E) Oxygen EMT impact parameter.

(F) EMT signal impact parameter.

FIGURE 3.11: **The impact of parameter values on the final composition of the OVCAR-3 tumour.** The fraction of the total tumour cell population classed as mesenchymal is found and compared for various parameter values. The *PCC* is given for each parameter across 51 simulations. Figures (A), (B), and (C) concern the cycling rate used in Equation 3.2, while Figures (D), (E), and (F) concern rates at which EMT can occur within the cells used in the jump probability in Equation 3.3.

The sensitivity of parameters on total populations and mesenchymal fractions show mostly opposite trends. Parameters showing strong correlations with total cell populations generally show weak correlations with the mesenchymal fraction and vice versa. This is due to the fact that these parameters either link directly to the cell cycling rate or the EMT probability, rather than both.

Total SKOV-3 Population

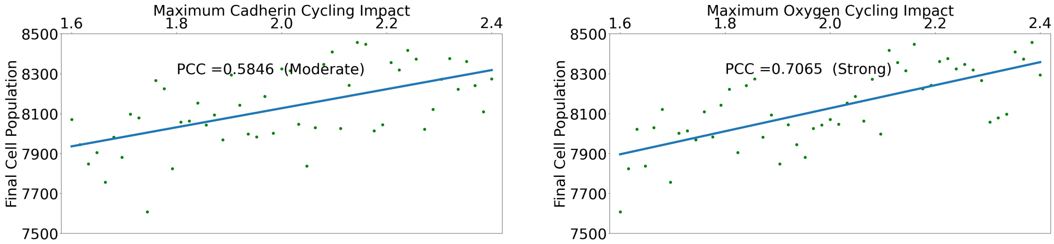

(A) Cadherin cycling impact parameter. (B) Oxygen cycling impact parameter.

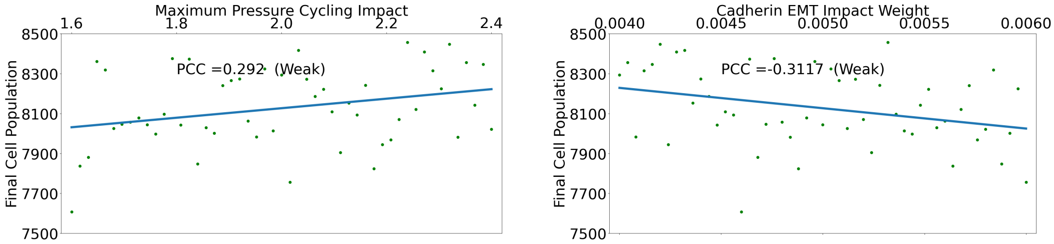

(C) Pressure cycling impact parameter. (D) Cadherin EMT impact parameter.

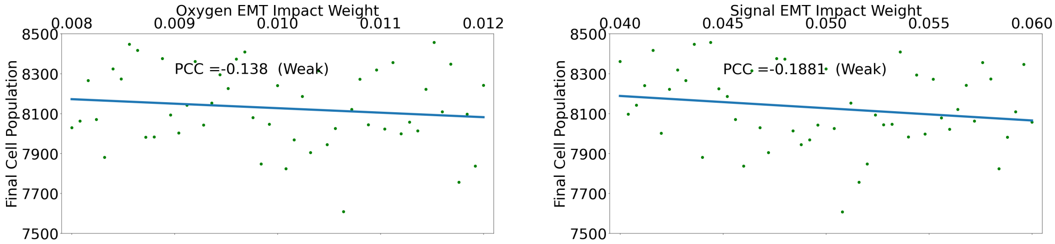

(E) Oxygen EMT impact parameter. (F) Signal EMT impact parameter.

FIGURE 3.12: **Impact of parameter values on the final total cell population in the SKOV-3 tumour.** The total tumour cell population after four days is found and compared for various parameter values. The *PCC* is given for each parameter across 51 simulations. Figures (A), (B), and (C) concern the cycling rate used in Equation 3.2, while Figures (D), (E), and (F) concern rates at which EMT can occur within the cells used in the jump probability in Equation 3.3.

Figure 3.12 shows the relationship between the same six parameters highlighted previously and the total population of SKOV-3 cells. The maximum cadherin cycling impact (A) and oxygen cycling impact (B) have a moderate and strong influence on the final population size respectively. Similar to OVCAR-3 tumours, the maximum pressure cycling impact has a weak correlation to the final population of SKOV-3 tumours, along with all the EMT impact weight parameters used in Equation 3.3.

Mesenchymal Fraction of SKOV-3 Tumours

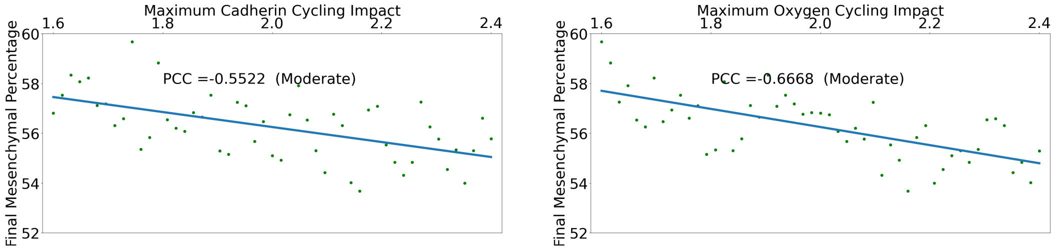

(A) Cadherin cycling impact parameter.

(B) Oxygen cycling impact parameter.

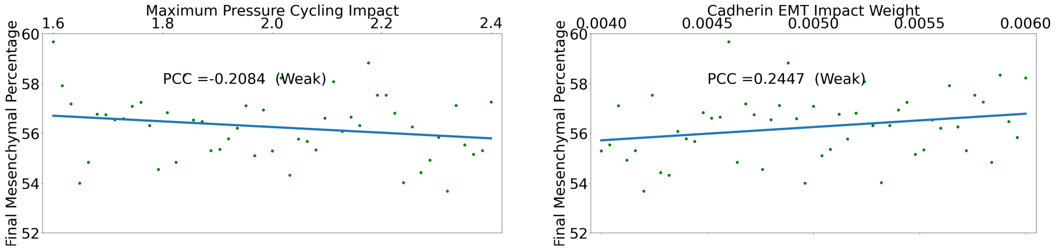

(C) Pressure cycling impact parameter.

(D) Cadherin EMT impact parameter.

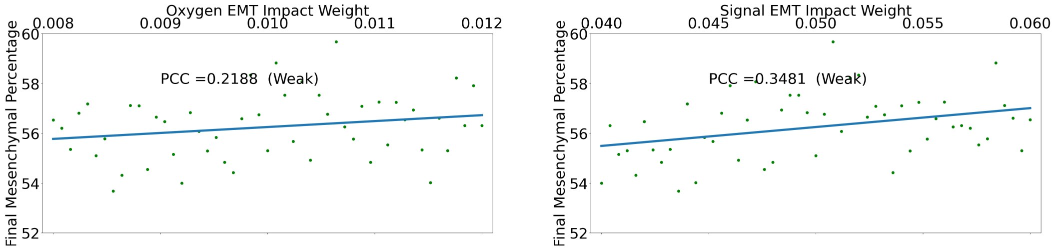

(E) Oxygen EMT impact parameter.

(F) EMT signal impact parameter.

FIGURE 3.13: **Impact of parameter values on the final composition of the SKOV-3 tumour.** The fraction of the total tumour cell population classed as mesenchymal is found and compared for various parameter values. The *PCC* is given for each parameter across 51 simulations. Figures (A), (B), and (C) concern the cycling rate used in Equation 3.2, while Figures (D), (E), and (F) concern rates at which EMT can occur within the cells used in the jump probability in Equation 3.3.

Figure 3.13 shows the relationship between the six tested parameters and the fraction of the SKOV-3 tumour population considered mesenchymal after 96 hours of simulated time. Surprisingly here, no EMT impact weight parameter has more than a weak impact on the percentage of mesenchymal cells in the final tumour, despite their direct link to the EMT jump probability (Equation 3.3). This is due to the fact that the interior SKOV-3 cells complete EMT and become mesenchymal regardless of small changes in these parameters. As well as this, the maximum cadherin cycling impact and oxygen cycling impact both have moderately negative correlations to the mesenchymal fraction of cells in the tumour. Increased cycling rates allow the tumour to grow faster, allowing the exterior cells to approach the domain boundaries. Here, the oxygen available to the cells is higher due to the Dirichlet boundary conditions imposed in the model, allowing a thicker shell of epithelial cells, thus decreasing the fraction of the tumour cells considered to be mesenchymal.

Cell Line Differentiation

Another approach to sensitivity analysis can be to change the difference in weighting terms between Tables 3.5 and 3.6. In these tables the weightings of parameters used in the EMT jump probability, p, in Equation 3.3 have five times larger weightings for SKOV-3 cells than OVCAR-3 cells. This creates the clearly distinguishable difference in tumour layouts, with OVCAR-3 possessing disjoint clumps of mesenchymal cells while SKOV-3 tumours have a pool of mesenchymal cells making up the entire interior. We define α to denote the factor at which SKOV-3 cells have a larger weighting than that used for OVCAR-3 cells in Table 3.5. For example, $\alpha = 5$ in Table 3.6. We can vary the value of α to explore at which point the tumour shows OVCAR-3 and SKOV-3 characteristics. Figure 3.14 shows the tumour appearance after 96 hours of simulated time for different values of α.

In Figure 3.14 (B) and (C) where $\alpha = 1.5$ and $\alpha = 2$, the tumour appears to show a hybrid state of OVCAR-3 and SKOV-3. Large clumps of mesenchymal cells are formed, with their increased size leading to eventual overlapping while making up a large proportion of the inside of the tumour. With values of α between two and four in Figures 3.14 (D), (E), and (F), the pool of mesenchymal cells has formed with only occasional epithelial cells appearing within the tumour interior. This appears closer to the original SKOV-3 tumour appearance. The slow transition between the cell lines across the figures display that the switch in the model between SKOV-3 and OVCAR-3 cells can be continual and non binary, generating cells with characteristics of both cell lines.

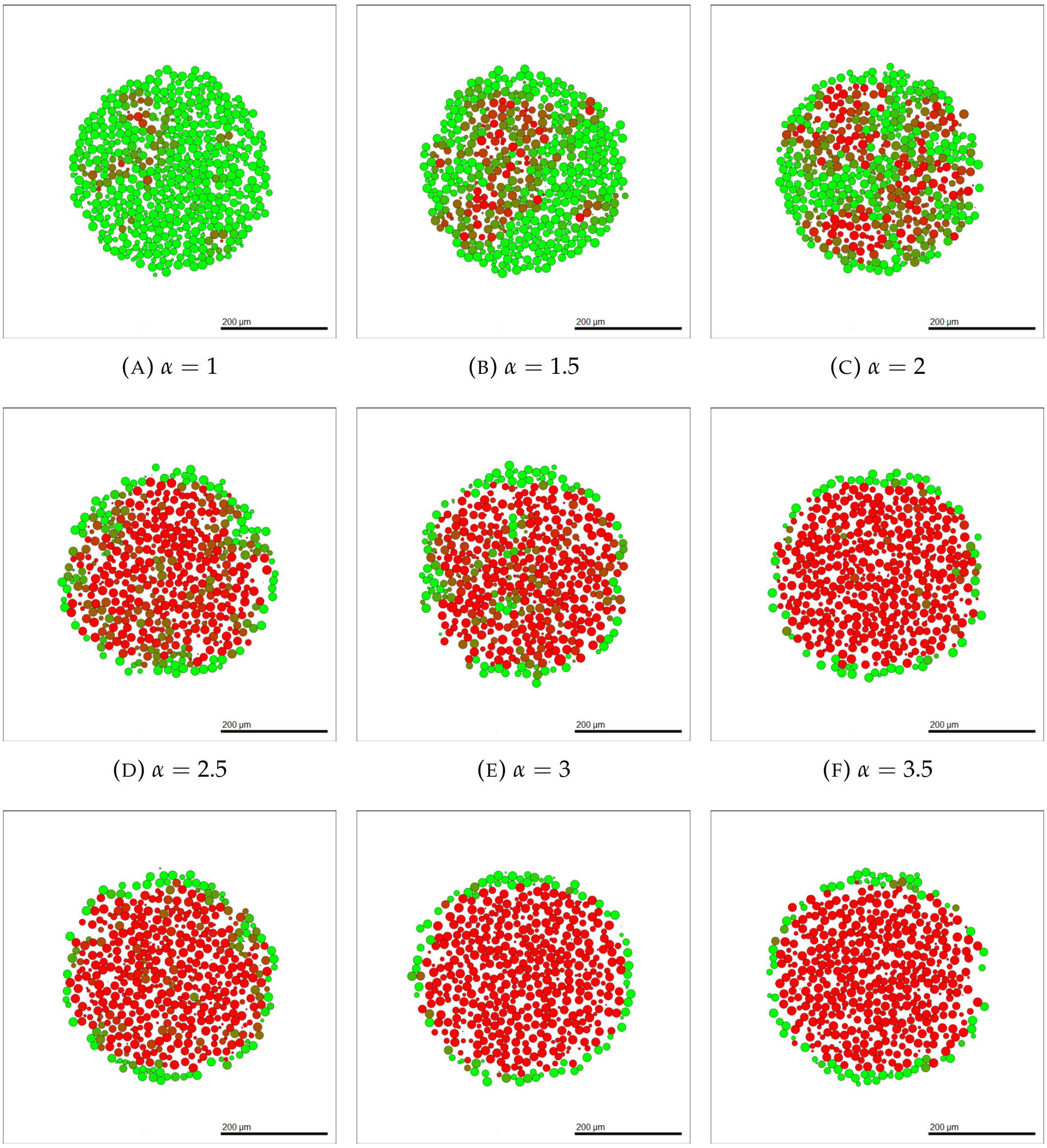

(A) $\alpha = 1$ (B) $\alpha = 1.5$ (C) $\alpha = 2$

(D) $\alpha = 2.5$ (E) $\alpha = 3$ (F) $\alpha = 3.5$

(G) $\alpha = 4$ (H) $\alpha = 4.5$ (I) $\alpha = 5$

FIGURE 3.14: **Impact of the value of α on the final composition of the SKOV-3 tumour.** Larger values of this α term lead to increased weightings for the parameters used in the EMT jump probability in Equation 3.3. Snapshots of the $z = 0$ plane are taken after four days of simulated time and compared for different α values.

3.4 Modelling Mesenchymal to Epithelial Transition

In this section, the effects of EMT and MET occurring simultaneously in tumours is explored. To model this, various intra-cellular and inter-cellular conditions are assumed to affect the rate of MET. Hyperoxic conditions have been found to increase the conversion of the EMT process into MET within cells [36]. Biological observations also suggest hybrid cells possess the highest cell plasticity on the epithelial-mesenchymal scale [215]. This suggests MET is more likely to occur in hybrid cells than the stable mesenchymal cells. To incorporate these dynamics, we denote two new variables, c_m^* defined as $1 - c_e^*$ and o_m^* defined as $1 - o_e^*$. These represent the contributions of higher oxygen levels and lower cell cadherin rating to an increased probability of MET on each iteration. In terms of probability, these can be seen as the compliments of c_e^* and o_e^* respectively. These parameters are shown in Table 3.8 and applied to Equation 3.5 to calculate the jump down probability on each iteration. For simplicity, we use the same "jump down" probabilities for the two cell lines, using similar values and weightings to those in Table 3.6 to account for the lack of signal impact involved in the EMT dynamics. Since no evidence was found in the literature of any bystander signal impacting MET rates, the concentration of the bystander signal was not incorporated into this equation.

Parameter Name	**Unweighted Parameter Symbol**	**Parameter Weight**	**Weighted Parameter Symbol**
Cadherin MET Impact	c_m^*	0.005	$c_m = 0.005 \cdot c_m^*$
Oxygen MET Impact	o_m^*	0.01	$o_m = 0.01 \cdot o_m^*$

TABLE 3.8: **Weightings for parameters used in generating the rates of MET for cells.** Only the current cadherin rating and the oxygen levels around the cell change the probability of a cell moving down the cadherin level on each iteration.

It has been observed experimentally that mesenchymal cells which have undergone EMT and have relocated to a secondary location may undergo MET at this new location [240]. This allows the cell to re-obtain the epithelial phenotype and behaviours previously exhibited to encourage stability and enhanced proliferative abilities [82]. MET has been observed in OVCAR-3 cell lines in which partial EMT has been completed [60]. SKOV-3 cells also show capabilities of showing molecular changes consistent with MET, transitioning from elongated to cuboidal shapes [96]. Here, we explore the effects of MET by including a probability in which cells can jump down in cadherin rating, q, shown in Equation 3.5,

$$q = 1 - (1 - c_m) \cdot (1 - o_m). \tag{3.5}$$

.

Cells continue to traverse through the cadherin ratings, jumping by only one step at a time. However, in this section, they are able to move either up or down during each iteration to allow for this MET process to be captured by the model.

To investigate the effects of heterogeneous cellular composition, a "hybrid" cell classification is now included into the model. Instead of only including epithelial and mesenchymal cells, the population is divided into three subgroups, giving us more precise results when tracking population types over time by providing extra categories for classification. Cells with a rating of four or less are now classified as epithelial, five to eight inclusive as hybrid cells, and nine or more as mesenchymal (See Figure 3.15). The tumour is initialised with each cell type separately to investigate the temporal impact of the starting tumour population type. This could ultimately provide an overview of how treatments for patients with tumours composed of varying cell types are likely to differ with time. Epithelial cells are initialised with a rating of zero, hybrid with a rating of seven, and mesenchymal with a rating of thirteen.

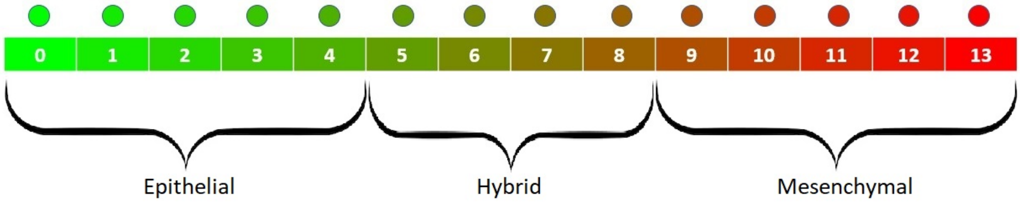

FIGURE 3.15: **Classification of cadherin ratings when hybrid cells are included in the model.** When including MET, a hybrid state is introduced into the classification of cells. Cells rated 0-4 are now classified as epithelial, 5-8 as hybrid, and 9-13 as mesenchymal. This ternary classification allows for more detailed results and easier comparisons with past models as shown in Sections 3.4.1 and 3.4.2.

3.4.1 OVCAR-3

Epithelial

OVCAR-3 tumours initialised with epithelial cells no longer obtain the defined isolated clumps of mesenchymal cells observed in Figure 3.7 during the simulation. Instead, the MET probabilities are too high to allow any notable amount of EMT to occur, as shown in Figure 3.16. The tumour size grows rapidly over time since the composition of the tumour remains mostly epithelial. Epithelial cells have the fastest cycling rate and so the tumour can proliferate at a faster rate than those initialised with hybrid or mesenchymal cells.

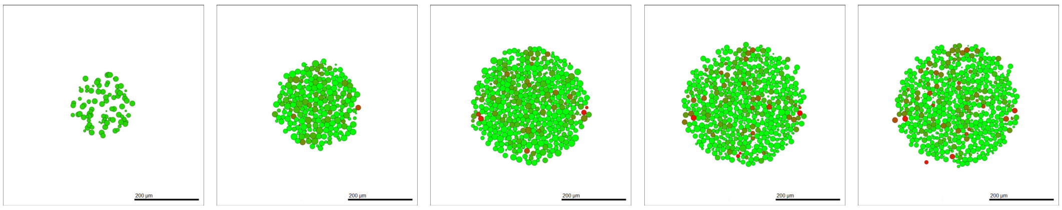

(A) 0 hours (B) 24 hours (C) 48 hours (D) 72 hours (E) 96 hours

FIGURE 3.16: **OVCAR-3 tumour over four days of simulated time, initialised with epithelial cells.** The initial placement of OVCAR-3 cells with an cadherin rating of zero is shown in panel (A). Minimal EMT occurs in the first day (B), with only very faint areas of darker green cells appearing after two days (C), suggesting very little EMT has occurred at this point. The amount of EMT undergone after three days (D) and four days (E) remains negligible, with all cells remaining purely epithelial over time.

Due to the lack of mesenchymal cells, even after 96 hours of simulated time, the adhesion between cells in the tumour remains high. The cells remain densely packed and part of the main tumour rather than breaking away and losing contact with other cells. This suggests that metastasis would be unlikely to occur at this point since the tumour is one rigid structure.

Hybrid

OVCAR-3 tumours initialised with hybrid cells result in a complete mix of epithelial, hybrid, and mesenchymal cells. No ordering or formation of clumps is visible despite the bystander effect present, as shown in Figure 3.17. Population sizes of the cell types appear generally similar with no clear majority of epithelial, hybrid, and mesenchymal cells present.

The tumour initialised with hybrid cells shows very high plasticity after only 24 hours of simulated time, as seen in Figure 3.17 (B). Following one day of simulated time there is a large population of green and red cells at the extremities of the epithelial-mesenchymal scale. This is unlike other initial conditions in which immediate changes in the tumour appearance are not observed as clearly. This suggests that hybrid cells in the model have the lowest stability and can fluctuate between states more readily than the more stable epithelial or mesenchymal cell type. Hybrid states are common in ovarian cancer and allow cells to retain both epithelial and mesenchymal characteristics, contributing to metastasis by exhibiting continued proliferation while gaining motility and resistance to therapy [236].

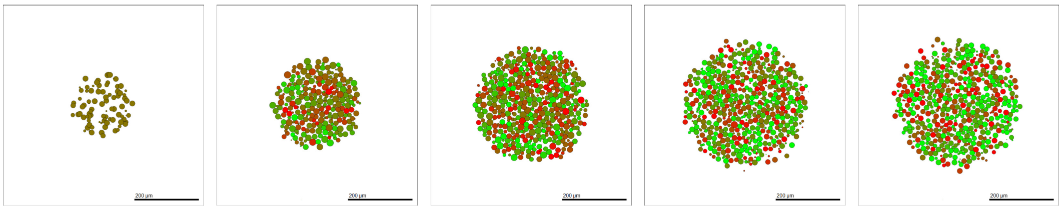

(A) 0 hours (B) 24 hours (C) 48 hours (D) 72 hours (E) 96 hours

FIGURE 3.17: **OVCAR-3 tumour over four days of simulated time, initialised with hybrid cells.** The initial placement of OVCAR-3 cells with an cadherin rating of seven is shown in panel (A). After one day (B), the tumour is made of a mixture of epithelial, hybrid, and mesenchymal cells, each scattered what appears to be at random throughout the tumour, with similar observations seen after two days (C). After three days (D), small collections of epithelial cells can be observed in among the scattering of individual epithelial, hybrid, and mesenchymal cells, seen further after four days (E).

Mesenchymal

When OVCAR-3 tumours are initialised with mesenchymal cells, the majority of the cells remain mesenchymal throughout the four day simulation. After the final simulation output, a scattering of epithelial cells is present throughout the tumour with no immediate observable patterning, as shown in Figure 3.18.

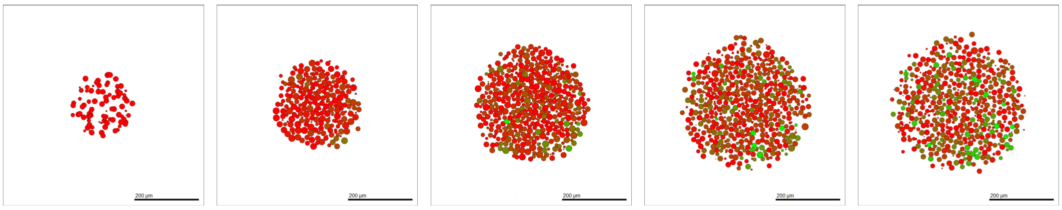

(A) 0 hours (B) 24 hours (C) 48 hours (D) 72 hours (E) 96 hours

FIGURE 3.18: **OVCAR-3 tumour over four days of simulated time, initialised with mesenchymal cells.** The initial placement of OVCAR-3 cells with an cadherin rating of thirteen is shown in panel (A). Minimal MET occurs in the first day (B), with areas of green epithelial cells appearing after two days (C). This patch of epithelial cells in the bottom right section of the tumour continues to grow after three days (D) with areas of epithelial cells observed throughout the tumour after four days (E), despite the vast majority of cells remaining mesenchymal during the simulation.

The OVCAR-3 tumour remains mostly mesenchymal over time, with a small number of epithelial cells appearing in the final tumour in Figure 3.18 (D) and (E). A number of cells can be seen escaping the main tumour clump and moving freely out into the domain. The tumour appears less grouped together with more empty space between the cells than seen in Figures 3.16 and 3.17. This is due to the high mesenchymal population decreasing the adhesion strengths within the tumour and the extra cell motility creating a less rigid tumour structure. This model resembles biologically the mesenchymal tumour cells with enhanced migratory capacity, favouring tumour cell dissemination over proliferation.

Temporal Dynamics

Here, we study the temporal evolution of cell populations to understand the dynamics and cellular transitions as shown in Figure 3.19. This is compared with experimental data in Figure 3.20 obtained by Ruscetti et al [187] for prostate cancers, obtained using the PKV cell line. The experiments by Ruscetti et al [187] shows the epithelial-mesenchymal plasticity in the PKV cell line cultured *in vitro*. Population fractions of each phenotype are tracked over the course of fourteen days, obtaining the temporal dynamics of the tumour. The PKV cells were isolated using fluorescence-activated cell sorting, identifying epithelial, hybrid, and mesenchymal-like cells during the *in vitro* experiment.

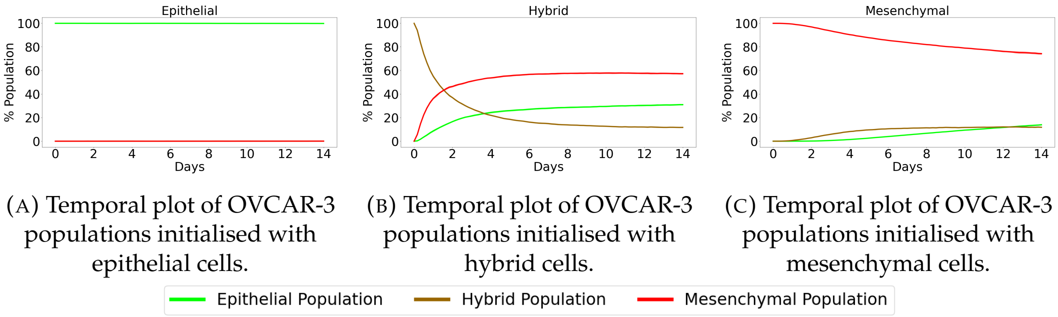

(A) Temporal plot of OVCAR-3 populations initialised with epithelial cells.

(B) Temporal plot of OVCAR-3 populations initialised with hybrid cells.

(C) Temporal plot of OVCAR-3 populations initialised with mesenchymal cells.

FIGURE 3.19: **Epithelial vs hybrid vs mesenchymal OVCAR-3 cell populations found *in silico* including MET.** OVCAR-3 tumours are initialised with epithelial (A), hybrid (B), or mesenchymal (C) cells. Simulations are run for fourteen days with the cellular proportions of the OVCAR-3 tumour composition recorded every hour. Curves show the populations of epithelial (green), hybrid (brown), and mesenchymal (red) cells during the simulation. Confidence intervals of 95% are present in each plot, taken from ten repeats of the simulation. However, due to the lack of substantial stochastically in the model, these intervals are not visible in the plots.

The comparisons between SKOV-3 and OVCAR-3 tumours in previous sections highlight the necessity for identifying potential differences in cell line characteristics. Despite this, different cell lines may still possess similar general trends and provide tentative insights into the predicted behaviour of others for model validation. The qualitative trends between the PKV cell line experimental results found *in vitro* by Ruscetti et al [187] and the OVCAR-3 cell line model results found here *in silico* are in close agreement. To remain consistent with the results found *in vitro*, we extend the time of the simulation from four days to fourteen. Simulations initialised with epithelial cells remain almost entirely epithelial throughout the simulation, with only small fluctuations in the cadherin rating of cells, as shown in Figure 3.19 (A). In Figure 3.19 (B), hybrid cells can go either way along the cadherin scale, with a notable population of epithelial, hybrid, and mesenchymal cells all present at the final time. Simulations initialised with mesenchymal cells remain mostly mesenchymal, with a small population of both epithelial and hybrid cells forming over time.

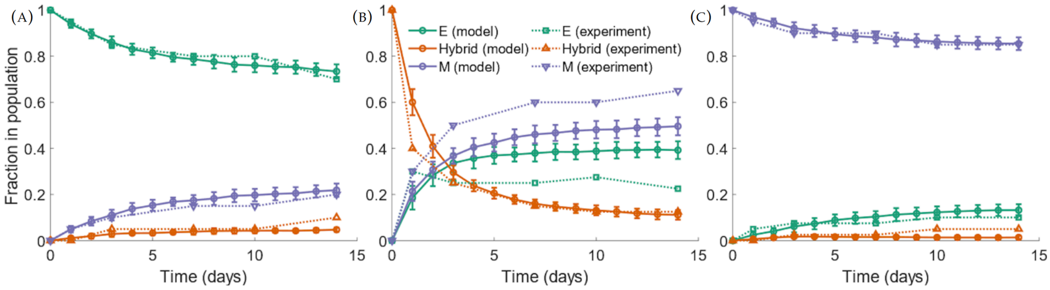

FIGURE 3.20: **Epithelial vs Hybrid vs Mesenchymal cells populations found by Tripathi et al [225].** Each panel shows the cell population of the cell types over time for both an *in vitro* experiment performed by Ruscetti et al [187] (dotted curves) and *in silico* simulation results of a model designed by Tripathi et al [225] (solid curves). Epithelial (E), hybrid, and mesenchymal (M) cell populations are shown using green, orange, and purple curves respectively. Cells initialised with either epithelial (A) or mesenchymal (C) cells generally remain with the respective cell type as the majority of the tumour at the final time of the simulation. Tumours initialised with a hybrid population (B) show lower stability, with cells rapidly transforming into either mesenchymal or epithelial cells.

Figures 3.19 and 3.20 confirms the importance of initial conditions on the tumour development, with (A) and (C) showing the stability in tumours initialised with epithelial or mesenchymal cells. While small changes occur in the tumour composition, the majority of cells in these scenarios remain the same type as those they were initialised with. Tumours initialised with hybrid cells (B) show increased plasticity and fluctuation in the cell types, with mesenchymal and epithelial cells both making up a large proportion of the overall tumour population.

3.4.2 SKOV-3

We can perform a similar experiment using SKOV-3 tumours. Since SKOV-3 cells are assumed to progress through EMT more rapidly than OVCAR-3 cells, the tumour progresses to the steady state of mesenchymal cells in the interior with a shell of epithelial cells around the exterior very rapidly. This leads to less dependence on the initial condition of the tumour cell type. Figure 3.21 shows the progression of the tumour over four days when initialised with epithelial cells. After 24 hours of the simulation, the majority of the cells become mesenchymal and have undergone EMT, as shown in Figure 3.21 (B). Few epithelial cells remain due to sufficient oxygen levels preventing EMT from occurring, with the vast majority of interior cells undergoing complete EMT within the first day. Midway through the simulation, as shown in Figure 3.21 (C), all cells other than those initiating the formation of the epithelial cells along the periphery undergo complete EMT. These interior cells remain mesenchymal for the remainder of the simulation.

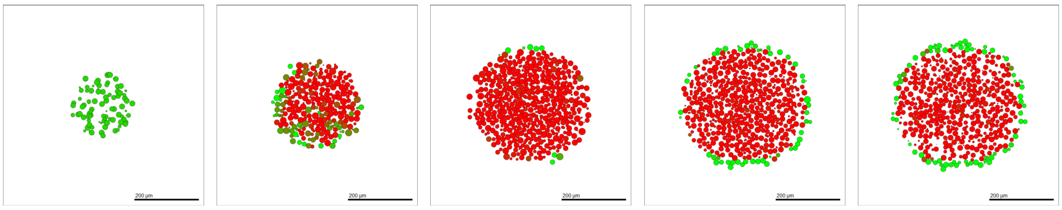

(A) 0 hours (B) 24 hours (C) 48 hours (D) 72 hours (E) 96 hours

FIGURE 3.21: **SKOV-3 tumour over four days of simulated time, initialised with epithelial cells.** Epithelial SKOV-3 cells are placed in the domain with an cadherin rating of zero (A). After one day (B), the majority of the tumour has undergone full EMT, showing a large area of red mesenchymal cells within the tumour. All interior cells complete EMT within two days (C), with occasional cells around the periphery converting back to epithelial cells as a result of high oxygen levels. This epithelial shell becomes more prominent after three days (D) and four days (E), where the outer layer of epithelial cells surround the interior pool of mesenchymal cells.

Figure 3.22 shows the populations of each cell type over time. In all initial conditions, mesenchymal cells rapidly become the main cell type in the SKOV-3 tumour. The epithelial cell population fraction gradually increases in Figures 3.22 (B) and (C). This is due to the tumour periphery expanding outwards and becoming more oxygenated due to the Dirichlet conditions from the domain boundary. This increased oxygen allows the threshold to be reached deeper into the tumour and the thickness of the epithelial shell to be increased. Cells mostly remain divided into either mesenchymal or epithelial, with very few hybrid cells appearing throughout the tumour. This agrees with the biological observations in the experiments shown in Figure 2.3 (B), where there is a clear division between the red pool of mesenchymal cells in the tumour core and green epithelial cells around the edge. Regardless of the initial conditions in the model, final population sizes for each type of SKOV-3 cell remain relatively consistent due to the fast rate at which EMT is reached compared to OVCAR-3 tumours.

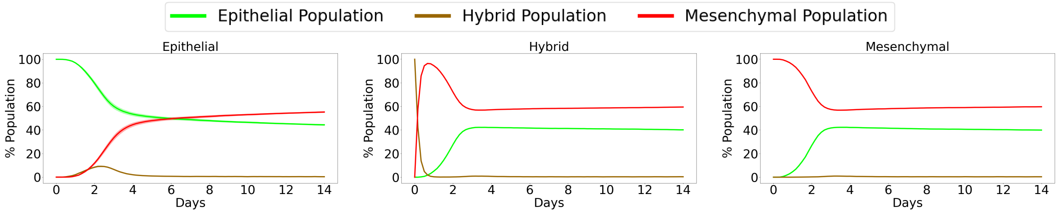

(A) Temporal plot of SKOV-3 populations initialised with epithelial cells.

(B) Temporal plot of SKOV-3 populations initialised with hybrid cells.

(C) Temporal plot of SKOV-3 populations initialised with mesenchymal cells.

FIGURE 3.22: **Epithelial vs hybrid vs mesenchymal SKOV-3 cell populations found *in silico* including MET.** SKOV-3 tumours are initialised with epithelial (A), hybrid (B), or mesenchymal (C) cells. Simulations are run for fourteen days with the cellular proportions of the SKOV-3 tumour composition recorded every hour. Curves show the populations of epithelial (green), hybrid (brown), and mesenchymal (red) cells during the simulation. Confidence intervals of 95% are present in each plot, taken from ten repeats of the simulation. However, due to the lack of substantial stochastically in the model, these intervals are not visible in the plots.

3.5 Conclusions

The role of EMT has been shown to have a key impact on OVCAR-3 and SKOV-3 tumours over time. While on the surface it may appear EMT is a binary process in which a switch is simply turned on, the complex dynamics in the background lead to a microenvironment-dependent, heterogeneous tumour layout. Few models created previously have investigated this continuous perspective of EMT with such a spatially dependent, heterogeneous approach. OVCAR-3 and SKOV-3 cells use similar rules in the mathematical model, with identical Hill functions used in the generation of parameters required for the EMT and cycling rates equations. By varying only the factor at which these parameters are larger in SKOV-3 cells than OVCAR-3 cells and incorporating an oxygen threshold in which SKOV-3 cells become epithelial, the biological observations seen *in vitro* can be accurately recreated. These changes are sufficient to induce the drastic differences seen between the cell lines experimentally.

The bystander effect is proven to generate results similar to those found experimentally. By using biological observations in Figure 3.20 for calibration, we can test our model against other data sets. The results show that the developed mathematical model can qualitatively predict the biological observations, indicating the usefulness of the model in exploring processes involved in EMT, MET and potentially to study responses to the therapy.

Sensitivity analysis on the model demonstrates that the outputs of interest are sensitive to most parameters involved in generating the rate at which a cell cycles (Equation 3.2) and undergoes EMT (Equation 3.3). SKOV-3 tumours have the unexpected behaviour of the mesenchymal fraction appearing independent of the parameter values used in Equation 3.3. Instead, the fraction is more dependent on the parameters used in the cell cycling rate in Equation 3.2. This is due to the fact that oxygen has Dirichlet conditions on the boundary edges, meaning cells able to get closer to the edges are in higher concentrations of oxygen. Higher cycling rates allow the tumour to expand and reach the boundary edges faster, allowing oxygen to reach further into the tumour surface and creating a thicker shell of epithelial cells around the tumour periphery.

The inclusion of MET in Section 3.4 highlights the importance of including all relevant processes on the cells studied. Including MET restricts the ability of the chemical signal to create mesenchymal clumps in OVCAR-3 tumours via the bystander effect. The tumours without MET ability are more representative of pre-metastatic tumours rather than those which have relocated into a secondary location. The detachable mesenchymal clumps and lack of clear overall structure to the tumour generally make OVCAR-3 tumours more harmful than SKOV-3 tumours. When including the process of MET alongside EMT, major differences in the final tumour layouts appear. The clumps seen in OVCAR-3 tumours are less apparent in the neoplasm, while SKOV-3 tumours remain possessing a similar green epithelial shell around the pool of central red mesenchymal cells. By changing initial conditions, we can see the importance of how we set the tumour composition used when starting a simulation. The bystander effect induces a chain reaction, encouraging cells in the proximity of surrounding mesenchymal cells to undergo EMT at an increased rate and become mesenchymal themselves. In SKOV-3 tumours the jump probability is large enough to reach stability within four days as EMT can be achieved in a shorter period of time than in OVCAR-3 tumours. This stability is seen in biological observations in which the interior of the tumour completes EMT and is made exclusively of mesenchymal cells, while the exterior cells remain epithelial with time upon reaching a certain proximity of the domain boundaries. These findings highlight the need for an accurate diagnosis when a patient is seen with ovarian cancer, in both the tumour size and composition.

The developed multiscale model shows a reasonable level of quantitative and qualitative agreement with experimental data [187] and previous model results [225]. Despite both different methods of fluorescence analysis performed between the varying cell lines, the general trends found between Ruscetti et al [187] and the mathematical model described above show similar qualitative results. While Ruscetti et al [187] uses a different cancer type (prostate) to that used for our model, this agreement allows us to have a certain level of confidence when extrapolating the model and parameter values beyond those in scenarios investigated experimentally. Doing this creates an opportunity to explore heterogeneous tumour variabilities such as a specific size, cell line, and mesenchymal composition. Including this heterogeneity can help make the tumour microenvironment more biologically realistic when treatment is then incorporated, making any gathered information more relevant to patients and improving the quality of care they receive.

Chapter 4

Quantitative Modelling of Tumour Responses to Treatment

4.1 Introduction

Behind only cardiovascular disease, cancer is the second largest cause of death in the United States [143]. The International Agency for Research on Cancer reported around 20 million cases of cancer in the year 2022 worldwide, leading to 9.7 million cancer related deaths [18]. Around one in five people are diagnosed with cancer during their lifetime, with the disease being attributed to the deaths of one in nine men and one in twelve women [18]. Due to late diagnosis and ineffective treatment methods, many cancer types such as pancreas (10%) and lung (7%) have very low 5-year survival rates [92, 17, 24]. As a result, an increased focus is being put on improving the prognosis of cancer treatment using a combination of methods including immunotherapy, chemotherapy, and radiotherapy [132]. Providing the optimal treatment protocol to patients is critical to ensure they have the best chances of survival while limiting the side effects associated with the therapies.

Cisplatin administration has become a popular method of ovarian cancer treatment and a crucial element of modern day medicine [237]. The drug has proven anti cancer properties caused by inhibiting DNA replication and inducing apoptosis through the formation of DNA adducts. These adducts cause helix instability and distortions in the DNA strands [224, 98]. The drug is administered intravenously and activates inside the cells by exchanging chloride ligands for water [249]. Cisplatin was FDA approved in the US for use against testicular and ovarian cancers in 1978, achieving approval the following year in Europe [74].

While cisplatin has evident positive effects on tumour size and aggression for patients, treatment may come with severe side effects. Renal toxicity is observed in 28-36% of patients treated with 50mg/m^2 of cisplatin as a single agent [74]. Neurotoxicity has been shown to be a side effect of cisplatin administration, with severe cases including patients suffering from a coma or status epilepticus [180]. Another crucial component of designing treatment protocol for patients is drug resistance. Tumours under repeated exposure to cisplatin can over time develop a larger proportion of resistant cells in its composition [142]. For this reason, finding a treatment plan for patients which provides optimal results while limiting the negative impacts associated with cisplatin is essential.

Using *in vivo* and *in vitro* experiments, tumour characteristics can be tested in a laboratory with different levels of treatment. These experiments require large amounts of time, money, and training to carry out. Mathematical models can present an alternative approach to testing the effects of drugs on a tumour without the need for these resources [14]. By developing a model to investigate the temporal and spatial dynamics of a neoplasm, simulations can be run and inferences can be made without these limitations. New treatment protocols can be tested *in silico* against cultured cell lines and provide results on the expected impacts.

When designing a drug treatment model, the developer has to consider the drug administration, mechanisms, diffusion, and degradation. Each of these aspects come with new questions and problems to address. For example, drugs administered *in vivo* are likely to be injected into the blood stream, entering the tumour microenvironment via diffusion from the blood vessels. If the tumour possesses a heterogeneous composition, resistant and susceptible cells can react differently to the treatment. The drug may also not diffuse equally throughout the tumour, causing the cells on the periphery of the tumour to be under higher exposure to the treatment. Certain cell types may be affected instantly by an increased concentration of drug in the microenvironment, while others may have a delay in the effects and initially remain unchanged. For each of these processes, a set of parameters is required to ensure quantitative accuracy in the outputs.

Many previous reviews have been performed on the types of mathematical models used to predict the impact of treatment on cancer tumours [243, 50, 53]. In a similar way, reviews have also been carried out on the possible approaches used to optimise parameter values based on experimental results [7, 228, 62]. These reviews tend to focus their attention on a certain type of model, such as ODE or agent-based models. Therefore, in this section, we aim to provide a broader overview of how drugs can be included into mathematical models regardless of the variety. Parameter optimisation approaches will be investigated, again with a broad range of techniques that are capable of optimising most types of model.

4.1.1 ODE Models for Drug Inclusion

ODE models track the rate of growth of tumour cells, usually dependent on current cell population sizes, substrate concentrations, and various drug related parameter values. Stein et al [210] used a model in which the rate of change of the tumour population, x, at time t is dependent on the natural growth rate, r, and a dose dependent drug effect, E, as shown in Equation 4.1,

$$\frac{dx}{dt} = r - E \cdot x. \tag{4.1}$$

The key chemotherapeutic parameter in Equation 4.1, E, relates to the effect of the drug on the growth rate of the tumour. The term is calculated using an E_i parameter found experimentally, quantifying the effect of the drug when administered at a dosage of $i$mg as shown in Equation 4.1a,

$$E = E_i \cdot p + N(0, \eta_i). \tag{4.1a}$$

A patient specific parameter, p, is also incorporated into the dynamics, dependent on variables such as the starting tumour size of the patient. To include stochasticity into the model, a normal distribution, $N(0, \eta_i)$, is included with mean zero and a dose dependent standard deviation of η_i, again calculated through fitting the ODE model to experimental data.

Instead of one homogeneous population, cancer tumours can be made of many different cell types. This tumour heterogeneity can give rise to a wide range of ODE compartment models, with the various cell types responding to treatment in different ways. Panetta et al [162] splits tumours into a population of proliferating cells, P, and quiescent cells, Q. The treatment is assumed to have no direct effect on the dynamics of the quiescent cell population, impacting only the cells actively proliferating. The total population of the tumour, x, is given in Equation 4.2. Here, r is the natural growth rate of proliferating cells, and E the dose dependent drug effect,

$$\frac{dx}{dt} = r \cdot P - E \cdot P. \tag{4.2}$$

The drug effect term, E, is dependent on the value of an effect parameter, d, and the concentration of the anticancer drug, $c(t)$, as shown in Equation 4.2a,

$$E = d \cdot c(t). \tag{4.2a}$$

Unlike the first model, this is a purely deterministic model with no stochasticity, with the effect of the drug directly proportional to the concentration. While the model includes no patient specific parameters, it does incorporate the composition of the tumour between proliferating and quiescent cells, with the drug only effective against the proliferating population.

A key limitation of both previous models is that the tumours are assumed to develop no drug resistance over time. This building up of resistance to chemotherapeutic drugs is a key aspect of cancer treatment and prognosis, with initial treatments often showing high success compared to administrations at later times. Claret et al [41] developed a tumour growth model that incorporated a time dependent resistance into the dynamics, shown in Equation 4.3,

$$\frac{dx}{dt} = r \cdot x - E \cdot e^{-\lambda t} \cdot x. \tag{4.3}$$

Similar to the previous models, r represents the tumour growth rate and E the initial drug effect term. To ensure the cell death caused by the drug reduces over time, an exponential decay term, $e^{-\lambda t}$, is included. This gradually diminishes the effects of the drug, reducing the kill rate and allowing the tumour population to recover, encapsulating the dynamics observed in patients more accurately.

Time dependency can be introduced into mathematical models of tumour growth in a number of ways. Ollier et al [160] develops an alternative model, in which rather than assuming the drug has an instantaneous effect on cancer cells, the model includes a damaged cell compartment. Sensitive cells can become damaged when exposed to chemotherapeutic drugs, with cell damage acting as an intermediate compartment between healthy cells and cell death. Populations are split into 3 groups: susceptible (S), resistant (R), and damaged (D). This leads to a rate of change in total tumour population, x, as shown in Equation 4.4,

$$\begin{cases} \frac{dS}{dt} = \alpha \cdot S \cdot \left(1 - \frac{y}{K}\right) - E \cdot S, \\ \frac{dR}{dt} = \alpha \cdot R \cdot \left(1 - \frac{y}{K}\right), \\ \frac{dD}{dt} = E \cdot S - \mu \cdot D, \\ \Downarrow \\ \frac{dx}{dt} = r \cdot (S + R) \cdot \left(1 - \frac{x}{K}\right) - \mu \cdot D. \end{cases} \tag{4.4}$$

As well as the inclusion of a logistic growth term with carrying capacity K, population dynamics of the tumour are also effected by the rate of death, μ, from the damaged cell population. A higher drug effect term leads to a higher rate of susceptible cells becoming damaged and capable of drug induced death. The effect of the drug in Equation 4.4 is similar to that used in Equation 4.2a, in which the effect is directly proportional to the concentration of drug.

The idea of damage accumulated by cells can take various directions. The model described in Equation 4.4 uses a binary approach in which cells either are or are not damaged. Other models take a more continuous approach to DNA damage, in which DNA damage undergoes a multistep process before completing programmed death. Simeoni et al [203] introduces a model with four compartments, one for healthy cells (x_1) and three for progressively more damaged cells (x_2, x_3, and x_4), with the total population denoted by x as shown in Figure 4.1 and Equation 4.5,

$$\begin{cases} \frac{dx_1}{dt} = f(x_1, x) - k_2 \cdot c(t) \cdot x_1 \\ \frac{dx_2}{dt} = k_2 \cdot c(t) \cdot x_1 - k_1 \cdot x_2 \\ \frac{dx_3}{dt} = k_1 \cdot x_2 - k_1 \cdot x_3 \\ \frac{dx_4}{dt} = k_1 \cdot x_3 - k_1 \cdot x_4 \\ \Downarrow \\ \frac{dx}{dt} = f(x_1, x) - k_1 \cdot x_4. \end{cases} \tag{4.5}$$

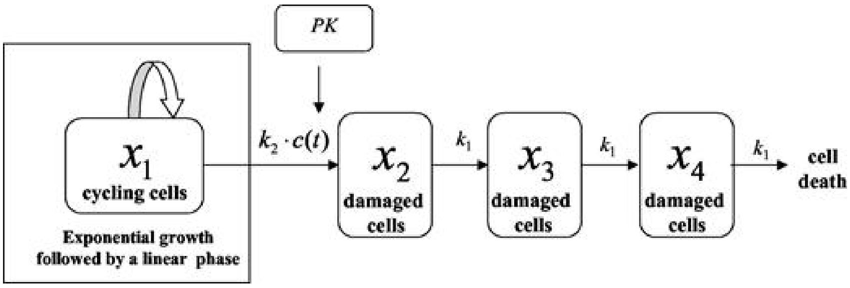

FIGURE 4.1: **Flow of cells through the compartments.** The image is taken from the paper by Simeoni et al [203]. Cycling cells in x_1 become damaged by the drug and enter x_2, initiating a chain reaction of damage until the cells die by exiting x_4. The rates at which cells move from damage compartments are assumed to be independent of the compartment the cell is in.

This approach allows the model to account for a delay in the impact of damage from the drug. The rate at which cells leave damaged compartments is assumed to be constant regardless of the stage of damage. A Hill-type function is included,

$f(x_1, x)$, in the growth rate of the x_1 compartment, explained in detail by Simeoni et al [203].

The models discussed so far all relate to a single drug type acting individually to reduce the tumour population. In many cases, however, a combination of drugs are administered to patients with the hopes of these drugs acting synergistically to reduce tumour growth more effectively than single dosage treatments. Bao [10] accounts for this by developing a mathematical model for a single drug and extending the model to capture the effects of two drugs used simultaneously. Similar to Equation 4.2, the population of sensitive cells in the tumour, y, is given by Equation 4.6 for a single drug treatment,

$$\frac{dy}{dt} = r \cdot y - E_1 \cdot y. \tag{4.6}$$

Here, E_i is the effect of drug i, found using a Hill function as shown in Equation 4.6a,

$$E_i = d \cdot \frac{c_i(t)}{k_i + c_i(t)}. \tag{4.6a}$$

The function incorporates a maximum death rate d, a half max concentration parameter k_i, and the drug concentration c_i.

This model is extended for when a second drug is introduced and administered simultaneously with another. The effects of the drug are assumed to combine additively, as shown in Equation 4.6b,

$$\frac{dy}{dt} = r \cdot y - (E_1 + E_2) \cdot y. \tag{4.6b}$$

This combined effect ensures the overall death rate caused by a chemotherapeutic treatment increases with the addition of another drug.

Population Dynamics	Drug Effect (E)	Equation	Model
$r - E \cdot x$	$E_i \cdot p + N(0, \eta_i)$	4.1	Stein et al [210]
$r \cdot P - E \cdot P$	$d \cdot c(t)$	4.2	Panetta et al [162]
$\frac{dx}{dt} = r \cdot x - E \cdot e^{-\lambda t} \cdot x$	$d \cdot c(t)$	4.3	Claret et al [41]
$r \cdot (S + R) \cdot \left(1 - \frac{x}{K}\right) - \mu \cdot D$	$d \cdot c(t)$	4.4	Ollier et al [160]
$f(x_1, x) - k_1 \cdot x_4$	$d \cdot c(t)$	4.5	Simeoni et al [203]
$r \cdot y - E_1 \cdot y$	$d \cdot \frac{c_i(t)}{k_i + c_i(t)}$	4.6	Bao [10]

TABLE 4.1: **Table of ODE approaches.** A summary of the ODE models developed previously to link the drug effect to tumour growth are provided above, with a wide range of different methods used in each.

A summary of the models discussed in this section is provided in Table 4.1, showing the population dynamics and drug effect for each model.

4.1.2 Agent-Based Models for Drug Inclusion

Alongside ODE models, agent-based models can provide an alternative, more stochastic approach to cancer treatment modelling. Agent-based models allow for a set of user defined rules to be assigned to the cancer cells, dependent on the conditions in the microenvironment, as performed in Chapters 2 and 3. Unlike ODE models, agent-based models provide each cell with individual dynamics depending on their situation, allowing for a more probabilistic approach to be taken.

Wang et al [230] developed an agent-based model to perform angiogenesis analysis on melanoma cells. The apoptosis rate of these cells were heavily dependent on the concentrations of the drug and glucose in the environment of the cell.

The probability of apoptosis for melanoma cells, p, during a time interval of Δt is given by Equation 4.7,

$$p = 1 - e^{-(\lambda_0 + \lambda_1)\Delta t}. \tag{4.7}$$

The natural death rate of melanoma cells is given by λ_0, and the death rate due to the cytotoxic drug is given by λ_1.

Here, w_1 and w_2 in Equation 4.7a are weighting factors given to the concentration of drug, C, and the concentration of glucose, G respectively,

$$\lambda_1 = \frac{w_1 C}{1 + w_2 G}. \tag{4.7a}$$

Unlike the ODE models, these concentrations of drug or glucose are assumed to be heterogenous throughout the spatial domain, leading to potentially varied rates of apoptosis from cell to cell.

Surendran et al [213] modelled the growth of glioblastomas, a type of brain cancer, using an agent-based approach. A treatment plan consisting of temozolomide administration was modelled using a PhysiCell framework [73] and simulated based upon a set of ODEs. The probability that a cell dies, p, on an iteration of length Δt is shown in Equation 4.8, using a Hill function with a Hill power of one,

$$p = r \cdot \left(\frac{C}{C + IC_{50}} \right). \tag{4.8}$$

Here, r is the natural proliferation rate, C is the concentration of temozolomide, and IC_{50} is the half effect drug concentration.

A similar model was produced by Hamis et al [85], where rather than assuming the drug directly increases the death rate of the cancer cells, here the drug is assumed to inhibit the repair of damaged cells. Cells in the G1 state of the cell cycle become damaged with a constant rate. Damaged cells can then either begin programmed cell death with probability p, or repair and return to being undamaged with probability $1 - p$. This probability is found using a Hill function as shown in Equation 4.9,

$$p = E \cdot \frac{C^\gamma}{EC_{50}^\gamma + C^\gamma}. \tag{4.9}$$

Here, E is the maximum effect of the drug, C is the concentration of drug in which the cell is located, EC_{50} the half max drug concentration, and γ the Hill power. Increasing the concentration of this drug decreases the value of p and encourages the death of the cell, rather than allowing the repair of a damaged cell that may behave abnormally.

In a similar probabilistic approach, Jalalimanesh et al [97] estimated the fraction of cancer that survive irradiation when administered at a certain dose. When treatment is administered, the agent-based model kills this fraction of the cancer cell population, calculated using Equation 4.10,

$$F = 1 - exp(-a \cdot C - b \cdot C^2). \tag{4.10}$$

Here, F denotes the fraction of cancer cells killed by a certain dosage of irradiation, C is the dosage administered to the patient, and a and b are factors obtained via parameter fitting. An algorithm is performed on each cell individually to ensure that approximately this fraction of the tumour is killed.

Table 4.2 provides a summary of the agent-based model approached discussed in this section [104]. Here, the death probability is provided for each model, showing how likely a cell is to die during an iteration of the simulation.

Death Probability (p)	Equation	Model
$1 - e^{-(\lambda_0+\lambda_1)\Delta t}$	4.7	Wang et al [230]
$r \cdot \left(\frac{C}{C+IC_{50}}\right)$	4.8	Surendran et al [213]
$E \cdot \frac{C^{\gamma}}{EC_{50}^{\gamma}+C^{\gamma}}$	4.9	Hamis et al [85]
$1 - exp(-a \cdot C - b \cdot C^2)$	4.10	Jalalimanesh et al [97]

TABLE 4.2: **Table of agent-based approaches.** A summary of the agent-based models previously developed that link the drug effect to tumour growth are provided above.

4.1.3 Parameter Optimisation Methods

The values of parameters which have not previously been found and documented in scientific literature require other methods to estimate. Parameter optimisation is a process in which the values of the unknown parameters in a mathematical model are found using one of a number of different approaches. To initiate parameter optimisation, data obtained from a *in vivo* or *in vitro* experiment is usually required. This data enables the user to quantify the difference between the *in silico* output and the experimental results, allowing this to be minimised and the relevant parameter values to be extracted. Due to the variety in types of *in silico* models and format of experimental results, there is no single standard approach to parameter optimisation. Optimisation techniques used for ODE models may not work for agent-based models, or vice versa for example.

Grid Search

Grid search is a common technique used to optimise parameters by running separate simulations for every possible combination of values in the parameter space. The results from each simulation is saved and compared to the data set that the user wishes to emulate with their model. The parameter set associated to the simulation with the smallest error to the data is extracted and assumed to be the optimal combination of parameter values for the model. This method is generally easy to initialise and is completely exhaustive of every parameter combination. However, it is usually only chosen as the method for parameter optimisation when the parameter space is small due to the high computational cost. If n parameters need optimising, each with m possible values, performing a grid search on the model would require n^m simulations.

Du et al [57] adopted a grid search approach to optimise the values of four parameters in their model. The model predicted the activity of epidermal growth factor receptor inhibitors, a class of drugs used for their anti-tumour properties. After grid search was completed, optimal parameter values were selected for the model using the best multi-linear regression from the simulations for the half effect drug concentration parameter value, pIC_{50}. Principal component analysis of the descriptors incorporated into this linear relation was performed, providing improved predictions to other linear regression models under consideration.

Grid search alongside matrix factorisation was performed by Wang et al [232] for various methods used to predict drug impact. Drug response matrices were scaled by dividing by the maximum absolute value in the matrix, ensuring all elements fell within the range [-1,1]. Regularisation parameters incorporated into the row vectors of these matrices were selected either from a uniform scale or a logarithmic scale via the grid search method across the parameter space. Three different methods of matrix factorisation used for the estimation of drug response were compared using the Pearson Product Correlation Coefficient (PCC) and root mean squared error (RMSE) analysis. For model validation, nine of the ten data sets were used as training, with the remaining set used to test, repeated ten times with a different testing set on each run. Taking a similarity regularised matrix factorisation approach was found to achieve the best results, leading to the highest PCC value and lowest $RMSE$ value.

Bayesian Optimisation

When determining parameter values, data obtained from the biological experiments may not be the only information a modeller wishes to base their optimisation on. Bayesian optimisation is a technique used to allow the incorporation of prior beliefs regarding the value of a parameter. Depending on the certainty of these prior beliefs, a weighting may be assigned to the likelihood distribution (generated from the data) and the prior distribution estimated by the modeller. These weights depend on aspects such as the certainty of the collected data and can generate a posterior distribution for the parameters from which optimised values can be extracted. Bayesian optimisation can take many different approaches depending on the form of the data available and the prior assumptions made by the modeller.

An agent-based model developed by Demetriades et al [51] quantified the impact of a cancer drug, with unknown parameters estimated using the Variational Bayesian Monte Carlo method. The rate at which cells divide and die were each assigned a prior Gaussian distribution with estimated respective means found by fitting to relevant *in vitro* values. Gaussian processes were then used to act as a statistical surrogate to estimate these posterior distributions, minimising the computational cost.

A key positive when using a Bayesian approach to model drug therapies is the inclusion of the prior distribution. Patient specificity is critical in obtaining optimal treatment protocols, suggesting that finding a way to incorporate a patient specific distribution for parameter values would be highly advantageous. Jayachandran et al [100] developed a model using Bayesian parameter optimisation that introduced a patient specific posterior distribution. Estimations of the relevant parameter values were used to generate a prior distribution based on a unique set of data provided by each patient, generating individual likelihood functions. Bayes theorem was then used to calculate the posterior parameter distributions and estimate the patient specific parameters.

Particle Swarm

While Bayesian optimisation incorporates prior beliefs with previously collected data, the more usual approach to parameter optimisation is to base parameter values on the data alone to reduce subjectivity. Particle swarm is a method used to optimise parameter values in a model by minimising a loss function. One or more initial estimations are made for the values of the model parameters. This set of predictions can be visualised as a set of particles placed within the parameter space. The value of the loss function is calculated for each particle in its current position, and a random velocity is assigned to each particle. Each particle then updates its position within the parameter space based on this assigned velocity. The loss function is again stored, a new velocity given to each particle, and the location updated. This is repeated up to a certain number of iterations at which point an optimal position in the parameter space associated with the minimal loss function is extracted. Adaptations can be made to this algorithm, such as incorporating a bias into the assigned velocity of the particles to encourage movement towards local/global minima found prior to the current iteration. The local best method encourages particles to move towards the minimum in its local neighbourhood using a bias in the velocity, while the global best method sets the bias towards the minimum in the entire parameter space.

Petrovski et al [171] used particle swarm to optimise chemotherapy treatment for their model of cancer tumour populations. The objective function to minimise for optimisation was the sum of the tumour cell populations at each time point over the course of the simulation. The optimisation used 50 particles placed randomly in the parameter space. On each of the 30 iterations performed, the particles were given a biased velocity towards the best values found thus far. The efficiency of using a local best and global best method were compared, with the global method reaching a feasible solution in a considerably lower number of iterations.

Instead of having a single objective function such as tumour size over time, particle swarm can be used to optimise multiple objective functions at once. Shindi et al [200] used two objective functions in the optimisation, minimising the total tumour size over time while also minimising the total drug used. These two results are stored for each particle after each iteration, with pareto optimal solutions found across the parameter space. This generates a pareto front, consisting of values which cannot be optimised further for either objective function. Using the values in this pareto front, a weighting was assigned between the two objective functions depending on the importance between minimising the tumour population and the dosage given to the patient. This weighting determined how far along the pareto front the optimised values were taken.

The approaches taken to mathematical modelling of drug effects, such as the affected cell types, effect function, or methods taken to include DNA damage, show a high variation from model to model. As a result, the decision made by a modeller regarding which approach to take can have a key impact on the results and findings from the *in silico* experiments. ODE models are excellent at predicting overall temporal population sizes deterministically, with the potential of analytically found results that can give important predictions for cancer treatment responses. Agent-based models allow for a more spatial approach, with dynamics studied on a more individualised level. The stochastic nature of these models can allow for more biologically realistic dynamics, though carrying out analysis on agent-based models is generally more troublesome than on ODE models.

Multiple approaches are taken, such as ODE models with patient specificity, added noise, and drug decay. Compartment models were introduced to allow for damage to cells or splitting the population into different cell types, as well as models to account for the synergistic effects of administering multiple drugs at once. Rather than approaching death as a rate, agent-based models take death as a probability to occur during an iteration. These models tend to utilise a Hill function in their dynamics, incorporating the IC_{50} value, the concentration of drug at which 50% of the cell population is killed.

Finding the values of model parameters such as the IC_{50} value is critical for accurate and meaningful results. While some values can be found in the literature, often drug, cell line, or model specific parameters have not been previously found and so require data found experimentally to be optimised. These approaches have a high variation in rigour and speed, allowing a modeller to choose which level of detail they wish their parameter search to undergo. If the modeller has prior knowledge regarding these values, Bayesian optimisation can be used to account for this knowledge whilst still incorporating the data found experimentally. While grid search is exhaustive of every parameter combination, a modeller may be constrained by time and require an approach with an individualised termination point, such as the particle swarm algorithm.

Modelling chemotherapy is crucial in improving the understanding of the impact that different treatment protocols can have on cancer tumours. The development of a range of mathematical models allows different aspects of cancer dynamics to be explored, broadening the knowledge without the need for additional extensive *in vitro* or *in vivo* experiments. These improvements can help improve the treatment administered to patients, increasing the survival rates and quality of life for patients of the disease.

4.2 Model Outline and Optimisation

The approach taken in this chapter builds upon on the model developed in Chapter 3, with the key adaptations being in the cycling and apoptosis rates. Data is obtained for cisplatin treatments at dosages of 0, 1, 3.125, 6.25, 12.5, 25, 50, 100, and 200mg/m^2, with live cell populations counted initially and subsequently every 24 hours for 72 hours. For each setting, total tumour populations are measured across three repeats, with results normalised to the initial populations. Optimisation is performed by running simulations with various parameter values, and comparing the results with those found biologically by quantifying the error.

Suppose $X(t)$ and $Y(t)$ denote the live cell population at time point t for an *in silico* simulation and *in vitro* experiment respectively, the error, $RMSE$, is given in

Equation 4.11,

$$RMSE = \sqrt{\frac{\sum_{t=1}^{4}(X(t) - Y(t))^2}{4}}. \tag{4.11}$$

A short example of how Latin hypercube sampling (LHS) and the $RMSE$ can be used to optimise multiple parameters simultaneously is highlighted in the box below. We take an initial estimate for each parameter and a range that this value can take, creating an array of equally spaced values for each parameter. Each parameter value in each array is then randomly assigned to a simulation.

Suppose there are two parameters, p_1 and p_2, to perform global parameter optimisation on. We make an initial estimate of 20.0 for the value of p_1 and 50.0 for the value of p_2 based on some previous knowledge, and have a high confidence in the values of these parameter so have a range of only ± 10%. If we want to test five values of each parameter, then p_1 would generate an array of [45,47.5,50,52.5,55] and p_2 an array of [18,19,20,21,22]. The elements of each of these arrays are then randomly assigned to a simulation, as shown in Table 4.3. After the completions of the simulations with their associated parameter values, the $RMSE$ is compared across each of the five runs.

Simulation Number	p_1 value	p_2 value	$RMSE$
1	52.5	22	0.021
2	45	21	0.038
3	47.5	18	0.014
4	55	20	0.031
5	50	19	0.017

TABLE 4.3: **Procedure used for LHS optimisation**. Here, two parameters and five simulations are tested, with the $RMSE$ value shown in the right hand column. Results suggest that the optimal value of p_1 is 47.5 and 18 for p_2 since these lead to the smallest $RMSE$ value.

Here we see that simulation 3 gives rise to the lowest $RMSE$ when compared to the data, and so we assume that 47.5 is the optimal value of parameter p_1 and 18 is the optimal value of parameter p_2.

4.2.1 Optimisation of Proliferation Rates

To allow for cell line specific optimisation of cycling rates, Equation 3.2 is carried forward with some small adaptations. Here, the cell cycling rate, b_c, is a cell line specific parameter which is assumed to change between cell lines, while c_c, p_c, and o_c remain independent of the cell line. Alongside this, observations of the experimental data provided suggest an adaptation to the logistic growth term may be required. Tumours appear to grow rapidly at low populations, with overall growth rates appearing to have a negative correlation to tumour size. Equation 4.12 shows the new approach taken to the population dynamics in the remainder of this chapter,

$$r_c = b_c \cdot c_c \cdot p_c \cdot o_c \cdot \left(\frac{K}{n} - 1 \right). \tag{4.12}$$

The current number of live cells in the tumour is denoted as n, with the carrying capacity due to available volume for the tumour grow in *in vitro* experiments represented by K. While a logistic growth term would produce an S shaped curve, dividing this term by $\frac{n}{K}$ would generate an increasing concave down population curve, as observed in the untreated experimental results.

For simplicity, we focus on the two constant parameters involved in Equation 4.12 in this section for parameter optimisation: the cell cycling rate, b_c, and the carrying capacity, K. The other terms depend on dynamic conditions such as those in the microenvironment, leading to excessive complexity when optimising their functions.

Firstly, we aim to optimise the rates of proliferation in cells by assuming that the cell line specific values of the cell cycling rate, b_c, and carrying capacity, K, remain constant regardless of the cisplatin treatment dosage. We initially estimate the cell cycling rate and carrying capacity parameter values for each cell line, informed by an inspection of the data when no drug is present and testing different values until the trends appear similar between the simulation and biological experiment. A parameter range of ± 20% is then used on these values to ensure a large range of parameters are tested, reducing the dependency on our initial estimates for their values. For each round of optimisation, 21 different values are used for each parameter, meaning 21 different simulations are performed with the $RMSE$ calculated across the simulations using Equation 4.11.

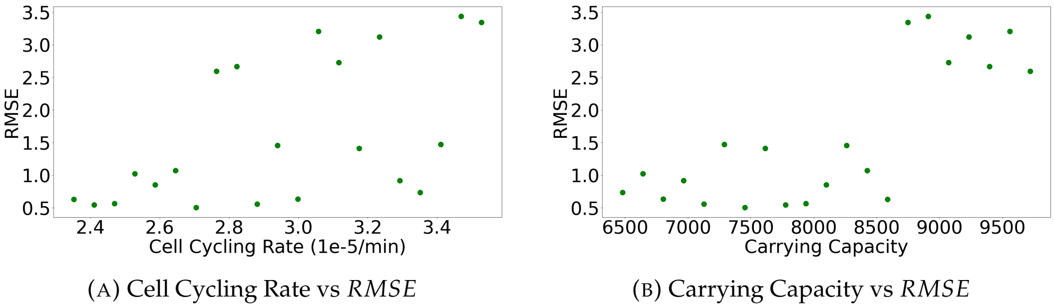

(A) Cell Cycling Rate vs *RMSE*

(B) Carrying Capacity vs *RMSE*

FIGURE 4.2: ***RMSE* for various simulations using different proliferation related parameters.** To find the optimal parameter values when comparing to the in vitro data, different values of the cell cycling rate, b_c, and carrying capacity, K, were tested. Simulations with the lowest *RMSE* when compared to the data were assumed to use optimal parameters.

Figure 4.2 shows the results from an example run of LHS for SKOV-3 wild type cells, comparing the *RMSE* with the parameter values for b_c and K in Equation 4.12. In this example, an initial cell cycling rate of $2.9e-5/\text{min}$ and carrying capacity of 8000 was investigated based on the initial observations of simulation results.

The *RMSE* results shown in Figure 4.2 have no clear positive or negative trends between the parameter values and *RMSE*, suggesting the optimal values are within the parameter ranges that were tested. The cell cycling rate and carrying capacity generate a minimum *RMSE* value at around $2.7e-5/\text{min}$ and 7452 respectively. The temporal population dynamics from this simulation are shown in Figure 4.3, showing a general agreement between the *in vitro* results in blue and the *in silico* results in green.

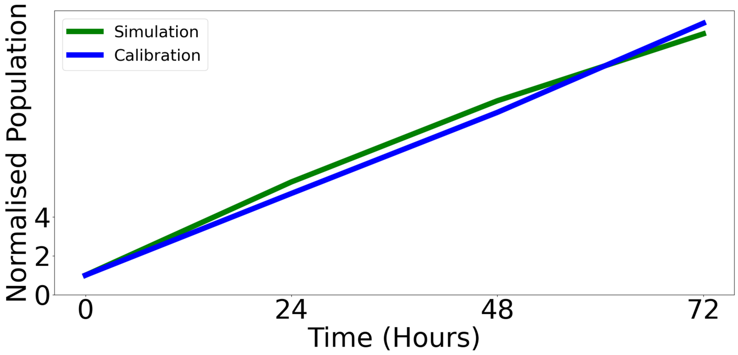

FIGURE 4.3: **Example temporal dynamics comparing model and experimental results.** Populations were tracked over 72 hours for *in silico* (green) and *in vitro* (blue) experiments, with populations normalised to the initial value.

Cell Line	Cycling Rate (b_c)	Carrying Capacity (K)
SKOV-3 Wild Type	0.0000270	7452
OVCAR-3 Wild Type	0.0000602	13680
SKOV-3 Cisplatin Resistant	0.0000696	5280
OVCAR-3 Cisplatin Resistant	0.0000193	15120

TABLE 4.4: **Proliferation related parameter values.** Values for the cycling rate and carrying capacity are optimised for each cell line individually using data from the control experiment. These values are used throughout the remainder of the chapter.

We perform this parameter optimisation on four ovarian cancer cell lines in this way, with wild type and cisplatin resistant variations of SKOV-3 and OVCAR-3 cells. For each cell line, we use data collected from the control experiments to optimise the cell cycling rate and the carrying capacity. We assume these parameters may be different across cell lines due to the differences in phenotypic behaviours and physical characteristics. The cell cycle rate and carrying capacity parameter values leading to the lowest $RMSE$ are shown in each respective cell line in Table 4.4.

4.2.2 Optimisation of Apoptosis Rates

Cisplatin is a DNA-damaging drug which can reduce the size of ovarian cancer tumours in multiple ways [193]. Apoptosis rates have been found to increased as a result of exposure to cisplatin in rapidly cycling cells [131]. The DNA adducts within rapidly cycling cells induce apoptosis when exposed to cisplatin, causing increased death rates within the tumour [131, 76]. Extended exposure to cisplatin is also found to cause prolonged DNA damage, leading to increased rates of cell death [3]. Apoptosis rates in this chapter are therefore assumed to depend on two aspects of the treatment given to the tumour:

- The current concentration of drug that a cell is located in.
- The damage that a cell has taken during its lifetime due to drug exposure.

After each iteration of the simulation, a value proportional to the concentration of cisplatin in which a cell is placed is added to a cumulative total of cell damage, leading to cells situated in higher concentrations of cisplatin over time to become more damaged. Equation 4.13 shows how the damage is accumulated in a cell using an iterative process,

$$damage(x_i, t+1) = damage(x_i, t) + \frac{cisplatin(x_i, t)}{1000}. \tag{4.13}$$

In this equation, $damage(x_i, t)$ denotes the damage in the i^{th} cell on iteration t when placed in a microenvironment with cisplatin concentration $cisplatin(x_i, t)$. A division of 1000 is included simply to prevent the $damage(x_i, t)$ variable from having an excessive number of digits.

Quantifying how these $cisplatin(x_i, t)$ and $damage(x_i, t)$ variables impact the death rate of cell i is the main focus of this chapter. Later in this section, the value of $damage(x_i, t)$ will generate a new damage impact variable, dam_d, incorporated into the apoptosis rate according to Equation 4.14,

$$r_d = b_d \cdot (1 + dam_d + cis_d). \tag{4.14}$$

The cisplatin concentration, $cisplatin(x_i, t)$, will also generate a new drug impact variable, cis_d, included in this equation. Instead of the historical conditions of the cell, this cis_d variable is based only on the current concentration of cisplatin in which a cell is situated. This ensures drugs can still have an impact on the death rate of a cell without any significant prior exposure or accumulated damage. Here, r_d represents the death rate of a cell (1/min), dam_d the damage impact parameter, and cis_d the drug impact parameter. The base death rate parameter, b_d, is set to $1e-5$ /min, the minimum death rate value of OVCAR-3 cells used previously in Chapters 2 and 3.

Since there is a small amount of drug uptake by the cells, as well as a decay rate over time, the concentration of drug becomes heterogeneous through both space and time. Therefore, we cannot assume that cells treated with 10mg/m^2 remain in 10mg/m^2 of cisplatin throughout the 72 hour simulation. We aim to build functions for how the cell damage (*damage*) and drug concentration (*cisplatin*) variables for each cell respectively correlate to the damage impact (dam_d) and drug impact (cis_d) variables in Equation 4.14. This is done by partitioning the function into sections, with each section of the function corresponding to a different dosage. For example, the first section for the drug concentration would be between 0 and 1mg/m^2, the second would be between 1 and 3.125mg/m^2, the third between 3.125 and 6.25mg/m^2, and so on.

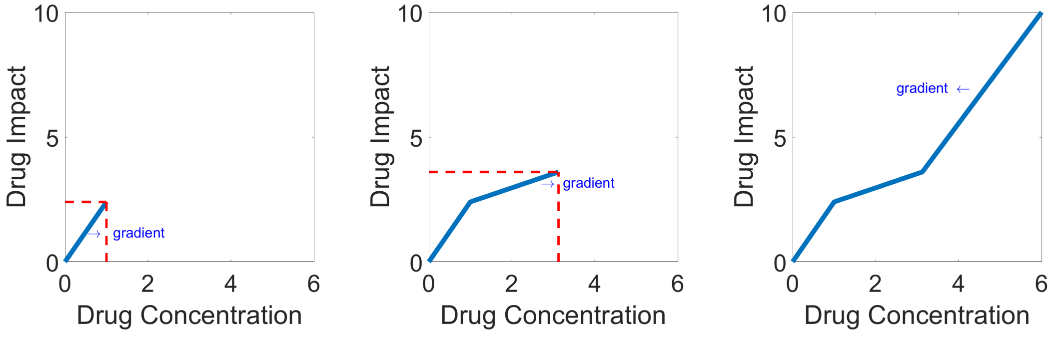

(A) Example of optimising the gradient at dosage 1mg/m^2.

(B) Example of optimising the gradient at dosage 3.125mg/m^2.

(C) Example of optimising the gradient at dosage 6.25mg/m^2.

FIGURE 4.4: **Optimisation process for drug and damage impact parameters**. Impact parameter curves are optimised by building upwards through the different dosages. The error between a range of gradients is calculated, with the gradient associated with the lowest error saved and used for future simulations.

The same partition would also be performed for the accumulated damage, with the partitions based on the maximum accumulated damage during the simulations at each dosage. For example, the first section for the accumulated damage would be between 0 and 0.543, the second would be between 0.543 and 1.733, and so on. LHS is then performed on each section one at a time, building up from the lowest dose section to the highest, each time generating a range of possible gradients used for a linear correlation between the drug concentration and drug impact variables in that section, alongside the accumulated damage and damage impact variables simultaneously. The optimised gradient is selected by calculating the $RMSE$ from the data for each simulation and recording the gradient that led to the minimised error. The gradients are then stored and the correlation remains constant for that section in all future simulations. This is repeated for all partitions until all treatment dosages have been analysed, up to 200mg/m^2. Figure 4.4 shows an example of these steps by building upon the optimisation of the drug impact curve with respect to drug concentration, where the blue line represents the gradient associated with the minimum $RMSE$ from the data in each section. The line plot generated by optimising the gradients is next converted into a scatter plot, with each point representing optimised values from a new dosage of treatment. Since the control experiment is redundant when using data to optimise the drug effects, this leads to eight points, one for each treatment dosage. A linear/Emax curve is then fitted to these points for the damage impact and drug impact parameters, allowing us to make predictions for dosages not tested experimentally. An overview of the optimisation process performed for each cell line is given in a step by step guide below.

1. Take the calibration data found experimentally for the control case in which no treatment is introduced.
2. Perform LHS on this calibration data to minimise the $RMSE$ from the simulation output, optimising the cell cycling rate parameter and carrying capacity for each cell line.
3. Set these as the optimised parameter values for the respective cell line, used for all future simulations irrespective of the drug dosage.
4. Take the experimental calibration data for the first drug dosage, set to 1mg/m^2 of cisplatin.
5. Perform LHS on the gradient of the drug impact parameter from 0 to 1mg/m^2 of drug concentration and on the gradient of the damage impact parameter from 0 to 0.543 of damage.
6. Set these as the gradients in these ranges of the corresponding x axes for each impact parameter.
7. Take the calibration data for the next dosage, 3.125mg/m^2.
8. Perform LHS on the gradient of the drug impact parameter from 1 to 3.125mg/m^2 of drug concentration and on the gradient of the damage impact parameter from 0.543 to 1.733 of damage.
9. Set these as the gradients in these ranges of the corresponding x axes for each impact parameter.
10. Take the calibration data for the next dosage, 6.25mg/m^2.
11. Repeat these steps of extracting the relevant calibration data, performing LHS, and optimising the gradients of the corresponding section of the plots until all gradients have been optimised up to 200mg/m^2 and 116.234 damage.
12. Extract the points on these plots that correspond to each dosage (1mg/m^2, 3.125mg/m^2, ..., 200mg/m^2 for the drug impact parameter and 0.543 damage, 1.733 damage, ..., 116.234 damage for the damage impact parameter).
13. Generate a linear fit to these points using a $y = m \cdot x$ function.

14. Repeat the simulations using these linear functions for the drug impact and damage impact parameters, comparing the new simulation results at each dosage to the calibration and validation data found experimentally.

15. If the comparisons appear adequate, assume a linear fit is sufficient. Otherwise, return to step 13 and instead fit these points using the Emax function shown later in Equation 4.15, repeating the simulations using this new fitting.

SKOV-3 Wild Type

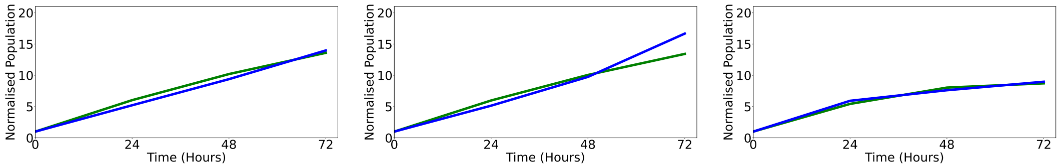

(A) 0mg/m^2 (B) 1mg/m^2 (C) 3.125mg/m^2

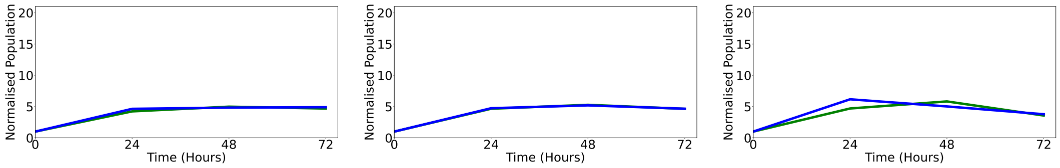

(D) 6.25mg/m^2 (E) 12.5mg/m^2 (F) 25mg/m^2

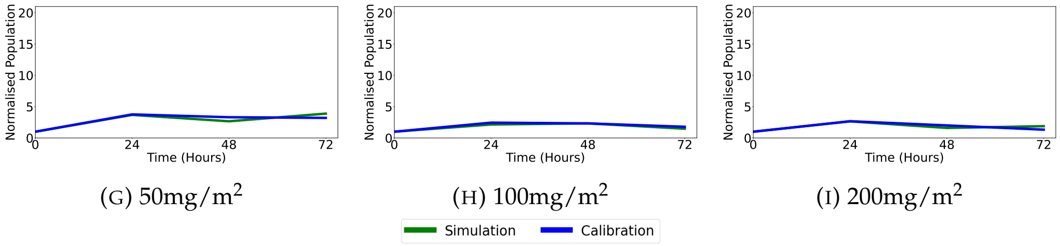

(G) 50mg/m^2 (H) 100mg/m^2 (I) 200mg/m^2

FIGURE 4.5: **Temporal dynamics of SKOV-3 wild type cell populations using optimal impact curves for the given drug dosage.** The green curves represent the simulation results and the blue curves represent the *in vitro* calibration results, with general agreement observed between the two across all dosages tested.

Figure 4.5 shows the results from the first parameter optimisation of SKOV-3 wild type cells. The optimised value for each dosage has a relatively good fit to the data. The general trends are captured, with small variations observed between the simulation and calibration data at 1mg/m^2 and 25mg/m^2.

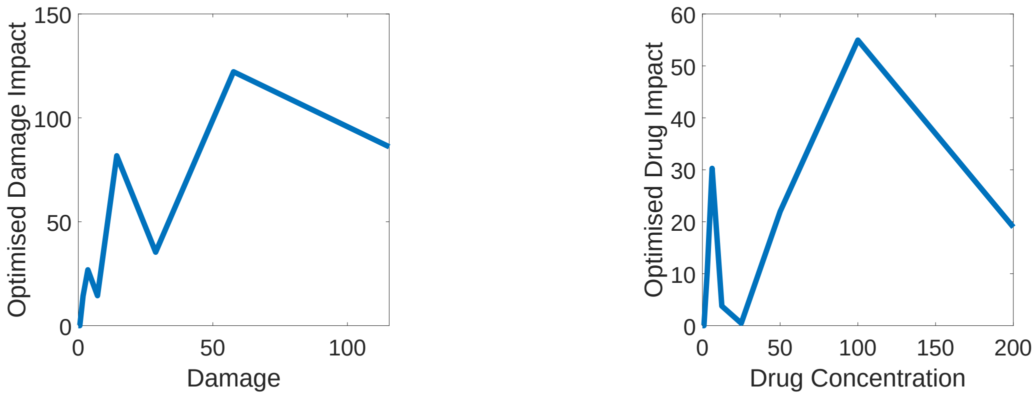

(A) Optimal curve fitted to the values of damage impact with respect to accumulated damage for each cell.

(B) Optimal curve fitted to the values of drug impact with respect to surrounding drug concentration for each cell.

FIGURE 4.6: **Optimal impact curves fitted for SKOV-3 wild type cells.** These are the curves producing the lowest *RMSE* when compared to the data for SKOV-3 wild type cell lines for the accumulated damage impact (A) and drug impact (B).

The optimised parameter values at each dosage are then extracted and plotted for the damage impact and drug impact, as shown in Figure 4.6. These trends would ideally be monotonically increasing, as higher DNA damage and drug concentrations in the microenvironment should in turn increase apoptosis rates. Though this is not the case in Figure 4.6, the general trends show a positive correlation for both plots.

Linear Fitting

Each point used to generate the line plots in Figure 4.6 is extracted and transformed into a scatter plot, with one point for each non-zero dosage. To prevent the overfitting observed in Figure 4.6, a linear fit is then made to these points with a y intercept of zero, as shown in Figure 4.7. The red line provides the linear fitting for the damage impact (A) and the drug impact (B) in Figure 4.7. The gradient coefficient for these plots are shown in Table 4.5, using the linear plot $y = m \cdot x$ and optimised on MATLAB.

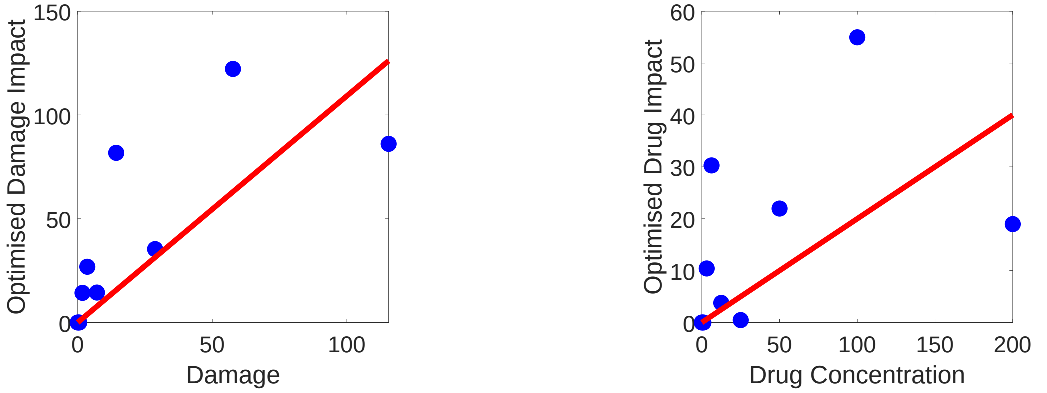

(A) Linear curve fitted to the optimised values of damage impact with respect to accumulated damage for each cell.

(B) Linear curve fitted to the optimised values of drug impact with respect to surrounding drug concentration for each cell.

FIGURE 4.7: **Fitted linear curves for SKOV-3 wild type cells.** The damage (A) and drug (B) impact parameters are optimised at each drug dosage and combined. Blue dots represent the optimised value at each separate drug dosage, with the red line showing the linear regression optimised across the points.

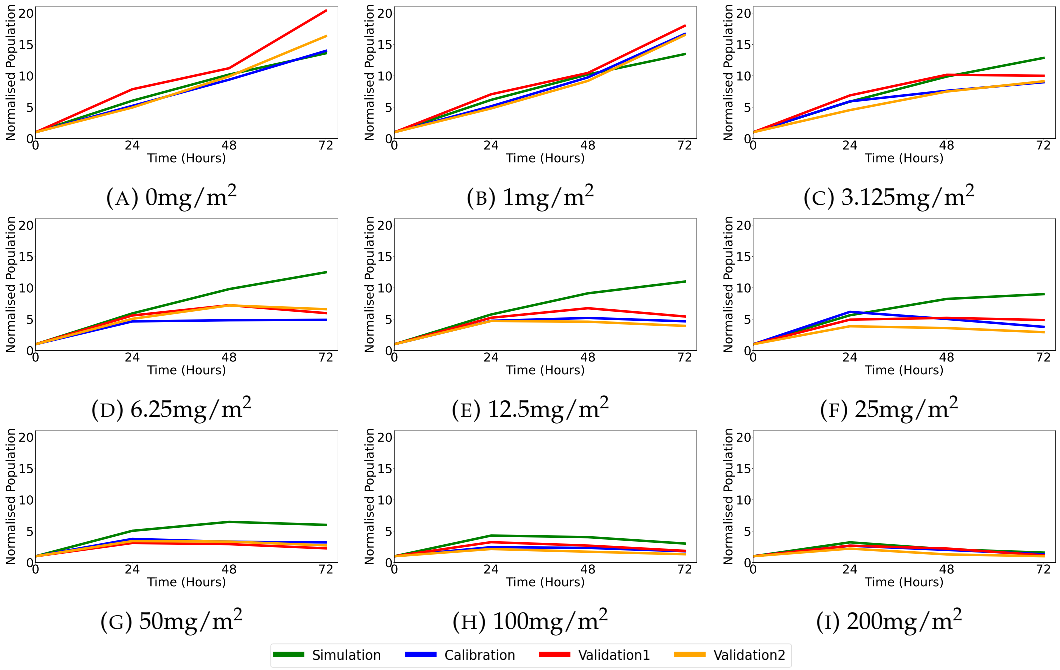

(A) 0mg/m^2

(B) 1mg/m^2

(C) 3.125mg/m^2

(D) 6.25mg/m^2

(E) 12.5mg/m^2

(F) 25mg/m^2

(G) 50mg/m^2

(H) 100mg/m^2

(I) 200mg/m^2

FIGURE 4.8: **Temporal dynamics of SKOV-3 wild type cell populations using linearly fitted parameter values.** Green curves represent the simulation results at each dosage, with blue curves representing the *in vitro* experimental results used for calibration. Red and yellow curves show the population dynamics found in *in vitro* experiments used for model validation.

y	x	m
Damage Impact	Damage	1.092
Drug Impact	Drug Concentration	0.200

TABLE 4.5: **Fitted linear coefficients for SKOV-3 wild type cells.** Increasing the drug concentration in which a cell is placed and the DNA damage carried out in the cell increases the apoptosis rate according to these fittings, with results shown in Figure 4.8.

Finally, simulations are run again at each drug dosage, this time using the parameters taken from the linear fits in Figure 4.7. At any given time, a cell with a certain damage variable in a certain concentration of cisplatin will extract its individual damage impact and drug impact parameters according to the linear fit shown in Figure 4.7. These values are incorporated into Equation 4.14, assigning the cell a death rate accordingly. The results at each dosage using this method can be used to compare the differences between the experimental data and the simulations in which this linear fit is used, as shown in Figure 4.8. Simulations using the values given by the linear fit (green) are compared with the calibration data (blue) along with two experimental repeats used for validation (red and yellow). Low dosages show a good fitting of the model to the data. The accuracy in the fitting is occasionally lost at medium dosages, despite the general trends continuing to be captured.

Emax Fitting

Figure 4.8 shows that when the linear fit in Figure 4.7 is implemented, the model loses a large amount of accuracy in the medium level dosages when compared to the validation and calibration data. This suggests that the linear approach may be under fitting the data. To explore this idea, we change the type of function used to fit the data to an Emax function, shown in Equation 4.15,

$$y = \frac{E_{max} \cdot x^{Hill}}{C_{50}^{Hill} + x^{Hill}}. \tag{4.15}$$

Figure 4.9 shows the fitted Emax curve to the same data points as before, with optimised coefficients provided in Table 4.6. This approach increases the death rate at low damage and dosages with a higher gradient observed near the origin.

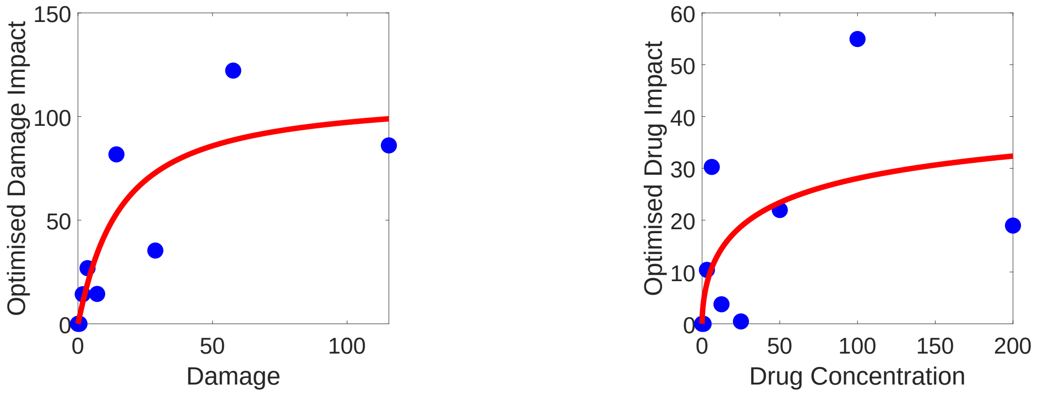

(A) Emax curve fitted to the optimised values of damage impact with respect to accumulated damage for each cell.

(B) Emax curve fitted to the optimised values of drug impact with respect to surrounding drug concentration for each cell.

FIGURE 4.9: **Fitted Emax curves for SKOV-3 wild type cells.** The damage (A) and drug (B) impact parameters previously optimised at each drug dosage and combined. Blue dots represent the optimised value at each separate drug dosage, with the red line showing the linear regression optimised across the points.

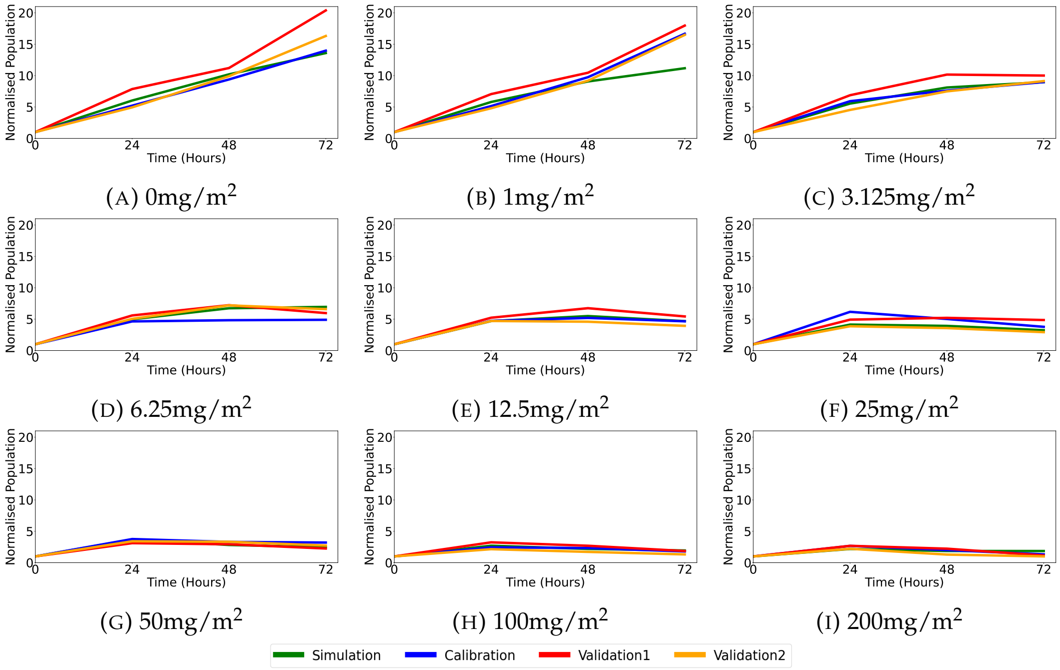

(A) 0mg/m^2 (B) 1mg/m^2 (C) 3.125mg/m^2

(D) 6.25mg/m^2 (E) 12.5mg/m^2 (F) 25mg/m^2

(G) 50mg/m^2 (H) 100mg/m^2 (I) 200mg/m^2

FIGURE 4.10: **Temporal dynamics of SKOV-3 wild type cell populations using Emax fitted parameter values.** Green curves represent the simulation results at each dosage, with blue curves representing the *in vitro* experimental results used for calibration. Red and yellow curves show the population dynamics found in *in vitro* experiments used for model validation.

y	x	E_{max}	$Hill$	C_{50}
Damage Impact	Damage	110.8	1.054	15.48
Drug Impact	Drug Concentration	47.07	0.5778	50.95

TABLE 4.6: **Fitted Emax coefficients for SKOV-3 wild type cells.** Increasing the drug concentration in which a cell is placed and the DNA damage carried out in the cell increases the apoptosis rate according to these fittings, with results shown in Figure 4.10.

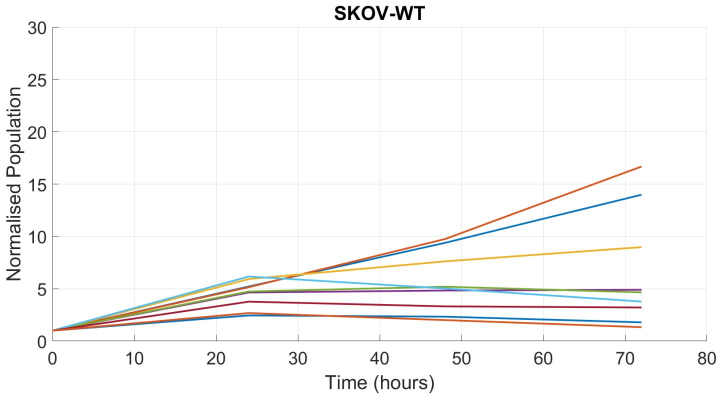

(A) Results used for model calibration at different drug dosages for SKOV-3 wild type cells.

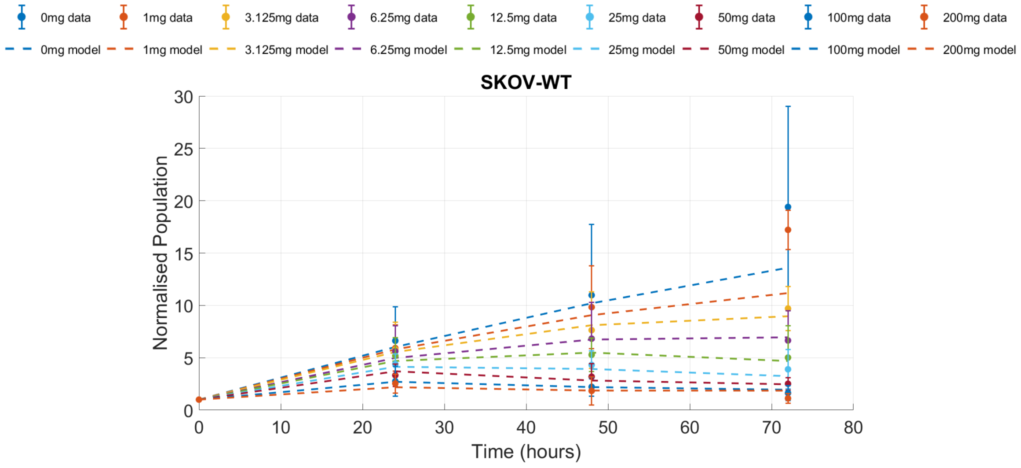

(B) Results used for model validation with 95% confidence intervals at different drug dosages for SKOV-3 wild type cells vs model simulation results.

FIGURE 4.11: **Comparison between calibration, simulation, and validation data for SKOV-3 wild type cells.** Results from the calibration data at each dosage (A), is compared with the results from validation data using error bars with simulation results shown in dashed lines (B).

As before, simulations are run again at each drug dosage. This time, the death raters for each cell are calculated using the Emax fits shown in Figure 4.9. Results from these simulations are shown in Figure 4.10. Simulations using the values given by the Emax fit (green) are compared with the calibration data (blue) and two repeats used for validation (red and yellow). Comparing these results with those found previously in Figure 4.7, the Emax approach provides a much improved fit to the data, with simulation results at almost all dosages appearing reasonable compared to the data.

As an alternative way to view the results, Figure 4.11 (A) provides the experimental data used to calibrate the model at each dosage. Figure 4.11 (B) shows the 95% confidence intervals found in the data used to validate the simulation results and compares these with the simulation output, plotted using the dashed lines. The model struggles to capture the very low dosages, however, has a good fit to those at higher treatment levels.

OVCAR-3 Wild Type

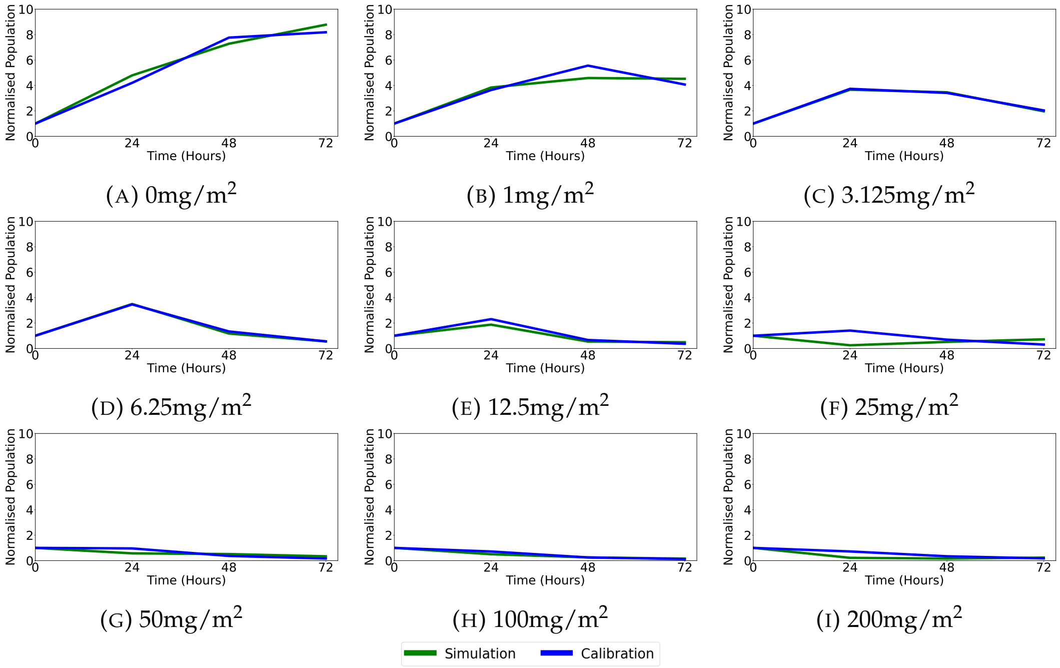

(A) 0mg/m^2 (B) 1mg/m^2 (C) 3.125mg/m^2

(D) 6.25mg/m^2 (E) 12.5mg/m^2 (F) 25mg/m^2

(G) 50mg/m^2 (H) 100mg/m^2 (I) 200mg/m^2

FIGURE 4.12: **Temporal dynamics of OVCAR-3 wild type cell populations using optimal impact curves for the given drug dosage.** The green curves represent the simulation results and the blue curves represent the *in vitro* calibration results, with general agreement observed between the two across all dosages tested.

The processes performed in Section 4.2.2 are then repeated for the remaining cell lines. Figure 4.12 compares the simulation results after the first parameter optimisation with the calibration data for OVCAR-3 wild type cells, with the optimal fittings of parameter values shown in Figure 4.13. Again, simulation results at lower dosages generally have a good fit to the data, with more notable differences appearing at medium dosages such as those observed for 25mg.

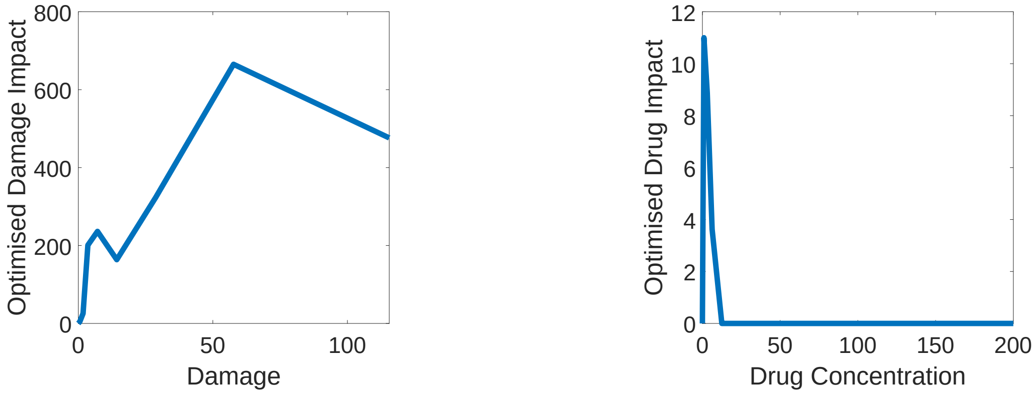

(A) Optimal curve fitted to the values of damage impact with respect to accumulated damage for each cell.

(B) Optimal curve fitted to the values of drug impact with respect to surrounding drug concentration for each cell.

FIGURE 4.13: **Optimal impact curves fitted for OVCAR-3 wild type cells.** These are the curves producing the lowest *RMSE* when compared to the data for SKOV-3 wild type cell lines for the accumulated damage impact (A) and drug impact (B).

Linear Fitting

After optimising a linear fit with coefficients shown in Table 4.7 to the results for the drug impact and damage impact parameters, the drug impact parameter appears to have a poor fitting. Since the scale of the drug impact shown in Figure 4.14 (B) is relatively small compared to the damage impact shown in Figure 4.14 (A), almost all of the death in OVCAR-3 wild type cells can be attributed to the accumulated DNA damage. The poor fitting for the drug impact parameter is therefore mostly unnoticeable when calculating the death rate in Equation 4.14.

y	x	m
Damage Impact	Damage	6.047
Drug Impact	Drug Concentration	0.001

TABLE 4.7: **Fitted linear coefficients for OVCAR-3 wild type cells.** Increasing the drug concentration in which a cell is placed and the DNA damage carried out in the cell increases the apoptosis rate according to these fittings, with results shown in Figure 4.15.

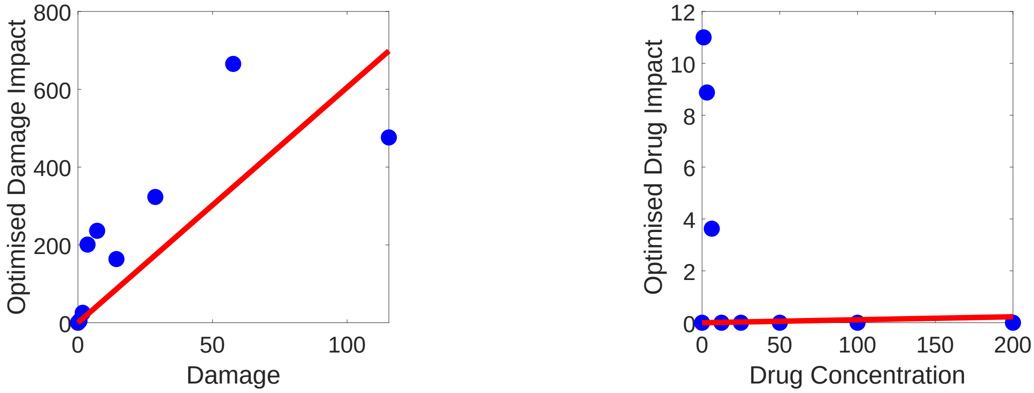

(A) Linear curve fitted to the optimised values of damage impact with respect to accumulated damage for each cell.

(B) Linear curve fitted to the optimised values of drug impact with respect to surrounding drug concentration for each cell.

FIGURE 4.14: **Fitted linear curves for OVCAR-3 wild type cells.** The damage (A) and drug (B) impact parameters are optimised at each drug dosage and combined. Blue dots represent the optimised value at each separate drug dosage, with the red line showing the linear regression optimised across the points.

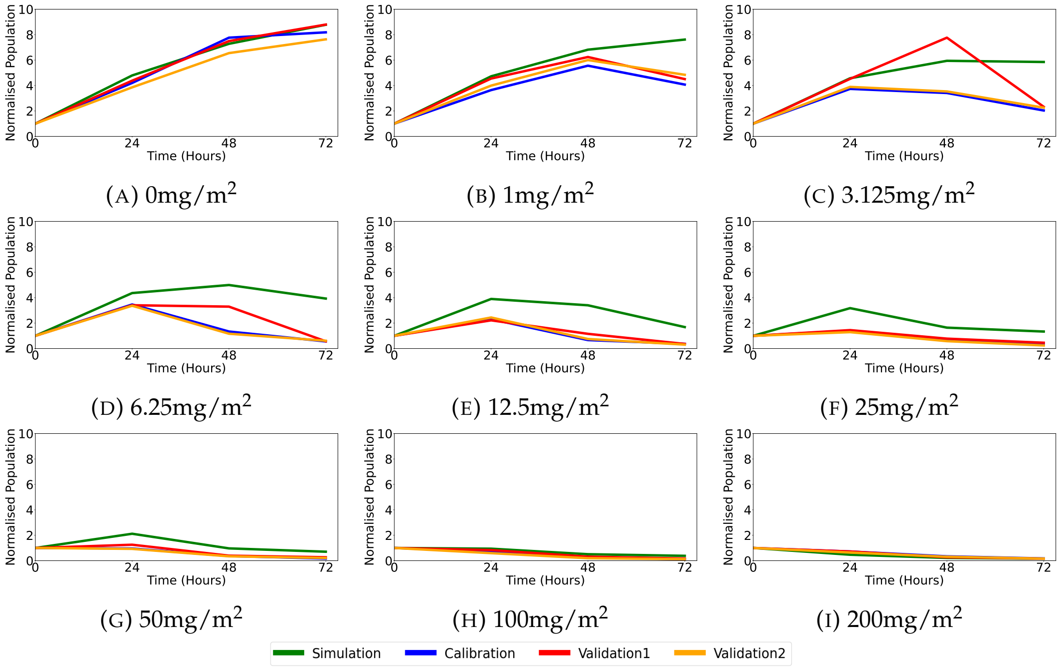

(A) 0mg/m^2 (B) 1mg/m^2 (C) 3.125mg/m^2

(D) 6.25mg/m^2 (E) 12.5mg/m^2 (F) 25mg/m^2

(G) 50mg/m^2 (H) 100mg/m^2 (I) 200mg/m^2

FIGURE 4.15: **Temporal dynamics of OVCAR-3 wild type cell populations using linearly fitted parameter values.** Green curves represent the simulation results at each dosage, with blue curves representing the *in vitro* experimental results used for calibration. Red and yellow curves show the population dynamics found in *in vitro* experiments used for model validation.

After simulating the model using the fittings shown in Figure 4.14, again we find in Figure 4.15 that the model is somewhat unable to capture the *in vitro* dynamics for medium dosages. The fit used for the damage impact parameter eluded to this, in which the linear curve appeared too low for most dosages, suggesting insufficient apoptosis could occur.

Emax Fitting

To combat this poor fitting at medium dosages, again an Emax fitting is used in place of the linear fitting. Figure 4.16 shows the Emax fitting to the points collected by the previous optimisation, with the relevant parameters given in Table 4.8. When compared with the linear fitting, this allows for an increased damage impact parameter for cells with a medium damage, creating higher rates of apoptosis and lower cell populations. As these dosages were responsible for the main discrepancies between the *in vitro* and *in silico* results in Figure 4.15, this change in death rate appears promising to improve on the results.

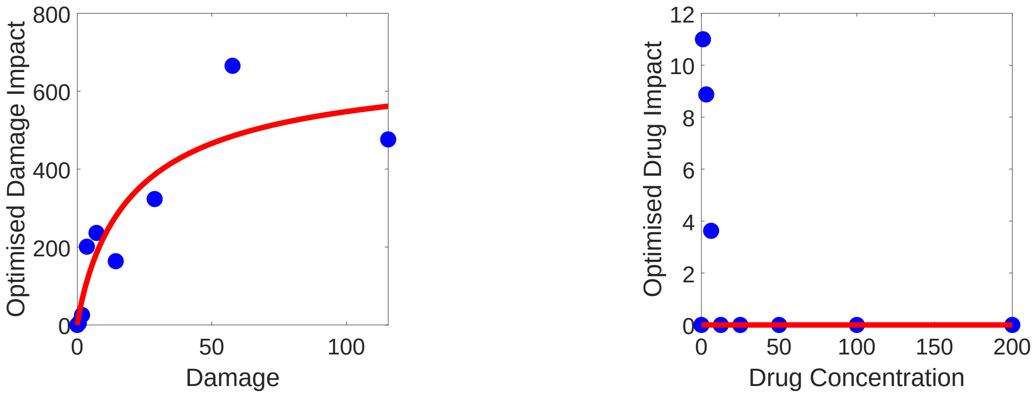

(A) Emax curve fitted to the optimised values of damage impact with respect to accumulated damage for each cell.

(B) Emax curve fitted to the optimised values of drug impact with respect to surrounding drug concentration for each cell.

FIGURE 4.16: **Fitted Emax curves for OVCAR-3 wild type cells.** The damage (A) and drug (B) impact parameters previously optimised at each drug dosage and combined. Blue dots represent the optimised value at each separate drug dosage, with the red line showing the linear regression optimised across the points.

E	*Conc*	E_{max}	*Hill*	C_{50}
Damage Impact	Damage	685.6	0.9033	21.74
Drug Impact	Drug Concentration	0	0	0

TABLE 4.8: **Fitted Emax coefficients for OVCAR-3 wild type cells.** Increasing the drug concentration in which a cell is placed and the DNA damage carried out in the cell increases the apoptosis rate according to these fittings, with results shown in Figure 4.17.

The resulting model dynamics are notably improved when compared with the *in vitro* data, as shown in Figures 4.17 and 4.18. The death occurring at medium dosages allows the model dynamics to capture the experimental trends with higher accuracy. The model remains limited at certain time points for certain dosages, potentially suggesting a flaw in either the model or the data for the OVCAR-3 wild type cell line.

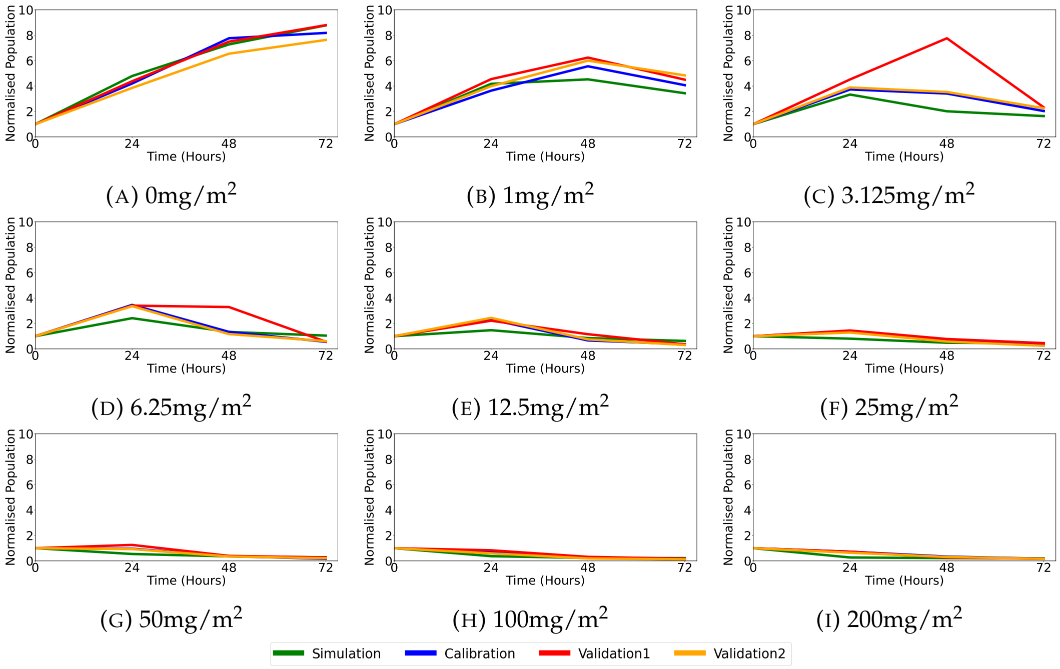

(A) 0mg/m^2 (B) 1mg/m^2 (C) 3.125mg/m^2

(D) 6.25mg/m^2 (E) 12.5mg/m^2 (F) 25mg/m^2

(G) 50mg/m^2 (H) 100mg/m^2 (I) 200mg/m^2

FIGURE 4.17: **Temporal dynamics of OVCAR-3 wild type cell populations using Emax fitted parameter values.** Green curves represent the simulation results at each dosage, with blue curves representing the *in vitro* experimental results used for calibration. Red and yellow curves show the population dynamics found in *in vitro* experiments used for model validation.

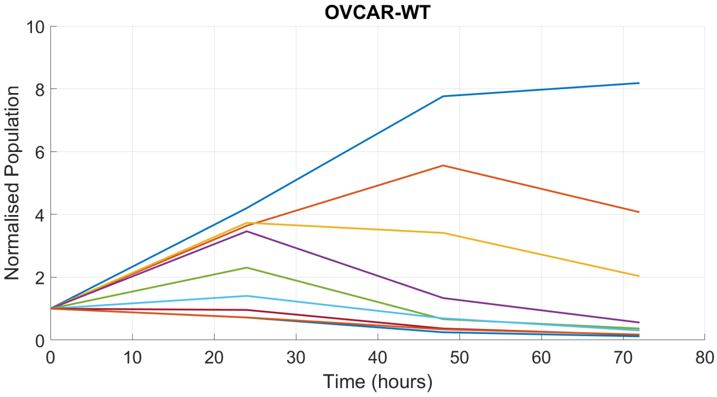

(A) Results used for model calibration at different drug dosages for SKOV-3 wild type cells.

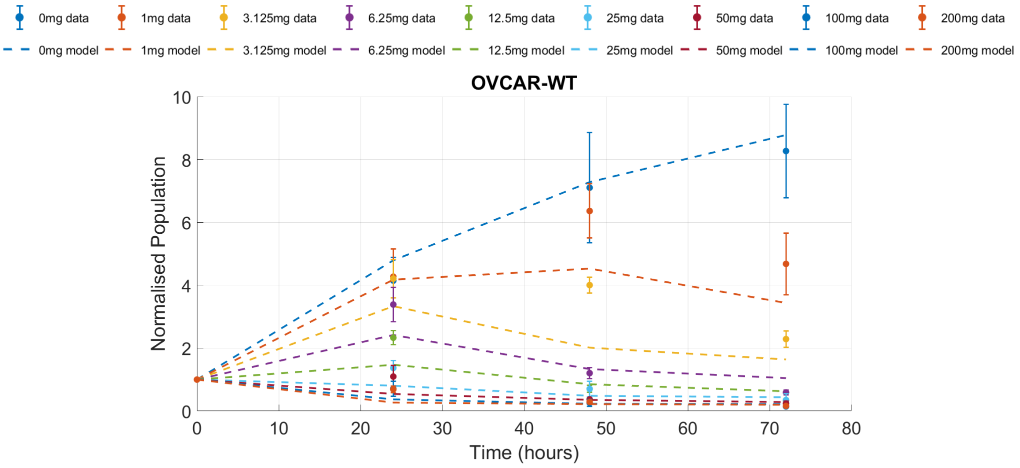

(B) Results used for model validation with 95% confidence intervals at different drug dosages for OVCAR-3 wild type cells vs model simulation results.

FIGURE 4.18: **Comparison between calibration, simulation, and validation data for OVCAR-3 wild type cells.** Results from the calibration data at each dosage (A), is compared with the results from validation data using error bars with simulation results shown in dashed lines (B).

SKOV-3 Cisplatin Resistant

Turning attention now to the cisplatin resistant cell lines, Figure 4.19 demonstrates that after the first optimisation shown in Figure 4.20 for SKOV-3 resistant cells at each dosage, the model has a good fit to the data. Low dosages show a small discrepancy between the simulation results and calibration data. At medium and high dosages, the simulation results appear similar to those found in the calibration experiments, with notable differences only at specific time points and dosages.

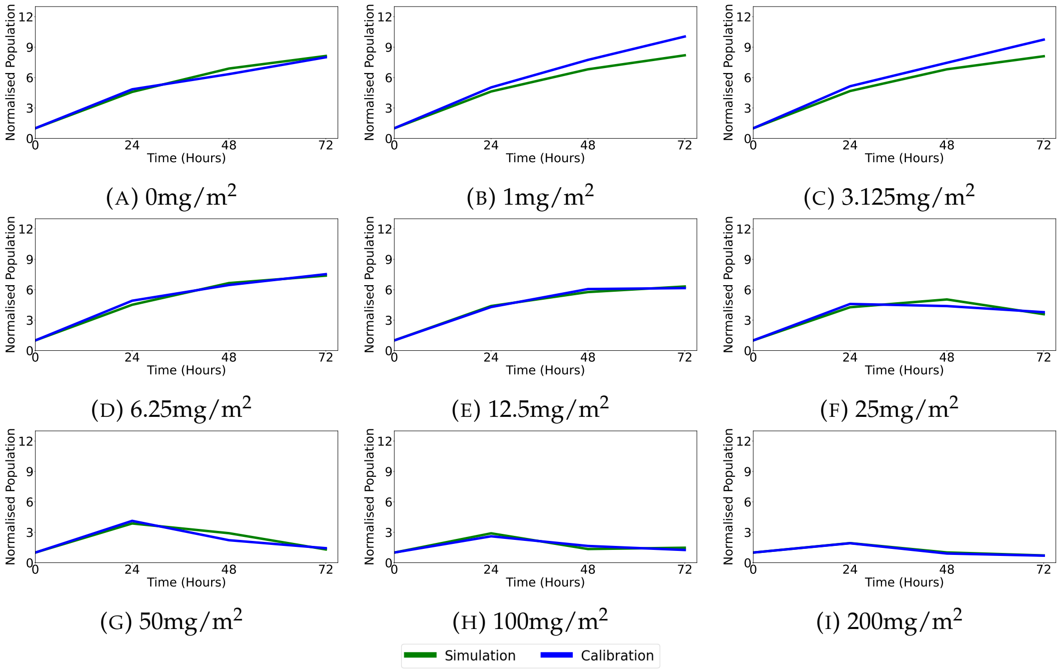

(A) $0\mathrm{mg/m^2}$ (B) $1\mathrm{mg/m^2}$ (C) $3.125\mathrm{mg/m^2}$

(D) $6.25\mathrm{mg/m^2}$ (E) $12.5\mathrm{mg/m^2}$ (F) $25\mathrm{mg/m^2}$

(G) $50\mathrm{mg/m^2}$ (H) $100\mathrm{mg/m^2}$ (I) $200\mathrm{mg/m^2}$

FIGURE 4.19: **Temporal dynamics of SKOV-3 cisplatin resistant cell populations using optimal impact curves for the given drug dosage.** The green curves represent the simulation results and the blue curves represent the *in vitro* calibration results, with general agreement observed between the two across all dosages tested.

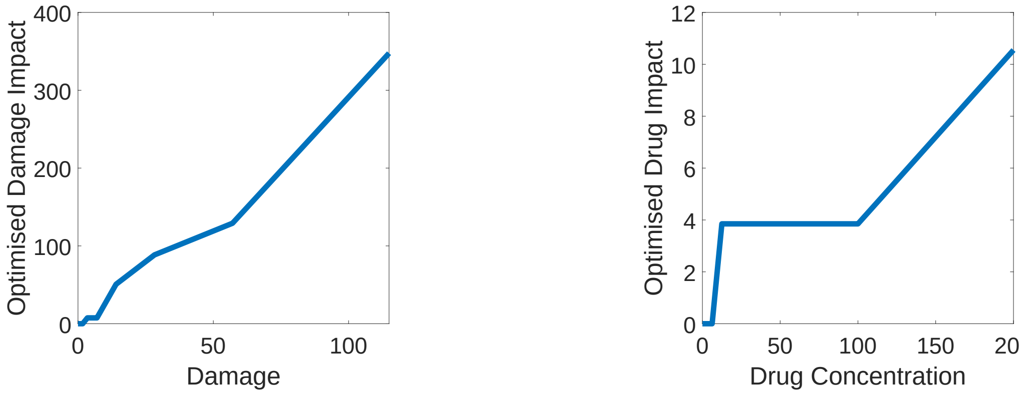

(A) Optimal curve fitted to the values of damage impact with respect to accumulated damage for each cell.

(B) Optimal curve fitted to the values of drug impact with respect to surrounding drug concentration for each cell.

FIGURE 4.20: **Optimal impact curves fitted for SKOV-3 cisplatin resistant cells.** These are the curves producing the lowest *RMSE* when compared to the data for SKOV-3 wild type cell lines for the accumulated damage impact (A) and drug impact (B).

The linear fit used for the production of results in Figures 4.22 and 4.23, with the associated gradient coefficient shown in Table 4.9. This produces the fit shown in Figure 4.21, with a very low gradient for the drug impact plot.

y	x	m
Damage Impact	Damage	2.886
Drug Impact	Drug Concentration	0.053

TABLE 4.9: **Fitted linear coefficients for SKOV-3 cisplatin resistant cells.** Increasing the drug concentration in which a cell is placed and the DNA damage carried out in the cell increases the apoptosis rate according to these fittings, with results shown in Figure 4.23.

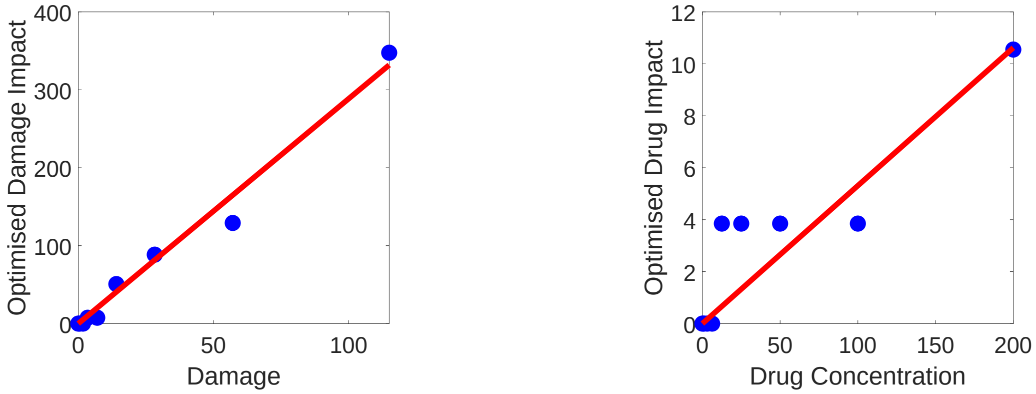

(A) Linear curve fitted to the optimised values of damage impact with respect to accumulated damage for each cell.

(B) Linear curve fitted to the optimised values of drug impact with respect to surrounding drug concentration.

FIGURE 4.21: **Fitted linear curves for SKOV-3 cisplatin resistant cells.** The damage (A) and drug (B) impact parameters are optimised at each drug dosage and combined. Blue dots represent the optimised value at each separate drug dosage, with the red line showing the linear regression optimised across the points.

Again, the magnitude of the drug impact parameter is very small when compared to the damage impact parameter. This suggests that the majority of cell death for SKOV-3 resistant cells will be due to the DNA damage accumulated over time. The linear fit for the damage impact parameter, as shown in Figure 4.21 suggests the potential for a linear fit to be sufficient in capturing the dynamics for this cell line, without the need of an Emax function for additional accuracy.

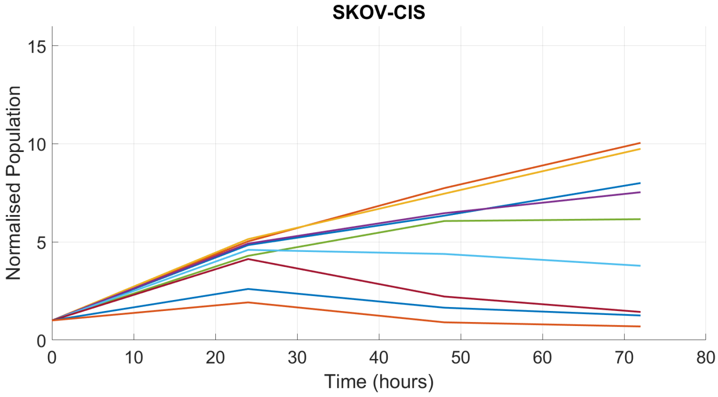

(A) Results used for model calibration at different drug dosages for SKOV-3 resistant cells.

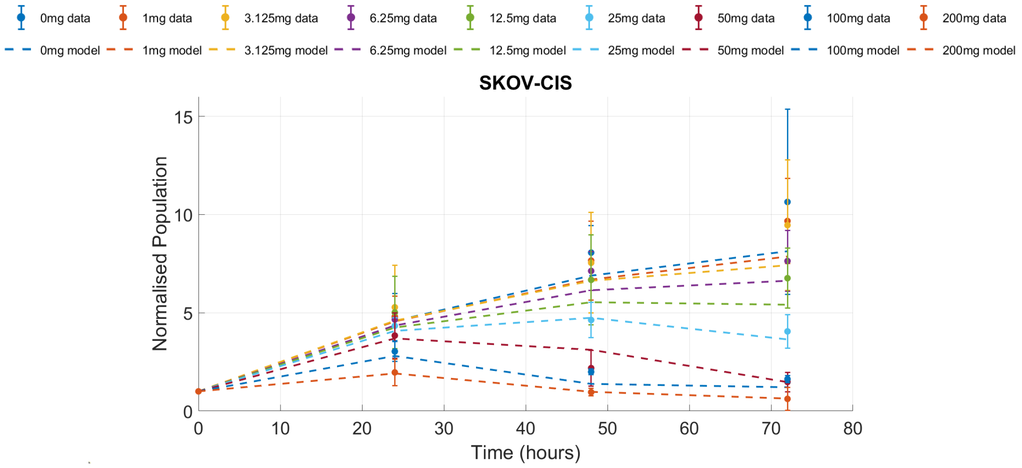

(B) Results used for model validation with 95% confidence intervals at different drug dosages for SKOV-3 resistant cells vs model simulation results.

FIGURE 4.22: **Comparison between calibration, simulation, and validation data for SKOV-3 cisplatin resistant cells.** Results from the calibration data at each dosage (A), is compared with the results from validation data using error bars with simulation results shown in dashed lines (B).

Simulations are re-run at each dosage using this linear fit, with model results in Figures 4.22 and 4.23 showing an excellent fit at most if not all dosages tested. The data used to calibrate the model shows that the untreated tumour has only the third highest rates of growth. The model removes this phenomenon, ensuring higher dosages always result in higher cell kill, also concluded by the validation data. This provides an example of where mathematical models can help to remove outliers from the experimental output that may otherwise be biologically irrelevant.

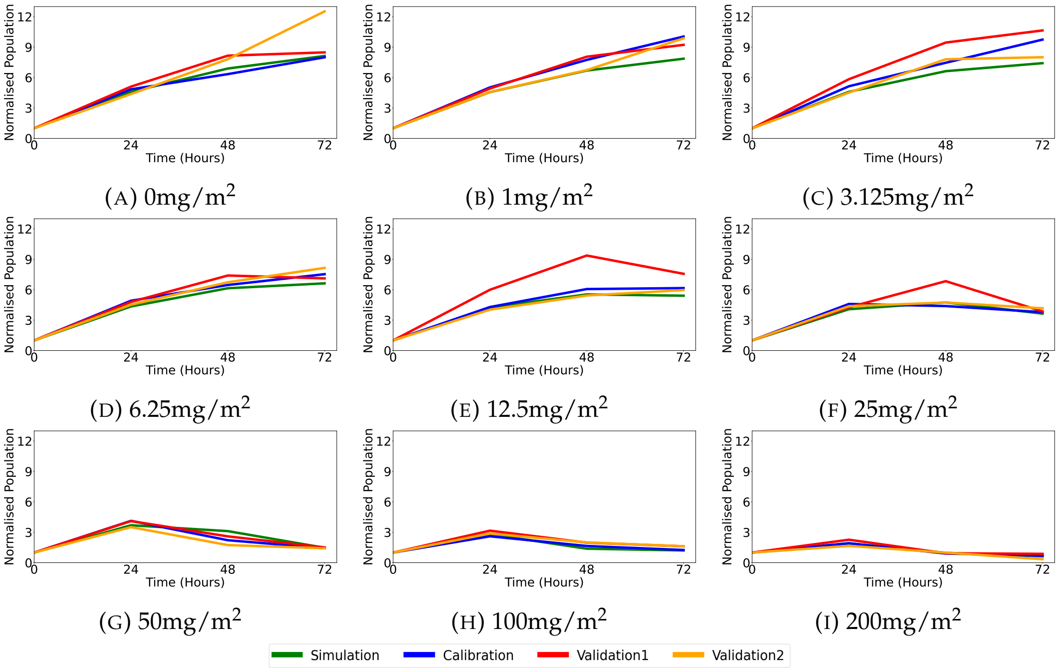

(A) 0mg/m^2 (B) 1mg/m^2 (C) 3.125mg/m^2

(D) 6.25mg/m^2 (E) 12.5mg/m^2 (F) 25mg/m^2

(G) 50mg/m^2 (H) 100mg/m^2 (I) 200mg/m^2

FIGURE 4.23: **Temporal dynamics of SKOV-3 cisplatin resistant cell populations using linearly fitted parameter values.** Green curves represent the simulation results at each dosage, with blue curves representing the *in vitro* experimental results used for calibration. Red and yellow curves show the population dynamics found in *in vitro* experiments used for model validation.

OVCAR-3 Cisplatin Resistant

Finally for the OVCAR-3 resistant cells, Figure 4.24 shows that at the optimised value for each dosage, the model has a good fit to the data with very small error. The optimised curves for the damage impact and drug impact parameters are shown in Figure 4.25.

y	x	m
Damage Impact	Damage	0.922
Drug Impact	Drug Concentration	0.328

TABLE 4.10: **Fitted linear coefficients for OVCAR-3 cisplatin resistant cells.** Increasing the drug concentration in which a cell is placed and the DNA damage carried out in the cell increases the apoptosis rate according to these fittings, with results shown in Figure 4.27.

A linear equation is fitted to the optimised damage and drug impact plots, shown in Figure 4.26, with gradient coefficients given in Table 4.10.

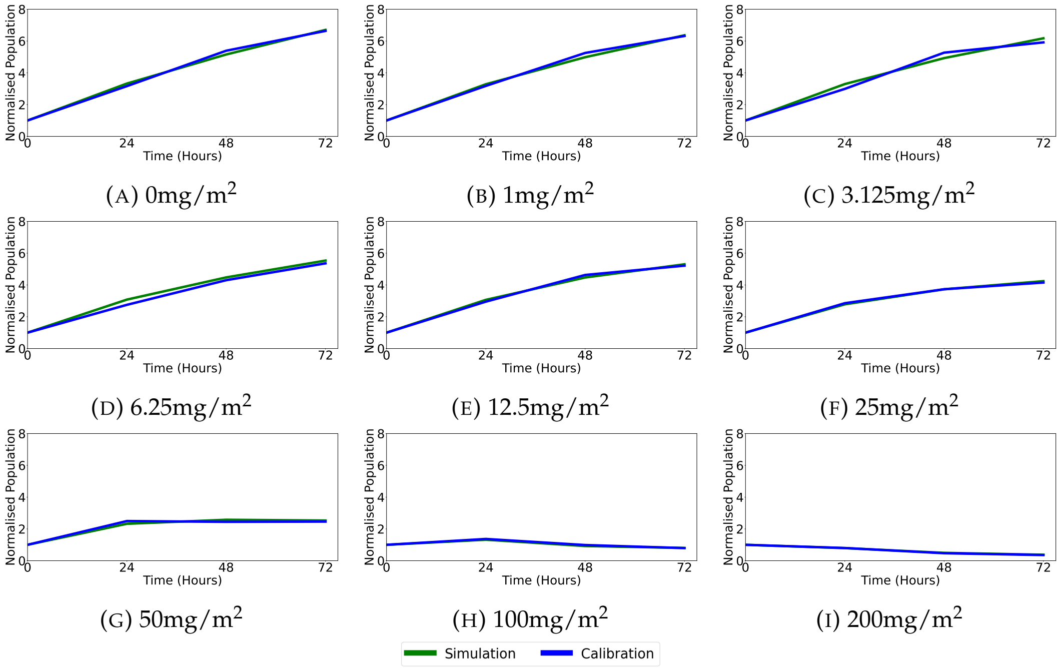

(A) 0mg/m^2

(B) 1mg/m^2

(C) 3.125mg/m^2

(D) 6.25mg/m^2

(E) 12.5mg/m^2

(F) 25mg/m^2

(G) 50mg/m^2

(H) 100mg/m^2

(I) 200mg/m^2

FIGURE 4.24: **Temporal dynamics of OVCAR-3 cisplatin resistant cell populations using optimal impact curves for the given drug dosage.** The green curves represent the simulation results and the blue curves represent the *in vitro* calibration results, with general agreement observed between the two across all dosages tested.

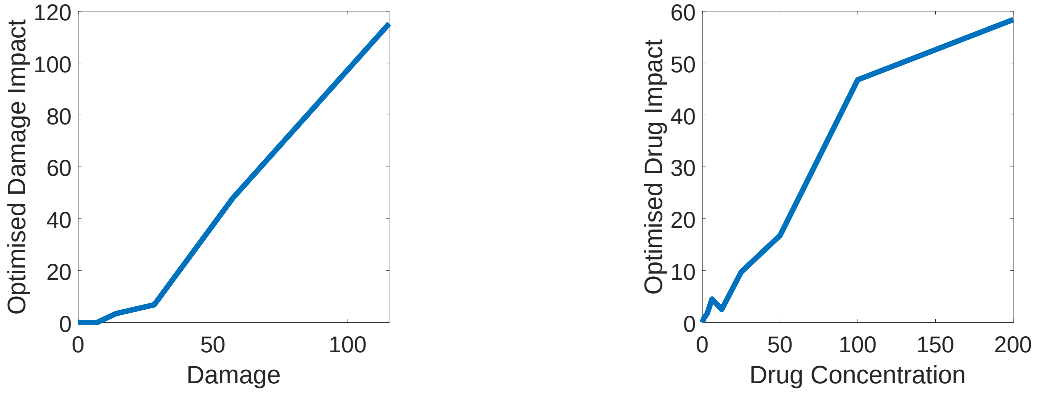

(A) Optimal curve fitted to the values of damage impact with respect to accumulated damage for each cell.

(B) Optimal curve fitted to the values of drug impact with respect to surrounding drug concentration for each cell.

FIGURE 4.25: **Optimal impact curves fitted for OVCAR-3 cisplatin resistant cells.** These are the curves producing the lowest *RMSE* when compared to the data for SKOV-3 wild type cell lines for the accumulated damage impact (A) and drug impact (B).

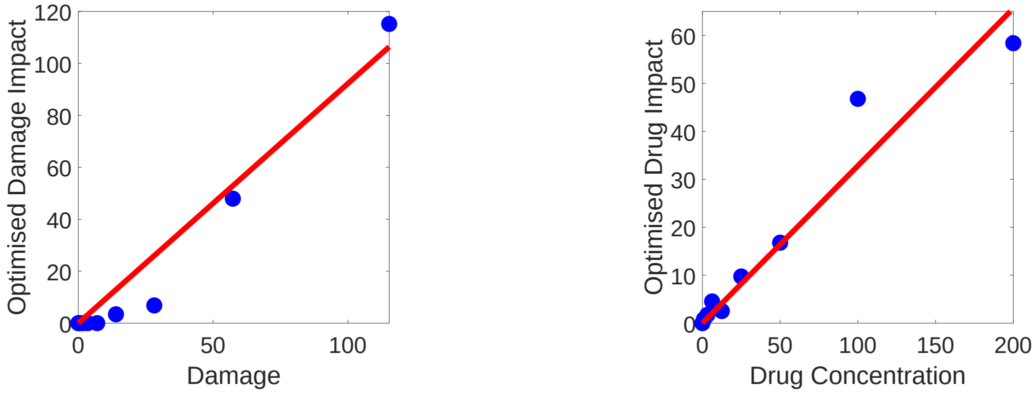

(A) Linear curve fitted to the optimised values of damage impact with respect to accumulated damage for each cell.

(B) Linear curve fitted to the optimised values of drug impact with respect to surrounding drug concentration for each cell.

FIGURE 4.26: **Fitted linear curves for OVCAR-3 cisplatin resistant cells.** The damage (A) and drug (B) impact parameters are optimised at each drug dosage and combined. Blue dots represent the optimised value at each separate drug dosage, with the red line showing the linear regression optimised across the points.

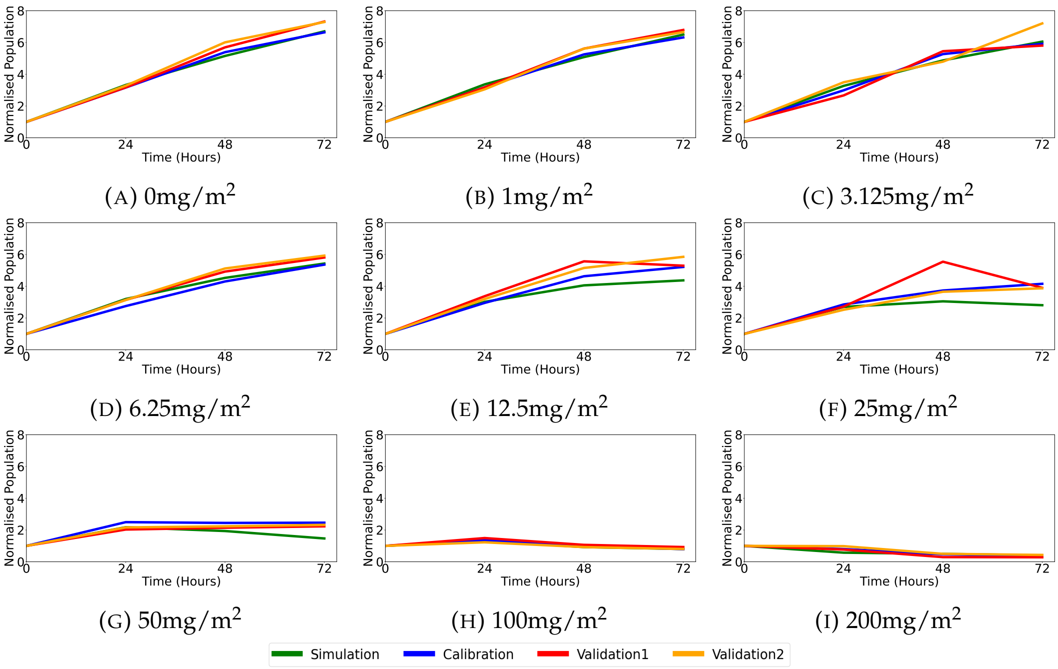

(A) $0\mathrm{mg/m}^2$

(B) $1\mathrm{mg/m}^2$

(C) $3.125\mathrm{mg/m}^2$

(D) $6.25\mathrm{mg/m}^2$

(E) $12.5\mathrm{mg/m}^2$

(F) $25\mathrm{mg/m}^2$

(G) $50\mathrm{mg/m}^2$

(H) $100\mathrm{mg/m}^2$

(I) $200\mathrm{mg/m}^2$

FIGURE 4.27: **Temporal dynamics of OVCAR-3 cisplatin resistant cell populations using linearly fitted parameter values.** Green curves represent the simulation results at each dosage, with blue curves representing the *in vitro* experimental results used for calibration. Red and yellow curves show the population dynamics found in *in vitro* experiments used for model validation.

Results using the values in this linear fitting in the simulations are shown in Figures 4.27 and 4.28. Since again these appear to be a good fit to the validation data, the Emax approach is not taken and a linear fit is assumed to be sufficient to a good model fit.

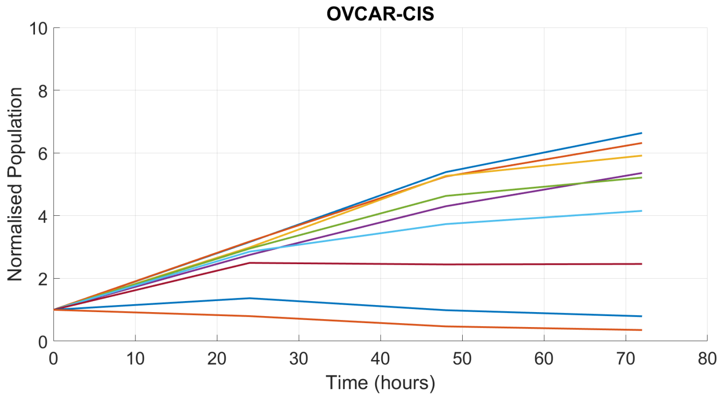

(A) Results used for model calibration at different drug dosages for OVCAR-3 resistant cells.

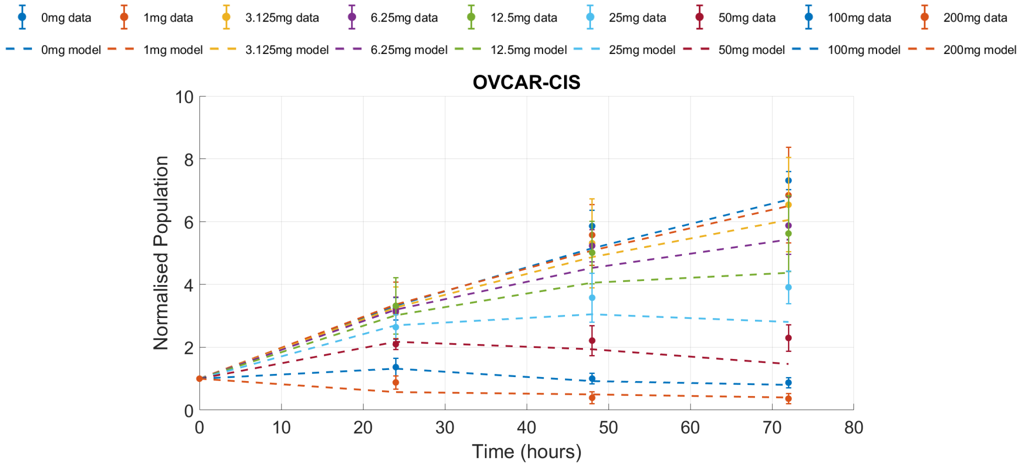

(B) Results used for model validation with 95% confidence intervals at different drug dosages for OVCAR-3 resistant cells vs model simulation results.

FIGURE 4.28: **Comparison between calibration, simulation, and validation data for OVCAR-3 cisplatin resistant cells.** Results from the calibration data at each dosage (A), is compared with the results from validation data using error bars with simulation results shown in dashed lines (B).

4.3 Results and Predictions

To make predictions using the newly fitted parameters and model, we create a setting that replicates a more *in vivo* setting with the aim of creating an environment similar to that in a patient. Spheroids are initialised in the spatial domain with varying proportions of wild type and cisplatin resistant cells. This helps to gain more insights into the impacts of tumour composition on the progression for different treatment protocols. Previously, the drug was initialised uniformly, with the only heterogeneity in cisplatin due to a small update rate from the cells. Here, vessels are introduced into the domain described later in Section 4.3.1 to produce an environment to those observed within patients. These vessels are assigned a secretion rate of cisplatin equal to the dosage of drug assumed to be administered. Figure 4.29 shows an example cross-section of the cisplatin concentration during a simulation, with high cisplatin densities observed in close proximity to where vessels pass through.

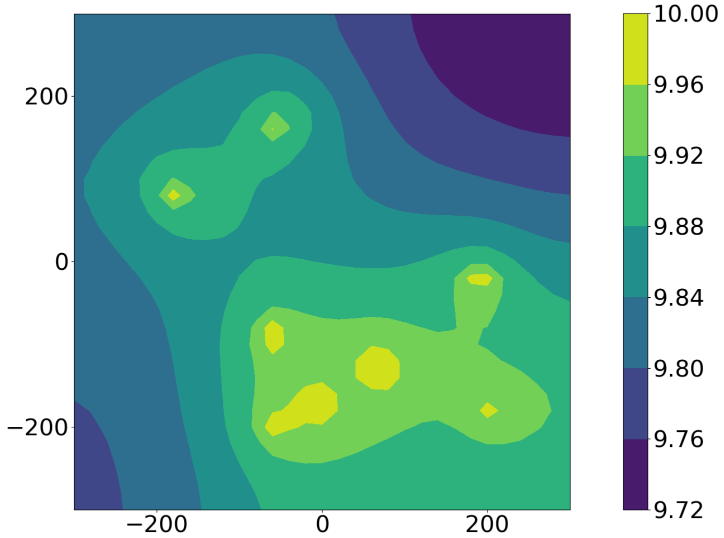

FIGURE 4.29: **Cross-section of cisplatin concentrations after vessel secretion**. Concentrations of cisplatin are tracked across the domain with a treatment dosage of 10mg. High concentrations (yellow) are located around vessels, with low concentrations (purple) found elsewhere.

4.3.1 Initialisation

Vessels are assumed to be spaced around 100-200 nanometres apart from each other [109], leading to nine vessels being initialised inside a 620 × 620 nanometre domain. This is done using an algorithm prior to placing the tumour into the domain. A vessel cell is placed along the bottom of the spatial domain, with a centre at z co-ordinate set to be $z = r - 310$, where r is the blood vessel cell radius to allow for the entire cell to be contained in the domain. The x and y co-ordinates are taken from a uniform distribution, each with a minimum of $r - 310$ and maximum of $310 - r$. After this cell has been placed, polar coordinates are used to select a random point on a hemisphere, sharing the same center as the cell and surrounding the cell in the positive z direction, with a radius of $2r$ as shown in Figure 4.30 (A). After selecting a point on this hemisphere, a new vessel cell is placed with this point as its centre. This process is then repeated with the new vessel cell, and so on. This generates a chain of cells, each with a larger z coordinate than the last to ensure the vessel works upwards with each vessel cell centre $2r$ away from its neighbours. When the algorithm attempts to place a cell within r distance of a x, y, or z boundary, the vessel is assumed to have left the domain and the chain for that vessel is ended. At this point, a new vessel is made by placing a new cell along the bottom of the domain and repeating the entire process. This is repeated until the correct number of vessel cells are present, with an example domain shown in Figure 4.30 (B).

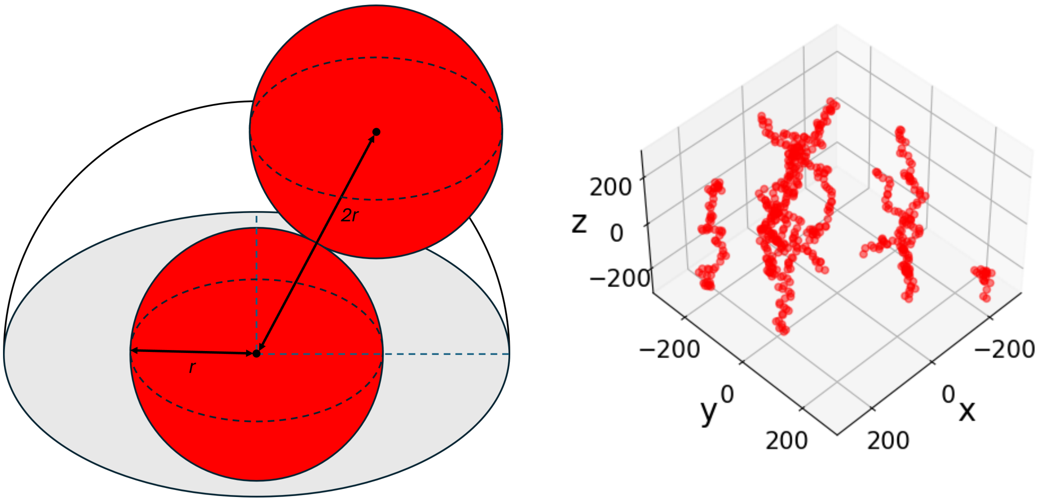

(A) The process in which chains of vessel cells are created for the simulation.

(B) The domain layour prior to the placement of the spheroid, with nine vessels initialised randomly.

FIGURE 4.30: **The vessel formation process.** Vessels form by creating a chain of cells with touching surfaces (A). This leads to the vessels working up through the domain until they make contact with a domain boundary, at which point the next vessel chain is made until termination (B).

Spheroids are composed of 400 cells initialised within a ball of radius of 50 nanometres in the centre of the domain. Tumours are composed of either 25%, 50%, or 75% susceptible (wild type) cells , with the remained made up of cisplatin resistant cells.

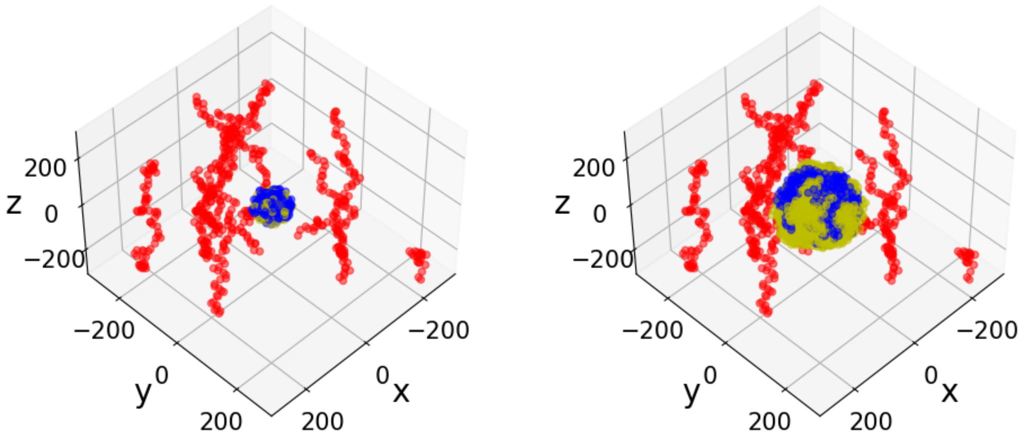

(A) 0 hours

(B) 24 hours

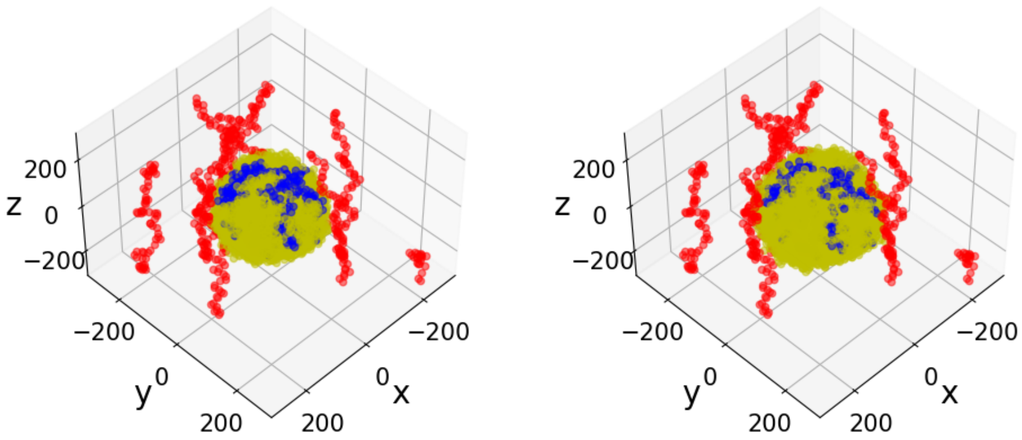

(C) 48 hours

(D) 72 hours

FIGURE 4.31: **An example 3D simulation for heterogeneous SKOV-3 tumours** Tumours above are initialised with 300 sensitive cells (blue) and 100 resistant cells (yellow) with nine blood vessels (red). Snapshots of the 3D domain are recorded every 24 hours, showing the progression of the tumour due to the growth of resistant cells.

Dosages of 10mg and 75mg are tested to investigate treatment levels previously unexplored. The blood vessels begin secreting the drug after six minutes of simulated time to represent the short delay between treatment administration and effect. Once this begins, vessels secrete cisplatin continuously at the same rate for the remainder of the simulation. Figure 4.31 shows an example of a simulation for

SKOV-3 tumours initialised with 75% susceptible cells with a drug dosage of 10mg, in which red blood vessels surround a tumour composed of susceptible cells (blue) and resistant cells (yellow).

4.3.2 Impact of Initial Conditions

Population dynamics are tracked over three days to produce results of the same time scale as those used in the calibration and validation. Simulation data is taken every hour, recording the live cell populations for susceptible and resistant cells.

Resistant cells remain the dominant population in SKOV-3 tumours regardless of treatment level or initial tumour composition. A dosage of 10mg, shown in the top row of Figure 4.32 appears insufficient in reducing the tumour size, with simulated populations of resistant cells increasing monotonically. At the higher dosage of 75mg, shown in the bottom row of Figure 4.32, the treatment is able to generate a small, temporary reduction in the resistant population. However, again this is insufficient in eradicating the tumour population, with recovery appearing to begin towards the end of the simulation.

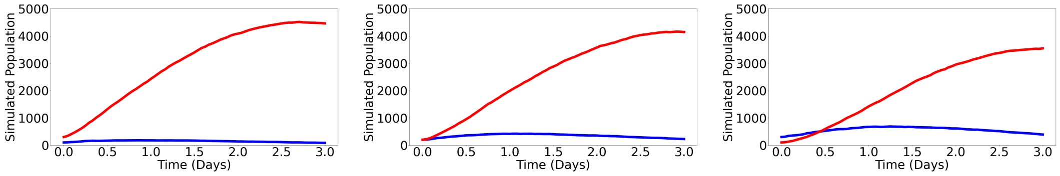

(A) 25% susceptible (B) 50% susceptible (C) 75% susceptible

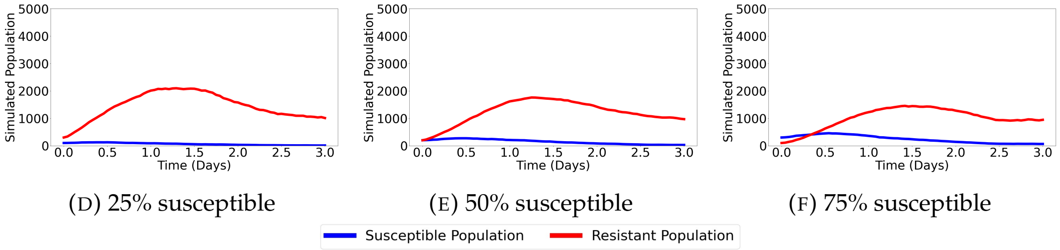

(D) 25% susceptible (E) 50% susceptible (F) 75% susceptible

FIGURE 4.32: **SKOV-3 tumours with varying initial compositions.** Populations are made up of 25% (left), 50% (middle), and 75% (right) wild type cells, with the remainer of the populations made up of cisplatin resistant cells. Tumours are then given a dosage of 10mg (top) and 75mg (bottom) cisplatin, with live cell populations recorded every hour.

Similar to that seen in the SKOV-3 simulations, resistant cells prevail throughout the simulations. Initially, susceptible cells are able to proliferate before the drug can induce sufficient cell damage to reduce the population. This occurs after around one day for 10mg, as shown in the top row of Figure 4.33 and around half a day for 75mg, as shown in the bottom row of Figure 4.33.

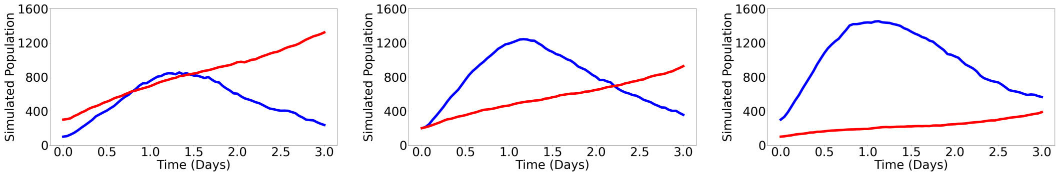

(A) 25% susceptible (B) 50% susceptible (C) 75% susceptible

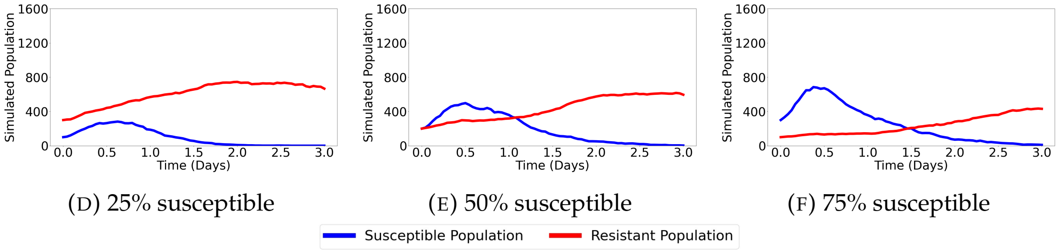

(D) 25% susceptible (E) 50% susceptible (F) 75% susceptible

FIGURE 4.33: **OVCAR-3 tumours with varying initial compositions.** Populations are made up of 25% (left), 50% (middle), and 75% (right) wild type cells, with the remainer of the populations made up of cisplatin resistant cells. Tumours are then given a dosage of 10mg (top) and 75mg (bottom) cisplatin, with live cell populations recorded every hour.

4.4 Discussion

The effects of cisplatin have been shown to play a critical role in the inhibition of cancer tumour progression. Tumours which would naturally grow otherwise exponentially appear to be somewhat controllable provided that certain treatment protocols are fulfilled. The model discussed in this chapter captures this phenomenon, with higher dosages generally leading to an increased reduction in cancer tumour growth, as observed in the *in vitro* experiments. Initially, a very good fit was made in most cases between the model output and the experimental data when parameters were optimised for each individual dosage separately. Calibrating these results to the relevant Emax and linear curves showed a good fit to the validation data for the four cell lines. This validation provided confidence when using the model to make predictions in Section 4.3 beyond those tested experimentally. Adapting the domain settings to contain drug-secreting vessels gave a more insightful prediction regarding how cisplatin may impact tumour growth inside a human body, showing the diffusion of the drug from the blood vessels following intravenous administration.

This chapter introduced the first quantitative data exploring the difference between drug sensitive and drug resistant tumours used in this study. By fitting unique parameter values for each cell line, predictions can be made about the tumour growth depending on the initial composition. Resistant cells were found to be effected less by exposure to cisplatin, allowing them to remain during the course of the simulations regardless of the treatment dosage. The removal of sensitive cells in turn provides more space for resistant cells to proliferate into, removing the contact inhibition there may have previously been. This reaffirms the "less is more" approach which is now being taken to many cancer treatments for patients, in which using lower dosages allows the susceptible cells to remain and prevent the tumour becoming predominantly drug resistant.

To explore this idea further, adaptations could be made to the administration of the drug. Currently, cisplatin is assumed to be administered as soon as the simulation starts with vessels secreting the drug with minimal delay and continues to do so until the terminations of the simulation. An approach that may be more relevant is to explore intermittent treatment, such as treatment periods followed by holiday periods. This is common practice during chemotherapy due to the toxicity and practicality of administering treatment. Another addition to the model could be to introduce a possible switch of cells from susceptible to resistant. Susceptible cells which withstand cisplatin exposure for prolonged periods of time may develop properties allowing them to transform into resistant cells, further adding to the resistant cell population. Obtaining biologically realistic rates for this switch would be essential to ensure results remained reasonable.

After exploring the quantitative impact of cisplatin on tumours, the chapter highlights the significant effect that chemotherapeutic treatments can have. It is therefore essential that patients are provided with the optimal protocols given the associated drawbacks with higher dosages. Mathematical models can have a key role in finding these treatment plans and helping to improve the survival rates for cancer patients.

Chapter 5

Conclusions

5.1 Conclusions

In this study, we have developed multiple mathematical models to study the progression of ovarian cancer using a range of various approaches. A relatively simple model was initially introduced to obtain preliminary results and gain an understanding of what may be expected following the development of more detailed models later in the study.

Firstly, an investigation of the effects of adipocyte exposure on OVCAR-3 and SKOV-3 cell lines was performed in Chapter 2. Observations of biological experiments, along with an extensive literature review provided a basis for the rules to incorporate into the initial model. The model included the effects on the cell cycle of the adipose derived media concentration in the microenvironment. The two cell lines were found to possess contrasting phenotypic changes when tumours were placed in the presence of adipose tissue, with OVCAR-3 cycling rates decreasing while SKOV-3 cycling rates increased. The model introduced the idea of the bystander effect for EMT in cancer cells. The process of mesenchymal cells secreting a chemical encouraging EMT with low diffusion into the microenvironment generated the red polka dot effect observed in OVCAR-3 tumours and the internal mesenchymal pool seen in SKOV-3 tumours. This effect remained present throughout the study and is critical in producing the tumour layouts observed *in vitro*. The qualitative results found *in vitro* were captured well by the model in Chapter 2, with tumour cell population sizes and compositions in general agreement. This allowed us to make confident predictions regarding the effects of the conditions on the tumour growth, such as the adipose media concentration, treatment dosage, and initial tumour size. Spatio-temporal dynamics were tracked and recorded along with tumour cross-sections for each simulation to help make direct comparisons across the different conditions.

Chapter 3 directed attention away from the role of adipocytes, and assumed adipose derived media was present throughout the simulations. The focus of this chapter turned to the impact that EMT had on tumour progression. The process of EMT was implemented with more detail, with the resulting phenotypic changes incorporated into the cells. Mesenchymal cells were assigned higher migration speeds and lower adhesion strengths than epithelial cells to capture the dynamics observed biologically. A carrying capacity was incorporated into the cycling rate equation in this chapter, as comparisons between the *in silico* simulation and *in vitro* experiment results were made for cells with a maximum occupancy. The current cadherin rating in the cells, as well as the concentration levels of oxygen and bystander signal in the microenvironment were all incorporated into the generation of a probability that a cell moved up the discrete EMT scale, with different weightings assigned for each cell line. The reverse process of EMT, MET, was introduced to allow mesenchymal cells to revert back to a more epithelial phenotype, as seen in post metastatic tumours. The results of different initial conditions were investigated, with tumours initialised with epithelial, mesenchymal, and a third "hybrid" cell type. The temporal dynamics were studied and compared with results found in a prostate cancer cell line, with similar quantitative results found in OVCAR-3 tumours. Sensitivity analysis was performed to investigate the responsiveness of the tumour population size and composition to the parameters involved in the cell cycling and EMT probability equations, where all tested parameters showed occasions of at least moderate impacts on the results.

Data obtained by biological experiments was used to generate a model tailored towards the impact of cisplatin in Chapter 4. The model incorporated a slight variation in the cell cycling rate equation and used a dynamic death rate dependent on the drug concentration. A damage variable, accumulated by prolonged exposure to high concentrations of cisplatin, alongside the current concentration of cisplatin a cell was placed in, were combined to approximate an apoptosis rate variable assigned to each cell individually. Parameter optimisation using the *in vitro* data was performed to quantify how the cisplatin concentration in the microenvironment and damage variable associated with each cell affect this apoptosis rate. By working consecutively through the different dosages for each cell line, optimised linear and Emax functions were built up for drug impact and damage impact parameters. Values were extracted from these functions and tested against validation data obtained through additional *in vitro* experiments to ensure the model provided accurate predictions. SKOV-3 cell lines generally showed a close fit between the model predictions and the validation data, with OVCAR-3 cell lines losing predictive ability at higher dosages. Following model validation, predictions were made to give insights into what may be expected in an *in vivo* setting. Tumours made up of various compositions of wild type and cisplatin resistant cell types were initialised in the domain along with surrounding blood vessels to supply the cisplatin. This helped to provide predictions more relevant to the real life situation of a patient, in which drugs are administered and diffuse throughout the tumour from a blood vessel source.

The overall aim of the project was to produce models capable of capturing the dynamics in various ovarian cancer tumours. With a large difference in tumour characteristics observed from cell line to cell line, the models required cell line specificity to ensure relevant results were produced. Different aspects of the microenvironment, tumour composition, and treatment protocol were explored to provide a detailed overview of ovarian cancer progression, highlighting the need for further research into the disease.

5.2 Future Work

The work done in this study opens up many possibilities for future research paths. Each model developed in this study omits various biological details that could be included to make the model more complex and closer to an *in vivo* setting. Different substrates in the microenvironment can have important roles to play in cancer progression, with only the key substrates included in the models developed in this study. Alongside substrates, other components in the microenvironment such as fibroblasts, macrophages, and adipose derived exosomes can have an key impact on the progression of ovarian cancer. Extracellular vesicles such as exosomes are small agents that can transfer information between cells, altering their behaviour and phenotype. The impact of including these adipose derived exosomes into simulations could be explored in future adaptations of the models described above to make more in depth investigations.

In Chapter 2, we investigated the role of adipocytes and the adipose tissue in tumour progression. Throughout the chapter, the adipose derived media was assumed to follow simple decay/uptake rules with a minimal effect on the temporal substrate dynamics. Further insights could be inferred if the domain boundaries had flux conditions that changed with time. This could represent a patient losing or gaining weight, affecting the proliferation and composition of the tumour. This would allow for predictions to be made on the impact that dieting for certain periods could have on tumour regression over the course of weeks or months. It could also incorporate the effects of cachexia, potentially by introducing a large decrease in adipose derived media when the tumour fulfils certain criteria.

Chapter 3 focused more heavily on the mechanisms of EMT and capturing the dynamics observed across various cell lines. While SKOV-3 tumours displayed a shell of epithelial cells around a mesenchymal core, OVCAR-3 tumours generated small clumps of mesenchymal cells within a region of epithelial cells. One hypothesis is that these clusters of mesenchymal OVCAR-3 cells can collectively exit the tumour and migrate away, ultimately relocating elsewhere in the body and completing metastasis [219]. Currently, the model incorporates a low adhesion force for mesenchymal cells, preventing the capability of these clusters from collectively escaping the tumour. Future adaptations could incorporate the occurrence of this event, providing a prediction of when metastasis may happen and if this can be prevented.

Possible treatment protocols provided to patients were modelled in Chapter 4. Following parameter optimisation, tumours were placed in a domain along with a network of vessels. These vessels were set to secrete a constant supply of cisplatin into the microenvironment after commencing treatment. This is not usually possible due to the side effects the patient is likely to experience under constant chemotherapy. The simulations may therefore be more biologically relevant if the treatments were given in intervals, implemented by dynamic secretion rates. This can imitate intermittent chemotherapy, where treatment is provided to a patient between periods of recovery. This is a popular method of cancer treatment, allowing the body to recuperate between the administrations. Results in this case may be more representative of the plausible treatment protocols for patients.

With ovarian cancer affecting so many women each year, further research into the possible treatments is essential. The continuation of drug development alongside the presence of multidisciplinary tools will ideally help improve the poor current prognosis, improving the lives of the current and future generations of ovarian cancer patients.

Bibliography

[1] M Adams et al. “A comparison of the toxicity and efficacy of cisplatin and carboplatin in advanced ovarian cancer”. In: *Acta Oncologica* 28.1 (1989), pp. 57–60.

[2] Waleed K Ahmed. “Advantages and disadvantages of using MATLAB/ode45 for solving differential equations in engineering applications”. In: *International Journal of Engineering* 7.1 (2013), pp. 25–31.

[3] Pamela Akuwudike et al. “Impact of fractionated cisplatin and radiation treatment on cell growth and accumulation of DNA damage in two normal cell types differing in origin”. In: *Scientific Reports* 13.1 (2023), p. 14891.

[4] Sara Al Habyan et al. “Multicellular detachment generates metastatic spheroids during intra-abdominal dissemination in epithelial ovarian cancer”. In: *Oncogene* 37.37 (2018), pp. 5127–5135.

[5] N Arias et al. “MicroRNAs involved in the browning process of adipocytes”. In: *Journal of physiology and biochemistry* 72.3 (2016), pp. 509–521.

[6] Melina Arnold et al. “Obesity and cancer: an update of the global impact”. In: *Cancer epidemiology* 41 (2016), pp. 8–15.

[7] J Bachmann et al. “Predictive mathematical models of cancer signalling pathways”. In: *Journal of internal medicine* 271.2 (2012), pp. 155–165.

[8] Rajiv Baijal and Rakesh K Tandon. “Effect of lactase on symptoms and hydrogen breath levels in lactose intolerance: A crossover placebo-controlled study”. In: *JGH Open* 5.1 (2021), pp. 143–148.

[9] Basil Bakir et al. “EMT, MET, plasticity, and tumor metastasis”. In: *Trends in cell biology* 30.10 (2020), pp. 764–776.

[10] Kangbo Bao. “An elementary mathematical modeling of drug resistance in cancer”. In: *Mathematical Biosciences and Engineering* 18.1 (2021), pp. 339–353.

[11] Alexis R Barr et al. “DNA damage during S-phase mediates the proliferation-quiescence decision in the subsequent G1 via p21 expression”. In: *Nature communications* 8.1 (2017), p. 14728.

[12] Alexander Bartelt and Joerg Heeren. "Adipose tissue browning and metabolic health". In: *Nature Reviews Endocrinology* 10.1 (2014), pp. 24–36.

[13] Joseph S Baxter et al. "Resistance to DNA repair inhibitors in cancer". In: *Molecular Oncology* 16.21 (2022), pp. 3811–3827.

[14] Sophia Belkhir, Frederic Thomas, and Benjamin Roche. "Darwinian approaches for cancer treatment: benefits of mathematical modeling". In: *Cancers* 13.17 (2021), p. 4448.

[15] George P Biro. "Oxygen and ATP: the Energy Economy of the Cell". In: *Blood substitutes and oxygen biotherapeutics*. Springer, 2022, pp. 21–32.

[16] Philippe Bourin et al. "Stromal cells from the adipose tissue-derived stromal vascular fraction and culture expanded adipose tissue-derived stromal/stem cells: a joint statement of the International Federation for Adipose Therapeutics and Science (IFATS) and the International Society for Cellular Therapy (ISCT)". In: *Cytotherapy* 15.6 (2013), pp. 641–648.

[17] Julie R Brahmer et al. "Five-year survival outcomes with nivolumab plus ipilimumab versus chemotherapy as first-line treatment for metastatic non–small-cell lung cancer in CheckMate 227". In: *Journal of Clinical Oncology* 41.6 (2023), pp. 1200–1212.

[18] Freddie Bray et al. "Global cancer statistics 2022: GLOBOCAN estimates of incidence and mortality worldwide for 36 cancers in 185 countries". In: *CA: a cancer journal for clinicians* 74.3 (2024), pp. 229–263.

[19] CA Brohem et al. "Comparison between fibroblasts and mesenchymal stem cells derived from dermal and adipose tissue". In: *International journal of cosmetic science* 35.5 (2013), pp. 448–457.

[20] Ronald B Brown. "Obesity and cancer: potential mediation by dysregulated dietary phosphate". In: *Obesities* 2.1 (2022), pp. 64–75.

[21] Anamaria Brozovic et al. "The miR-200 family differentially regulates sensitivity to paclitaxel and carboplatin in human ovarian carcinoma OVCAR-3 and MES-OV cells". In: *Molecular oncology* 9.8 (2015), pp. 1678–1693.

[22] Karen M Bussard et al. "Tumor-associated stromal cells as key contributors to the tumor microenvironment". In: *Breast Cancer Research* 18.1 (2016), pp. 1–11.

[23] B Cannon et al. "Perinatal activation of brown adipose tissue". In: *The Endocrine Control of the fetus*. Springer, 1988, pp. 306–320.

[24] Maomao Cao et al. “Current cancer burden in China: epidemiology, etiology, and prevention”. In: *Cancer biology & medicine* 19.8 (2022), pp. 1121–1138.

[25] Sonia Capellero et al. “Ovarian cancer cells in ascites form aggregates that display a hybrid epithelial-mesenchymal phenotype and allows survival and proliferation of metastasizing cells”. In: *International Journal of Molecular Sciences* 23.2 (2022), p. 833.

[26] Roberto A Ku-Carrillo, Sandra E Delgadillo, and BM Chen-Charpentier. “A mathematical model for the effect of obesity on cancer growth and on the immune system response”. In: *Applied Mathematical Modelling* 40.7-8 (2016), pp. 4908–4920.

[27] Roberto A Ku-Carrillo, Sandra E Delgadillo-Aleman, and Benito M Chen-Charpentier. “Effects of the obesity on optimal control schedules of chemotherapy on a cancerous tumor”. In: *Journal of Computational and Applied Mathematics* 309 (2017), pp. 603–610.

[28] Brett W Carter and William G Schucany. “Brown adipose tissue in a newborn, Baylor University Medical Center Proceedings”. In: *Baylor University Medical Center Proceedings*. Vol. 21. 3. Taylor & Francis. 2008, pp. 328–330.

[29] Marielena Gamboa Castro, Susan E Leggett, and Ian Y Wong. “Clustering and jamming in epithelial–mesenchymal co-cultures”. In: *Soft Matter* 12.40 (2016), pp. 8327–8337.

[30] Christine L Chaffer and Robert A Weinberg. “A perspective on cancer cell metastasis”. In: *science* 331.6024 (2011), pp. 1559–1564.

[31] Christine L Chaffer et al. “EMT, cell plasticity and metastasis”. In: *Cancer and Metastasis Reviews* 35 (2016), pp. 645–654.

[32] Ashwin Chandra et al. “Ovarian cancer: Current status and strategies for improving therapeutic outcomes”. In: *Cancer medicine* 8.16 (2019), pp. 7018–7031.

[33] Da-Chung Chen et al. “Serum adiponectin and leptin levels in Taiwanese breast cancer patients”. In: *Cancer letters* 237.1 (2006), pp. 109–114.

[34] Hsin-Fu Chen et al. “Surface marker epithelial cell adhesion molecule and E-cadherin facilitate the identification and selection of induced pluripotent stem cells”. In: *Stem Cell Reviews and Reports* 7 (2011), pp. 722–735.

[35] Shih-Yao Chen. “Does epithelial-mesenchymal transition happen in rheumatoid joints?” In: *European journal of rheumatology* 1.2 (2014), p. 86.

[36] Shuo Chen et al. “Conversion of epithelial-to-mesenchymal transition to mesenchymal-to-epithelial transition is mediated by oxygen concentration in pancreatic cancer cells Retraction in/10.3892/ol. 2022.13227”. In: *Oncology letters* 15.5 (2018), pp. 7144–7152.

[37] Tong Chen et al. “Epithelial–mesenchymal transition (EMT): A biological process in the development, stem cell differentiation, and tumorigenesis”. In: *Journal of cellular physiology* 232.12 (2017), pp. 3261–3272.

[38] Shaomei Cheng et al. “The essential roles of CCR7 in epithelial-to-mesenchymal transition induced by hypoxia in epithelial ovarian carcinomas”. In: *Tumor Biology* 35 (2014), pp. 12293–12298.

[39] Cheen Fei Chin and Foong May Yeong. “Safeguarding entry into mitosis: the antephase checkpoint”. In: *Molecular and cellular biology* 30.1 (2010), pp. 22–32.

[40] Yu-Tang Chin et al. “Leptin OB3 peptide suppresses leptin-induced signaling and progression in ovarian cancer cells”. In: *Journal of Biomedical Science* 24 (2017), pp. 1–13.

[41] Laurent Claret et al. “Model-based prediction of phase III overall survival in colorectal cancer on the basis of phase II tumor dynamics”. In: *Journal of Clinical Oncology* 27.25 (2009), pp. 4103–4108.

[42] Geoffrey M Cooper. “The Eukaryotic Cell Cycle”. In: *National Library of Medicine* (2000). URL: `https://www.ncbi.nlm.nih.gov/books/NBK9876/`.

[43] Tristan I Croll et al. “Modelling oxygen diffusion and cell growth in a porous, vascularising scaffold for soft tissue engineering applications”. In: *Chemical Engineering Science* 60.17 (2005), pp. 4924–4934.

[44] Elisa Dalla Pozza et al. “Secreted molecules inducing epithelial-to-mesenchymal transition in cancer development”. In: *Seminars in cell & developmental biology*. Vol. 78. Elsevier. 2018, pp. 62–72.

[45] Christine P Dancey and John Reidy. *Statistics without maths for psychology*. Pearson education, 2007.

[46] Suman K Das et al. “Adipose triglyceride lipase contributes to cancer-associated cachexia”. In: *Science* 333.6039 (2011), pp. 233–238.

[47] Ben Davidson, Claes G Trope, and Reuven Reich. “The role of the tumor stroma in ovarian cancer”. In: *Frontiers in oncology* 4 (2014), p. 104.

[48] Felicity M Davis et al. “Targeting EMT in cancer: opportunities for pharmacological intervention”. In: *Trends in pharmacological sciences* 35.9 (2014), pp. 479–488.

[49] Lisette G De Pillis and Ami Radunskaya. “The dynamics of an optimally controlled tumor model: A case study”. In: *Mathematical and computer modelling* 37.11 (2003), pp. 1221–1244.

[50] Kaushik Dehingia, Hemanta K Sarmah, and Mdi Begum Jeelani. “A brief review on cancer research and its treatment through mathematical modelling”. In: *Ann Cancer Res Ther* 29.1 (2021), pp. 34–40.

[51] Marios Demetriades et al. “Interrogating and quantifying in vitro cancer drug pharmacodynamics via agent-based and bayesian monte carlo modelling”. In: *Pharmaceutics* 14.4 (2022), p. 749.

[52] Mahalia S Desruisseaux et al. “Adipocyte, adipose tissue, and infectious disease”. In: *Infection and immunity* 75.3 (2007), pp. 1066–1078.

[53] Prashant Dogra et al. “Mathematical modeling in cancer nanomedicine: a review”. In: *Biomedical microdevices* 21 (2019), pp. 1–23.

[54] Claire L Donohoe et al. “Emerging concepts linking obesity with the hallmarks of cancer”. In: *Trends in endocrinology & metabolism* 28.1 (2017), pp. 46–62.

[55] Esther Dos Santos et al. “The roles of leptin and adiponectin at the fetal-maternal interface in humans”. In: *Hormone molecular biology and clinical investigation* 24.1 (2015), pp. 47–63.

[56] Bowen Du and Joong Sup Shim. “Targeting epithelial–mesenchymal transition (EMT) to overcome drug resistance in cancer”. In: *Molecules* 21.7 (2016), p. 965.

[57] Hongying Du et al. “Prediction of inhibitory activity of epidermal growth factor receptor inhibitors using grid search-projection pursuit regression method”. In: *PLoS One* 6.7 (2011), e22367.

[58] Jing Du et al. “Hypoxia promotes vasculogenic mimicry formation by inducing epithelial–mesenchymal transition in ovarian carcinoma”. In: *Gynecologic oncology* 133.3 (2014), pp. 575–583.

[59] Pernilla Eliasson et al. “Hypoxia mediates low cell-cycle activity and increases the proportion of long-term–reconstituting hematopoietic stem cells during in vitro culture”. In: *Experimental hematology* 38.4 (2010), pp. 301–310.

[60] Sivan Elloul et al. “Mesenchymal-to-epithelial transition determinants as characteristics of ovarian carcinoma effusions”. In: *Clinical & experimental metastasis* 27 (2010), pp. 161–172.

[61] Joema Felipe Lima et al. “EMT in breast carcinoma—a review”. In: *Journal of clinical medicine* 5.7 (2016), p. 65.

[62] Anna Fiedler et al. "Tailored parameter optimization methods for ordinary differential equation models with steady-state constraints". In: *BMC systems biology* 10 (2016), pp. 1–19.

[63] Toren Finkel and Paul M Hwang. "The Krebs cycle meets the cell cycle: Mitochondria and the G1–S transition". In: *Proceedings of the National Academy of Sciences* 106.29 (2009), pp. 11825–11826.

[64] Michael J Flynn and Jonathan A Ledermann. "Ovarian cancer recurrence: is the definition of platinum resistance modified by PARPi and other intervening treatments? The evolving landscape in the management of platinum-resistant ovarian cancer". In: *Cancer Drug Resistance* 5.2 (2022), p. 424.

[65] Walfre Franco et al. "Hyperthermic injury to adipocyte cells by selective heating of subcutaneous fat with a novel radiofrequency device: feasibility studies". In: *Lasers in surgery and medicine* 42.5 (2010), pp. 361–370.

[66] Linnea C Franssen and Mark AJ Chaplain. "A mathematical multi-organ model for bidirectional epithelial–mesenchymal transitions in the metastatic spread of cancer". In: *IMA Journal of Applied Mathematics* 85.5 (2020), pp. 724–761.

[67] Christine Frithioff-Bøjsøe et al. "Leptin, adiponectin, and their ratio as markers of insulin resistance and cardiometabolic risk in childhood obesity". In: *Pediatric diabetes* 21.2 (2020), pp. 194–202.

[68] Andrea Frontini and Saverio Cinti. "Distribution and development of brown adipocytes in the murine and human adipose organ". In: *Cell metabolism* 11.4 (2010), pp. 253–256.

[69] Sandra Galic, Jon S Oakhill, and Gregory R Steinberg. "Adipose tissue as an endocrine organ". In: *Molecular and cellular endocrinology* 316.2 (2010), pp. 129–139.

[70] Dingcheng Gao et al. "Microenvironmental regulation of epithelial–mesenchymal transitions in cancer". In: *Cancer research* 72.19 (2012), pp. 4883–4889.

[71] Claude Gérard and Albert Goldbeter. "The balance between cell cycle arrest and cell proliferation: control by the extracellular matrix and by contact inhibition". In: *Interface focus* 4.3 (2014), p. 20130075.

[72] Ahmadreza Ghaffarizadeh, Samuel H Friedman, and Paul Macklin. "BioFVM: an efficient, parallelized diffusive transport solver for 3-D biological simulations". In: *Bioinformatics* 32.8 (2016), pp. 1256–1258.

[73] Ahmadreza Ghaffarizadeh et al. “PhysiCell: An open source physics-based cell simulator for 3-D multicellular systems”. In: *PLoS computational biology* 14.2 (2018), e1005991.

[74] Sumit Ghosh. “Cisplatin: The first metal based anticancer drug”. In: *Bioorganic chemistry* 88 (2019), p. 102925.

[75] Marta Giralt and Francesc Villarroya. “White, brown, beige/brite: different adipose cells for different functions?” In: *Endocrinology* 154.9 (2013), pp. 2992–3000.

[76] Victor M Gonzalez et al. “Is cisplatin-induced cell death always produced by apoptosis?” In: *Molecular pharmacology* 59.4 (2001), pp. 657–663.

[77] Michael M Gottesman et al. “Toward a better understanding of the complexity of cancer drug resistance”. In: *Annual review of pharmacology and toxicology* 56 (2016), pp. 85–102.

[78] Mariana Lopes Grassi et al. “Proteomic analysis of ovarian cancer cells during epithelial-mesenchymal transition (EMT) induced by epidermal growth factor (EGF) reveals mechanisms of cell cycle control”. In: *Journal of proteomics* 151 (2017), pp. 2–11.

[79] David Robert Grimes, Alexander G Fletcher, and Mike Partridge. “Oxygen consumption dynamics in steady-state tumour models”. In: *Royal Society open science* 1.1 (2014), p. 140080.

[80] Xiangming Guan. “Cancer metastases: challenges and opportunities”. In: *Acta pharmaceutica sinica B* 5.5 (2015), pp. 402–418.

[81] JP Guastalla Iii and V Dieras. “The taxanes: toxicity and quality of life considerations in advanced ovarian cancer”. In: *British journal of cancer* 89.3 (2003), S16–S22.

[82] NPA Devika Gunasinghe et al. “Mesenchymal–epithelial transition (MET) as a mechanism for metastatic colonisation in breast cancer”. In: *Cancer and Metastasis Reviews* 31 (2012), pp. 469–478.

[83] Jef Haerinck and Geert Berx. “Partial EMT takes the lead in cancer metastasis”. In: *Developmental Cell* 56.23 (2021), pp. 3174–3176.

[84] Sara Hamis, Stanislav Stratiev, and Gibin G Powathil. “Uncertainty and sensitivity analyses methods for agent-based mathematical models: An introductory review”. In: *The Physics of Cancer: Research Advances* (2021), pp. 1–37.

[85] Sara Hamis et al. "Targeting cellular DNA damage responses in cancer: an in vitro-calibrated agent-based model simulating monolayer and spheroid treatment responses to ATR-inhibiting drugs". In: *Bulletin of Mathematical Biology* 83.10 (2021), p. 103.

[86] Innocence Harvey, Anik Boudreau, and Jacqueline M Stephens. "Adipose tissue in health and disease". In: *Advances in Surgical and Medical Specialties* (2023), pp. 1281–1306.

[87] Waqar Ul Hassan, Udo Greiser, and Wenxin Wang. "Role of adipose-derived stem cells in wound healing". In: *Wound repair and regeneration* 22.3 (2014), pp. 313–325.

[88] MG Hayward and WR Keatinge. "Roles of subcutaneous fat and thermoregulatory reflexes in determining ability to stabilize body temperature in water." In: *The Journal of physiology* 320.1 (1981), pp. 229–251.

[89] Peng He, Kang Qiu, and Ya Jia. "Modeling of mesenchymal hybrid epithelial state and phenotypic transitions in EMT and MET processes of cancer cells". In: *Scientific Reports* 8.1 (2018), p. 14323.

[90] Staffan Hildebrand, Jasmin Stümer, and Alexander Pfeifer. "PVAT and its relation to brown, beige, and white adipose tissue in development and function". In: *Frontiers in Physiology* 9 (2018), p. 70.

[91] Yong-Feng Hou et al. "1α, 25 (OH) 2D3 suppresses the migration of ovarian cancer SKOV-3 cells through the inhibition of epithelial–mesenchymal transition". In: *International Journal of Molecular Sciences* 17.8 (2016), p. 1285.

[92] Jian-Xiong Hu et al. "Pancreatic cancer: A review of epidemiology, trend, and risk factors". In: *World journal of gastroenterology* 27.27 (2021), p. 4298.

[93] Zhe Huang and Aimin Xu. "Adipose extracellular vesicles in intercellular and inter-organ crosstalk in metabolic health and diseases". In: *Frontiers in immunology* 12 (2021), p. 608680.

[94] Honor Hugo et al. "Epithelial—mesenchymal and mesenchymal—epithelial transitions in carcinoma progression". In: *Journal of cellular physiology* 213.2 (2007), pp. 374–383.

[95] Kenji Ikeda, Pema Maretich, and Shingo Kajimura. "The common and distinct features of brown and beige adipocytes". In: *Trends in Endocrinology & Metabolism* 29.3 (2018), pp. 191–200.

[96] Neda Jabbari, Ashley N Reavis, and John F McDonald. "Sequence variation among members of the miR-200 microRNA family is correlated with variation in the ability to induce hallmarks of mesenchymal-epithelial transition in ovarian cancer cells". In: *Journal of ovarian research* 7.1 (2014), pp. 1–9.

[97] Ammar Jalalimanesh et al. "Simulation-based optimization of radiotherapy: Agent-based modeling and reinforcement learning". In: *Mathematics and Computers in Simulation* 133 (2017), pp. 235–248.

[98] Elizabeth R Jamieson and Stephen J Lippard. "Structure, recognition, and processing of cisplatin- DNA adducts". In: *Chemical reviews* 99.9 (1999), pp. 2467–2498.

[99] Thierry Jardé et al. "Involvement of adiponectin and leptin in breast cancer: clinical and in vitro studies". In: *Endocrine-related cancer* 16.4 (2009), pp. 1197–1210.

[100] Devaraj Jayachandran et al. "Model-based individualized treatment of chemotherapeutics: Bayesian population modeling and dose optimization". In: *PloS one* 10.7 (2015), e0133244.

[101] Gordon C Jayson et al. "Ovarian cancer". In: *The Lancet* 384.9951 (2014), pp. 1376–1388.

[102] Jian Jiang, Ya-ling Tang, and Xin-hua Liang. "EMT: a new vision of hypoxia promoting cancer progression". In: *Cancer biology & therapy* 11.8 (2011), pp. 714–723.

[103] Jingwen Jiang et al. "Exosomes regulate the epithelial–mesenchymal transition in cancer". In: *Frontiers in Oncology* 12 (2022), p. 864980.

[104] Jeanette AI Johnson et al. "Human interpretable grammar encodes multicellular systems biology models to democratize virtual cell laboratories". In: *Cell* 188.17 (2025), pp. 4711–4733.

[105] Mohit Kumar Jolly and Toni Celià-Terrassa. "Dynamics of phenotypic heterogeneity associated with EMT and stemness during cancer progression". In: *Journal of clinical medicine* 8.10 (2019), p. 1542.

[106] Mohit Kumar Jolly et al. "EMT and MET: necessary or permissive for metastasis?" In: *Molecular oncology* 11.7 (2017), pp. 755–769.

[107] Mohit Kumar Jolly et al. "Epithelial/mesenchymal plasticity: how have quantitative mathematical models helped improve our understanding?" In: *Molecular Oncology* 11.7 (2017), pp. 739–754.

[108] Mohit Kumar Jolly et al. "Stability of the hybrid epithelial/mesenchymal phenotype". In: *Oncotarget* 7.19 (2016), p. 27067.

[109] Alexander Jönsson et al. "Tissue Like Density Sheets of Hepatoblastoma Cultures Obtained with Thin Suspended Hydrogels Mimicking In Vivo Inter-Capillary Distances". In: *Advanced Materials Technologies* 10.7 (2025), p. 2401204.

[110] Joel P Joseph et al. "Hypoxia induced EMT: A review on the mechanism of tumor progression and metastasis in OSCC". In: *Oral oncology* 80 (2018), pp. 23–32.

[111] Tommi Jussila and Frej Stenbäck. "Cell proliferation markers and growth factors in ovarian cancer". In: *Annals of medicine* 27.1 (1995), pp. 87–94.

[112] Ulf D Kahlert, Justin V Joseph, and Frank AE Kruyt. "EMT-and MET-related processes in nonepithelial tumors: importance for disease progression, prognosis, and therapeutic opportunities". In: *Molecular oncology* 11.7 (2017), pp. 860–877.

[113] Raghu Kalluri et al. "EMT: when epithelial cells decide to become mesenchymal-like cells". In: *The Journal of clinical investigation* 119.6 (2009), pp. 1417–1419.

[114] Jee Hyun Kang et al. "Adiponectin induces growth arrest and apoptosis of MDA-MB-231 breast cancer cell". In: *Archives of pharmacal research* 28.11 (2005), pp. 1263–1269.

[115] Fuat Kaplan and Fulya Teksen. "Apoptotic effects of salinomycin on human ovarian cancer cell line (OVCAR-3)". In: *Tumor Biology* 37 (2016), pp. 3897–3903.

[116] Mojgan Karimi-Zarchi et al. "The clinicopathologic characteristics and 5-year survival rate of epithelial ovarian cancer in Yazd, Iran". In: *Electronic physician* 7.6 (2015), p. 1399.

[117] Laura Kerosuo and Marianne Bronner-Fraser. "What is bad in cancer is good in the embryo: importance of EMT in neural crest development". In: *Seminars in cell & developmental biology*. Vol. 23. Elsevier. 2012, pp. 320–332.

[118] Wael Khazen et al. "Expression of macrophage-selective markers in human and rodent adipocytes". In: *FEBS letters* 579.25 (2005), pp. 5631–5634.

[119] SI Kim and J-W Kim. "Role of surgery and hyperthermic intraperitoneal chemotherapy in ovarian cancer". In: *ESMO open* 6.3 (2021), p. 100149.

[120] Yangjin Kim et al. "Transformed epithelial cells and fibroblasts/myofibroblasts interaction in breast tumor: a mathematical model and experiments". In: *Journal of mathematical biology* 61.3 (2010), pp. 401–421.

[121] Tatiana Kisseleva and David A Brenner. "Is it the end of the line for the EMT?" In: *Hepatology* 53.5 (2011), pp. 1433–1435.

[122] Yuliya Klymenko et al. "Heterogeneous cadherin expression and multicellular aggregate dynamics in ovarian cancer dissemination". In: *Neoplasia* 19.7 (2017), pp. 549–563.

[123] Chie Kudo-Saito et al. "Cancer metastasis is accelerated through immunosuppression during Snail-induced EMT of cancer cells". In: *Cancer cell* 15.3 (2009), pp. 195–206.

[124] Sandeep Kumar, Alakesh Das, and Shamik Sen. "Extracellular matrix density promotes EMT by weakening cell–cell adhesions". In: *Molecular bioSystems* 10.4 (2014), pp. 838–850.

[125] Arthur W Lambert and Robert A Weinberg. "Linking EMT programmes to normal and neoplastic epithelial stem cells". In: *Nature Reviews Cancer* 21.5 (2021), pp. 325–338.

[126] Samy Lamouille et al. "Regulation of epithelial–mesenchymal and mesenchymal–epithelial transitions by microRNAs". In: *Current opinion in cell biology* 25.2 (2013), pp. 200–207.

[127] Kerry A Landman and Anna Q Cai. "Cell proliferation and oxygen diffusion in a vascularising scaffold". In: *Bulletin of mathematical biology* 69 (2007), pp. 2405–2428.

[128] Meghan Leary et al. "Sensitization of drug resistant cancer cells: a matter of combination therapy". In: *Cancers* 10.12 (2018), p. 483.

[129] YuKyung Lee, Woo Hee Jung, and Ja Seung Koo. "Adipocytes can induce epithelial-mesenchymal transition in breast cancer cells". In: *Breast cancer research and treatment* 153.2 (2015), pp. 323–335.

[130] Ernst Lengyel. "Ovarian cancer development and metastasis". In: *The American journal of pathology* 177.3 (2010), pp. 1053–1064.

[131] Caihong Li et al. "Astragalus polysaccharides increase the sensitivity of SKOV3 cells to cisplatin". In: *Archives of gynecology and obstetrics* 297 (2018), pp. 381–386.

[132] Jun-Long Liang et al. "Recent advances in engineered materials for immunotherapy-involved combination cancer therapy". In: *Advanced Materials* 33.31 (2021), p. 2007630.

[133] Tsai-Tsen Liao and Muh-Hwa Yang. "Revisiting epithelial-mesenchymal transition in cancer metastasis: the connection between epithelial plasticity and stemness". In: *Molecular oncology* 11.7 (2017), pp. 792–804.

[134] Juliane M Liberto et al. "Current and emerging methods for ovarian cancer screening and diagnostics: a comprehensive review". In: *Cancers* 14.12 (2022), p. 2885.

[135] Fernando Lizcano. "The beige adipocyte as a therapy for metabolic diseases". In: *International journal of molecular sciences* 20.20 (2019), p. 5058.

[136] Kinyui Alice Lo and Lei Sun. "Turning WAT into BAT: a review on regulators controlling the browning of white adipocytes". In: *Bioscience reports* 33.5 (2013), e00065.

[137] Fredrik Lönnqvist et al. "Leptin secretion from adipose tissue in women. Relationship to plasma levels and gene expression." In: *The Journal of clinical investigation* 99.10 (1997), pp. 2398–2404.

[138] Paul Macklin et al. "Patient-calibrated agent-based modelling of ductal carcinoma in situ (DCIS): from microscopic measurements to macroscopic predictions of clinical progression". In: *Journal of theoretical biology* 301 (2012), pp. 122–140.

[139] Adam L MacLean et al. "Epithelial-mesenchymal transition in metastatic cancer cell populations affects tumor dormancy in a simple mathematical model". In: *Biomedicines* 2.4 (2014), pp. 384–402.

[140] Joana Maia et al. "Exosome-based cell-cell communication in the tumor microenvironment". In: *Frontiers in cell and developmental biology* 6 (2018), p. 18.

[141] Emilia Majsiak et al. "The impact of symptoms on quality of life before and after diagnosis of coeliac disease: The results from a Polish population survey and comparison with the results from the United Kingdom". In: *BMC gastroenterology* 21 (2021), pp. 1–11.

[142] Tomaz Makovec. "Cisplatin and beyond: molecular mechanisms of action and drug resistance development in cancer chemotherapy". In: *Radiology and oncology* 53.2 (2019), pp. 148–158.

[143] Kyle Mani et al. "Causes of death among people living with metastatic cancer". In: *Nature Communications* 15.1 (2024), p. 1519.

[144] Guya D Marconi et al. "Epithelial-mesenchymal transition (EMT): the type-2 EMT in wound healing, tissue regeneration and organ fibrosis". In: *Cells* 10.7 (2021), p. 1587.

[145] Natasha K Martin et al. "Tumour–stromal interactions in acid-mediated invasion: a mathematical model". In: *Journal of theoretical biology* 267.3 (2010), pp. 461–470.

[146] Andrea I McClatchey and Alpha S Yap. “Contact inhibition (of proliferation) redux”. In: *Current opinion in cell biology* 24.5 (2012), pp. 685–694.

[147] Gary R Mirams et al. “Chaste: an open source C++ library for computational physiology and biology”. In: *PLoS computational biology* 9.3 (2013), e1002970.

[148] Timothy J Mitchison. “The proliferation rate paradox in antimitotic chemotherapy”. In: *Molecular biology of the cell* 23.1 (2012), pp. 1–6.

[149] Abhisek Mitra, Lopa Mishra, and Shulin Li. “EMT, CTCs and CSCs in tumor relapse and drug-resistance”. In: *Oncotarget* 6.13 (2015), p. 10697.

[150] Steven M Mooney et al. “The GRHL2/ZEB feedback loop—a key axis in the regulation of EMT in breast cancer”. In: *Journal of cellular biochemistry* 118.9 (2017), pp. 2559–2570.

[151] Aristidis Moustakas and Carl-Henrik Heldin. “Signaling networks guiding epithelial–mesenchymal transitions during embryogenesis and cancer progression”. In: *Cancer science* 98.10 (2007), pp. 1512–1520.

[152] Franco Muggia and Andrea Bonetti. “History of intraperitoneal platinum drug delivery for ovarian cancer and its future applications”. In: *Cancer Drug Resistance* 4.2 (2021), p. 453.

[153] Ryan J Murphy et al. “The role of mechanical interactions in EMT”. In: *Physical Biology* 18.4 (2021), p. 046001.

[154] Kim Nasmyth. “Putting the cell cycle in order”. In: *Science* 274.5293 (1996), pp. 1643–1645.

[155] DG Nicholls. “The bioenergetics of brown adipose tissue mitochondria”. In: *FEBS letters* 61.2 (1976), pp. 103–110.

[156] M Angela Nieto. “Epithelial plasticity: a common theme in embryonic and cancer cells”. In: *Science* 342.6159 (2013), p. 1234850.

[157] GM Nieuwenhuyzen-de Boer et al. “Adjuvant use of PlasmaJet device during cytoreductive surgery for advanced-stage ovarian cancer: Results of the PlaComOv-study, a randomized controlled trial in the Netherlands”. In: *Annals of Surgical Oncology* 29.8 (2022), pp. 4833–4843.

[158] Motoaki Ohtsubo and James M Roberts. “Cyclin-dependent regulation of G1 in mammalian fibroblasts”. In: *Science* 259.5103 (1993), pp. 1908–1912.

[159] Samuel Oliver et al. “Exploring the role of EMT in ovarian cancer progression using a multiscale mathematical model”. In: *npj Systems Biology and Applications* 11.1 (2025), p. 36.

[160] Edouard Ollier et al. "Analysis of temozolomide resistance in low-grade gliomas using a mechanistic mathematical model". In: *Fundamental & clinical pharmacology* 31.3 (2017), pp. 347–358.

[161] Ananya Pal et al. "Partial EMT in head and neck cancer biology: a spectrum instead of a switch". In: *Oncogene* 40.32 (2021), pp. 5049–5065.

[162] John C Panetta et al. "Using pharmacokinetic and pharmacodynamic modeling and simulation to evaluate importance of schedule in topotecan therapy for pediatric neuroblastoma". In: *Clinical Cancer Research* 14.1 (2008), pp. 318–325.

[163] Paolo Paoli, Elisa Giannoni, and Paola Chiarugi. "Anoikis molecular pathways and its role in cancer progression". In: *Biochimica et Biophysica Acta (BBA)-Molecular Cell Research* 1833.12 (2013), pp. 3481–3498.

[164] Jeongsook Park and Jean E Schwarzbauer. "Mammary epithelial cell interactions with fibronectin stimulate epithelial-mesenchymal transition". In: *Oncogene* 33.13 (2014), pp. 1649–1657.

[165] Ievgenia Pastushenko and Cédric Blanpain. "EMT transition states during tumor progression and metastasis". In: *Trends in cell biology* 29.3 (2019), pp. 212–226.

[166] VINITA Patanaphan, Omar M Salazar, and Rapael Risco. "Breast cancer: metastatic patterns and their prognosis." In: *Southern medical journal* 81.9 (1988), pp. 1109–1112.

[167] Dennis Pedri et al. "Epithelial-to-mesenchymal-like transition events in melanoma". In: *The FEBS journal* 289.5 (2022), pp. 1352–1368.

[168] Edgar Pérez-Herrero and Alberto Fernández-Medarde. "Advanced targeted therapies in cancer: Drug nanocarriers, the future of chemotherapy". In: *European journal of pharmaceutics and biopharmaceutics* 93 (2015), pp. 52–79.

[169] Angelica Perna et al. "Different cell cycle modulation in SKOV-3 ovarian cancer cell line by anti-HIV drugs". In: *Oncology Research* 25.9 (2017), p. 1617.

[170] Howard T Petrie. "Role of thymic organ structure and stromal composition in steady-state postnatal T-cell production". In: *Immunological reviews* 189.1 (2002), pp. 8–20.

[171] Andrei Petrovski, Bhavani Sudha, and John McCall. "Optimising cancer chemotherapy using particle swarm optimisation and genetic algorithms". In: *International Conference on Parallel Problem Solving from Nature*. Springer. 2004, pp. 633–641.

[172] MJ Piccart, H Lamb, and Jan Baptist Vermorken. "Current and future potential roles of the platinum drugs in the treatment of ovarian cancer". In: *Annals of Oncology* 12.9 (2001), pp. 1195–1203.

[173] Maksim V Plikus et al. "Fibroblasts: Origins, definitions, and functions in health and disease". In: *Cell* 184.15 (2021), pp. 3852–3872.

[174] Sylvia P Poulos, Dorothy B Hausman, and Gary J Hausman. "The development and endocrine functions of adipose tissue". In: *Molecular and cellular endocrinology* 323.1 (2010), pp. 20–34.

[175] Anna Ptak, Elzbieta Kolaczkowska, and Ewa L Gregoraszczuk. "Leptin stimulation of cell cycle and inhibition of apoptosis gene and protein expression in OVCAR-3 ovarian cancer cells". In: *Endocrine* 43 (2013), pp. 394–403.

[176] Anna Ptak, Anna Wróbel, and Ewa L Gregoraszczuk. "Effect of bisphenol-A on the expression of selected genes involved in cell cycle and apoptosis in the OVCAR-3 cell line". In: *Toxicology letters* 202.1 (2011), pp. 30–35.

[177] Kira Pugh et al. "Simulations probe the role of space in the interplay between drug-sensitive and drug-resistant cancer cells". In: *Journal of Theoretical Biology* (2025), p. 112048.

[178] Alain Puisieux, Thomas Brabletz, and Julie Caramel. "Oncogenic roles of EMT-inducing transcription factors". In: *Nature cell biology* 16.6 (2014), pp. 488–494.

[179] Marie-Therese Puth, Markus Neuhäuser, and Graeme D Ruxton. "Effective use of Pearson's product–moment correlation coefficient". In: *Animal behaviour* 93 (2014), pp. 183–189.

[180] Luyu Qi et al. "Advances in toxicological research of the anticancer drug cisplatin". In: *Chemical research in toxicology* 32.8 (2019), pp. 1469–1486.

[181] Lizzia Raffaghello and Francesco Dazzi. "Classification and biology of tumour associated stromal cells". In: *Immunology letters* 168.2 (2015), pp. 175–182.

[182] Céline Revenu and Darren Gilmour. "EMT 2.0: shaping epithelia through collective migration". In: *Current opinion in genetics & development* 19.4 (2009), pp. 338–342.

[183] Conly L Rieder. "Mitosis in vertebrates: the G2/M and M/A transitions and their associated checkpoints". In: *Chromosome Research* 19 (2011), pp. 291–306.

[184] Evanthia T Roussos, John S Condeelis, and Antonia Patsialou. "Chemotaxis in cancer". In: *Nature Reviews Cancer* 11.8 (2011), pp. 573–587.

[185] Nathan Rout-Pitt et al. “Epithelial mesenchymal transition (EMT): a universal process in lung diseases with implications for cystic fibrosis pathophysiology”. In: *Respiratory research* 19.1 (2018), pp. 1–10.

[186] Liangyou Rui. “Brown and beige adipose tissues in health and disease”. In: *Comprehensive Physiology* 7.4 (2017), p. 1281.

[187] Marcus Ruscetti et al. “HDAC inhibition impedes epithelial–mesenchymal plasticity and suppresses metastatic, castration-resistant prostate cancer”. In: *Oncogene* 35.29 (2016), pp. 3781–3795.

[188] Harold Sacks and Michael E Symonds. “Anatomical locations of human brown adipose tissue: functional relevance and implications in obesity and type 2 diabetes”. In: *Diabetes* 62.6 (2013), pp. 1783–1790.

[189] Harold S Sacks and John N Fain. “Human epicardial adipose tissue: a review”. In: *American heart journal* 153.6 (2007), pp. 907–917.

[190] Masao Saitoh. “Involvement of partial EMT in cancer progression”. In: *The Journal of Biochemistry* 164.4 (2018), pp. 257–264.

[191] Karine Salin et al. “Variation in the link between oxygen consumption and ATP production, and its relevance for animal performance”. In: *Proceedings of the Royal Society B: Biological Sciences* 282.1812 (2015), p. 20151028.

[192] Kritika Saxena, Mohit Kumar Jolly, and Kuppusamy Balamurugan. “Hypoxia, partial EMT and collective migration: Emerging culprits in metastasis”. In: *Translational oncology* 13.11 (2020), p. 100845.

[193] Yuliya Sedletska, Marie-Josèphe Giraud-Panis, and Jean-Marc Malinge. “Cisplatin is a DNA-damaging antitumour compound triggering multifactorial biochemical responses in cancer cells: importance of apoptotic pathways”. In: *Current Medicinal Chemistry-Anti-Cancer Agents* 5.3 (2005), pp. 251–265.

[194] TJ Sego et al. “Tissue forge: Interactive biological and biophysics simulation environment”. In: *PLOS Computational Biology* 19.10 (2023), e1010768.

[195] Petra Sekyrova, Joel Östblom, and Michael Andäng. “Blebbing as a physical force in cancer EMT–Parallels with mitosis”. In: *Seminars in Cancer Biology*. Vol. 22. Elsevier. 2012, pp. 369–373.

[196] Ron Sender and Ron Milo. “The distribution of cellular turnover in the human body”. In: *Nature medicine* 27.1 (2021), pp. 45–48.

[197] Yachen Shen et al. “Shared PPARα/γ target genes regulate brown adipocyte thermogenic function”. In: *Cell reports* 30.9 (2020), pp. 3079–3091.

[198] Yasuko Shimada et al. “The effect of periodontal treatment on serum leptin, interleukin-6, and C-reactive protein”. In: *Journal of periodontology* 81.8 (2010), pp. 1118–1123.

[199] Aasa Shimizu et al. “Patient-derived exosomes as siRNA carriers in ovarian cancer treatment”. In: *Cancers* 16.8 (2024), p. 1482.

[200] Omar Shindi et al. “The combined effect of optimal control and swarm intelligence on optimization of cancer chemotherapy”. In: *Computer Methods and Programs in Biomedicine* 189 (2020), p. 105327.

[201] Hitoshi Shiozaki et al. “E-cadherin mediated adhesion system in cancer cells”. In: *Cancer: Interdisciplinary International Journal of the American Cancer Society* 77.8 (1996), pp. 1605–1613.

[202] Alfred Sholl-Franco et al. “ATP controls cell cycle and induces proliferation in the mouse developing retina”. In: *International Journal of Developmental Neuroscience* 28.1 (2010), pp. 63–73.

[203] Monica Simeoni et al. “Predictive pharmacokinetic-pharmacodynamic modeling of tumor growth kinetics in xenograft models after administration of anticancer agents”. In: *Cancer research* 64.3 (2004), pp. 1094–1101.

[204] Bethany N Smith and Neil A Bhowmick. “Role of EMT in metastasis and therapy resistance”. In: *Journal of clinical medicine* 5.2 (2016), p. 17.

[205] G Solinas et al. “Tumor-associated macrophages (TAM) as major players of the cancer-related inflammation”. In: *Journal of leukocyte biology* 86.5 (2009), pp. 1065–1073.

[206] Estel Solsona-Vilarrasa and Karen H Vousden. “Obesity, white adipose tissue and cancer”. In: *The FEBS Journal* 292.9 (2025), pp. 2189–2207.

[207] M Soltani and Pu Chen. “Numerical modeling of fluid flow in solid tumors”. In: *PloS one* 6.6 (2011), e20344.

[208] Annie Cristhine Moraes Sousa-Squiavinato et al. “Cofilin-1 signaling mediates epithelial-mesenchymal transition by promoting actin cytoskeleton reorganization and cell-cell adhesion regulation in colorectal cancer cells”. In: *Biochimica et Biophysica Acta (BBA)-Molecular Cell Research* 1866.3 (2019), pp. 418–429.

[209] Jörn Starruß et al. “Morpheus: a user-friendly modeling environment for multiscale and multicellular systems biology”. In: *Bioinformatics* 30.9 (2014), pp. 1331–1332.

[210] Andrew Stein et al. “Dynamic tumor modeling of the dose–response relationship for everolimus in metastatic renal cell carcinoma using data from the phase 3 RECORD-1 trial”. In: *BMC cancer* 12 (2012), pp. 1–10.

[211] Ruby M van Stein et al. “Standardizing HIPEC and perioperative care for patients with ovarian cancer in the Netherlands using a Delphi-based consensus”. In: *Gynecologic Oncology Reports* 39 (2022), p. 100945.

[212] Zhiqi Sun et al. “Perilipin1 promotes unilocular lipid droplet formation through the activation of Fsp27 in adipocytes”. In: *Nature communications* 4.1 (2013), pp. 1–15.

[213] Anudeep Surendran et al. “Agent-based modelling reveals the role of the tumor microenvironment on the short-term success of combination temozolomide/immune checkpoint blockade to treat glioblastoma”. In: *The Journal of Pharmacology and Experimental Therapeutics* 387.1 (2023), pp. 66–77.

[214] Maciej H Swat et al. “Multi-scale modeling of tissues using CompuCell3D”. In: *Methods in cell biology*. Vol. 110. Elsevier, 2012, pp. 325–366.

[215] Wai Leong Tam and Robert A Weinberg. “The epigenetics of epithelial-mesenchymal plasticity in cancer”. In: *Nature medicine* 19.11 (2013), pp. 1438–1449.

[216] David Tarin. “Role of the host stroma in cancer and its therapeutic significance”. In: *Cancer and Metastasis Reviews* 32.3 (2013), pp. 553–566.

[217] Roslyn Tedja et al. “Generation of Stable Epithelial–Mesenchymal Hybrid Cancer Cells with Tumorigenic Potential”. In: *Cancers* 15.3 (2023), p. 684.

[218] William P Tew. “Ovarian cancer in the older woman”. In: *Journal of geriatric oncology* 7.5 (2016), pp. 354–361.

[219] Eric Theveneau and Roberto Mayor. “Cadherins in collective cell migration of mesenchymal cells”. In: *Current opinion in cell biology* 24.5 (2012), pp. 677–684.

[220] Eric Theveneau and Roberto Mayor. “Collective cell migration of epithelial and mesenchymal cells”. In: *Cellular and Molecular Life Sciences* 70 (2013), pp. 3481–3492.

[221] EW Thompson and I Haviv. “The social aspects of EMT-MET plasticity”. In: *Nature medicine* 17.9 (2011), pp. 1048–1049.

[222] Neha Tiwari et al. “EMT as the ultimate survival mechanism of cancer cells”. In: *Seminars in cancer biology*. Vol. 22. Elsevier. 2012, pp. 194–207.

[223] Lindsey A Torre et al. “Ovarian cancer statistics, 2018”. In: *CA: a cancer journal for clinicians* 68.4 (2018), pp. 284–296.

[224] Elizabeth E Trimmer and John M Essigmann. “Cisplatin.” In: *Essays in biochemistry* 34 (1999), pp. 191–211.

[225] Shubham Tripathi et al. “A mechanism for epithelial-mesenchymal heterogeneity in a population of cancer cells”. In: *PLoS computational biology* 16.2 (2020), e1007619.

[226] Neil Vasan, José Baselga, and David M Hyman. “A view on drug resistance in cancer”. In: *Nature* 575.7782 (2019), pp. 299–309.

[227] Faina Vikhanskaya et al. “Inactivation of p53 in a human ovarian cancer cell line increases the sensitivity to paclitaxel by inducing G2/M arrest and apoptosis”. In: *Experimental cell research* 241.1 (1998), pp. 96–101.

[228] Andrei I Vlad, Alexei A Romanyukha, and Tatiana E Sannikova. “Parameter tuning of agent-based models: Metaheuristic algorithms”. In: *Mathematics* 12.14 (2024), p. 2208.

[229] M Walter et al. “Interleukin 6 secreted from adipose stromal cells promotes migration and invasion of breast cancer cells”. In: *Oncogene* 28.30 (2009), pp. 2745–2755.

[230] Jun Wang et al. “Multi-scale agent-based modeling on melanoma and its related angiogenesis analysis”. In: *Theoretical Biology and Medical Modelling* 10 (2013), pp. 1–19.

[231] Lijuan Wang et al. “Ectopic over-expression of miR-429 induces mesenchymal-to-epithelial transition (MET) and increased drug sensitivity in metastasizing ovarian cancer cells”. In: *Gynecologic oncology* 134.1 (2014), pp. 96–103.

[232] Lin Wang et al. “Improved anticancer drug response prediction in cell lines using matrix factorization with similarity regularization”. In: *BMC cancer* 17 (2017), pp. 1–12.

[233] Tongtong Wang, Anand Kumar Sharma, and Christian Wolfrum. “Novel insights into adipose tissue heterogeneity”. In: *Reviews in Endocrine and Metabolic Disorders* (2022), pp. 1–8.

[234] Jukka Westermarck and Veli-Matti Kähäri. “Regulation of matrix metalloproteinase expression in tumor invasion”. In: *The FASEB journal* 13.8 (1999), pp. 781–792.

[235] Raimund J Wieser et al. “p16INK4 mediates contact-inhibition of growth”. In: *Oncogene* 18.1 (1999), pp. 277–281.

[236] Michael Ellis Williams et al. “Adipocyte derived exosomes promote cell invasion and challenge paclitaxel efficacy in ovarian cancer”. In: *Cell Communication and Signaling* 22.1 (2024), p. 443.

[237] Katarzyna Woźniak and Janusz Błasiak. "Recognition and repair of DNA-cisplatin adducts." In: *Acta Biochimica Polonica* 49.3 (2002), pp. 583–596.

[238] Agata Wronska and Zbigniew Kmiec. "Structural and biochemical characteristics of various white adipose tissue depots". In: *Acta physiologica* 205.2 (2012), pp. 194–208.

[239] Y Yang et al. "Transforming growth factor-β1 induces epithelial-to-mesenchymal transition and apoptosis via a cell cycle-dependent mechanism". In: *Oncogene* 25.55 (2006), pp. 7235–7244.

[240] Dianbo Yao, Chaoliu Dai, and Songlin Peng. "Mechanism of the mesenchymal–epithelial transition and its relationship with metastatic tumor formation". In: *Molecular cancer research* 9.12 (2011), pp. 1608–1620.

[241] Ying Ye, Qinjin Dai, and Hongbo Qi. "A novel defined pyroptosis-related gene signature for predicting the prognosis of ovarian cancer". In: *Cell death discovery* 7.1 (2021), p. 71.

[242] Tsz-Lun Yeung et al. "Cellular and molecular processes in ovarian cancer metastasis. A Review in the Theme: Cell and Molecular Processes in Cancer Metastasis". In: *American Journal of Physiology-Cell Physiology* 309.7 (2015), pp. C444–C456.

[243] Anyue Yin et al. "A review of mathematical models for tumor dynamics and treatment resistance evolution of solid tumors". In: *CPT: pharmacometrics & systems pharmacology* 8.10 (2019), pp. 720–737.

[244] Tuğba Akman Yıldız, Sadia Arshad, and Dumitru Baleanu. "New observations on optimal cancer treatments for a fractional tumor growth model with and without singular kernel". In: *Chaos, Solitons & Fractals* 117 (2018), pp. 226–239.

[245] Jinhai Yu et al. "Lipid droplet remodeling and interaction with mitochondria in mouse brown adipose tissue during cold treatment". In: *Biochimica Et Biophysica Acta (BBA)-Molecular Cell Research* 1853.5 (2015), pp. 918–928.

[246] Maximilian Zeyda and Thomas M Stulnig. "Adipose tissue macrophages". In: *Immunology letters* 112.2 (2007), pp. 61–67.

[247] Luyuan Zhang and Wei Min. "Bioorthogonal chemical imaging of metabolic changes during epithelial–mesenchymal transition of cancer cells by stimulated Raman scattering microscopy". In: *Journal of biomedical optics* 22.10 (2017), pp. 106010–106010.

[248] Pengfei Zhu et al. “The proliferation, apoptosis, invasion of endothelial-like epithelial ovarian cancer cells induced by hypoxia”. In: *Journal of Experimental & Clinical Cancer Research* 29.1 (2010), pp. 1–8.

[249] Aleksandra Zoń and Ilona Bednarek. “Cisplatin in ovarian cancer treatment—known limitations in therapy force new solutions”. In: *International journal of molecular sciences* 24.8 (2023), p. 7585.

[250] Nathan J Zvaifler. “Relevance of the stroma and epithelial-mesenchymal transition (EMT) for the rheumatic diseases”. In: *Arthritis research & therapy* 8.3 (2006), pp. 1–11.